UNIVERSITY OF OKLAHOMA

GRADUATE COLLEGE

COMPARATIVE STUDY OF PORE STRUCTURE CHARACTERIZTION FOR DIFFERENT
ROCK SAMPLES USING DIGITAL IMAGES

A THESIS

SUBMITTED TO THE GRADUATE FACULTY

in partial fulfillment of the requirements for the

Degree of

MASTER OF SCIENCE

By

YIXIN ZHANG
Norman, Oklahoma
2019

COMPARATIVE STTUDY OF PORE STRCUTURE CHARACTERIZTION FOR
DIFFERENT ROCK SAMPLES USING DIGITAL IMAGES

A THESIS APPROVED FOR THE
MEWBOURNE SCHOOL OF PETROLEUM AND GEOLOGICAL ENGINEERING

BY THE COMMITTEE CONSISTING OF

Dr. Rouzbeh Ghanbarnezhad Moghanloo, Chair

Dr. Abbas Seyedolali

Dr. Ashwin Venkatraman

Dedicate to my dear mom and dad who gave me countless love and support.

Acknowledgements

First and foremost, I would like to express my heartfelt and sincere thanks to my academic advisor Prof. Rouzbeh Ghanbarnezhad Moghanloo. Thanks for him providing me the precious study opportunity and thorough guidance on my entire degree program. I appreciate his contributions of time and ideas to make my work completed successfully. It is his deep insights, tremendous knowledge, and invaluable advice that enable me to accomplish this thesis. I am also indebted towards him for his generosity, selfless support and especially for the generous patience and forbearance that he has provided to me for the two years. Big thanks once again go to him, for without him this work would have never seen the light as it is today.

I also would like to acknowledge the committee members, Dr. Abbas Seyedolali and Dr. Ashwin Venkatraman, for their guidance and support of my research.

Furthermore, I would like to appreciate Dr. Davud Davudov for his selfless assistance in my research. Thank him for always answering my questions patiently. Without his careful help, the study would be tricky for me. Moreover, I especially appreciate Dr. Mark Curtis for providing experimental data to finish my research.

Then I think it is essential that I thank my long term friend Qi Cao for her constant encoragment and support when I met trouble. And I would like to say thank you to my friends in Oklahoma for their accompanies during my graduate life at OU.

Lastly, but perhaps most importantly, I must express my deepest gratitude to my family, my parents: Jichang and Jianing; my aunt and uncle: Yanli and Hui; my grandparents: Yuwen and Qinghai. Thank you all for giving me the strength to reach for the stars and chasing my dream. Without your love and faith, I would not have been where I am today.

Contents

List of Figures

Abstract

Due to the scarcity in supply of energy and slumping production from conventional reservoirs, exportation from unconventional tight shale reservoirs has received considerable scholarly attention in recent years. However, the evaluation of a variety of heterogenous unconventional reservoirs is challenging, because there are some imperfections and uncertainties associated with understanding of the microstructure in tight shale reservoir. Thus, the aim of this thesis is to examine a novel approach to analyze the pore structure characterization of the Marcellus and Eagle Ford shale samples.

In this study, we utilize Scanning Electron Microscopy (SEM) and micro-CT images of four different lithological rock samples including shale, sandstone, carbonate, and limestone to assess complex pore structure characterization, pore connectivity, and simulate single phase flow. Meantime, the shale rocks are compared with 20 distinct lithological rock samples to evaluate differences between their pore structure properties. We establish a three-dimensional pore structure model for each sample and partition pore space to extract corresponding pore network model using the hybrid algorithm. Additionally, we predict the absolute permeability through intrusion percolation simulation. Based on the image processing software in this study, the specific pore space parameters including porosity, pore radius, tortuosity, coordination number, are obtained. Results indicates that the computed petrophysical parameters and transport properties of shale samples are much smaller than those of carbonate, limestone, and sandstone. Furthermore, the results suggest that for the studied shale sample, Representative Elementary Volume (REV) is around 5 μm, which is smaller than that of carbonate, limestone, and sandstone samples. The results from this study will provide a new insight into complex pore structure and achieve the visualization of a micro-pore structure.

Chapter1 Introduction

Rock is a porous medium and contains a large number of pores with different sizes. These internal pores usually have diverse geometry and spatial distribution characteristics of clutter and are connected through a complicated pore space network structure existing within the rock. In addition, the internal pore and existed pore fluid directly affect the rock physical properties, such as: elastic strength modulus; Poisson's ratio of the stress; wave propagation; hydraulic conductivity; and permeability. Because of this, the recognition and quantitative characterization of rock pore structure properties are of great significance. Rock pore structure of unconventional resources has an essential effect on the reservoir storage and the internal fluid flow behavior. The study of reservoir microscopic pore shape, connectivity, pore size distribution, and coordination number are helpful to the classification evaluation of reservoir, also helping to predict the productivity performance of unconventional tight reservoirs.

Due to dwindling production from conventional reservoirs and recent developments in technology, production from unconventional shale reservoirs has been lately gaining much attention. For unconventional reservoirs, pore connectivity and pore structure are crucial in transport properties. Furthermore, in the exploitation of shale gas, researchers found that the pore size varies from nanometer to micron, that the gas storage and migration mechanism are complex and diverse, and the gases with pores of different sizes have different motion characteristics. For example, in nanopores, methane molecules are mainly adsorbed and exhibit diffusion motion. In micron pores, the free state is dominant, which is characterized by seepage. Additionally, for rocks with small porosity and extremely low permeability, the gas slippage effect is visible, and the measured permeability is greatly affected by the external environment (temperature and pressure).

Therefore, accurate and quantitative description of shale pore structure characteristics is an essential content of shale reservoir evaluation.

Because shale experiences various levels of diagenesis, and thus the pore structure can be quite complex and produce a lot of nano-pores, which leads to shale that is characterized by low effective porosity, low permeability, and substantial heterogeneity. The fluid flow is a necessary process for the rock, as it is a porous medium, and leads to material transport. The permeability determines the difficulty of fluid flowing through the porous rock, which is the most important parameter to describe the transport properties of the rock. However, due to the complexity and randomness of the pore structure of the rock, the permeability of different types of rock varies greatly, up to about ten orders of magnitude. Even for the same type of rock, due to the different formation environments and geological conditions, the permeability can vary by several orders of magnitude. Thus, the complexity of the pore structure makes it difficult to describe the comprehensively permeability of rock. The relationship between pore structure characteristics and rock permeability is not evident. The randomness of macroscopic permeability of pore rock makes the prediction of rock permeability very difficult. The main factors that affecting the permeability tensor of porous rock include porosity of the rock, connectivity of pores, pore shape and size, internal stress and strain state, and pore pressure.

Bourbie et al. (1987) illustrated the relationship between the permeability and porosity for Fontainebleau sandstone and showed that the Kozeny-Carman formula based on the isometric channel model could better explain the relationship between the permeability of rock with higher porosity and the pore structure parameters. Even so, this model simplified the pore network structure inside the rock into circular pipes, ignoring the complexity of pore structure. Historically, mercury intrusion techniques and gas adsorption techniques combined with the NMR technique

are used as macroscopic scope for pore size analysis of conventional reservoirs. However, Bustin (2008) pointed out potential pitfalls of using very high mercury injection pressures to get pore size distribution. For unconventional reservoirs, a very high pressure (>60,000psi) is required for mercury to get into the whole pore structure. Moreover, macroscopic approaches are not able to visualize small nanoscale pores in shale rocks. Mercury porosimeter is a commonly used method to study the seepage-pores (those with a pore radius larger than 100nm). Alternatively, gas adsorption has been widely used to detect small pores; however, with the gas adsorption technique, only the pores within the range of 3 −100nm can be detected. Due to the natural rock forming complex pore sizes in disordered distribution, it is difficult to describe the pore structure characteristics of the rock quantitatively, because there is a limit on experimental equipment and experimental techniques. It's also difficult to achieve to observe the stress and strain distribution within the pore structure, so this technique will not be able to establish the macroscopic properties of the rock or the relationship between the pore structure characteristics.

Therefore, if a pore structure model can be established, it can be used to quantitatively describe the pore structure characteristics of rocks and explain the relationship between permeability and internal pores, making it possible to accurately and reasonably predict the rock permeability of different pore structures. For this reason, researchers focus on the pore structure model, through which they can quantitatively express the internal mechanism and visibly observe internal physics structures. Digital rock analysis becomes an alternative method for visualizing, analyzing, and modeling the unconventional reservoirs.

In this study, we mainly examine a new method to analyze the pore structure parameters of 600 contiguous high-resolution SEM images with 6 μm of Marcellus and Eagle Ford shale samples.

We compared different rocks (shale, sandstone, carbonate, and limestone samples) to observe the difference between their pore structure properties.

Objective of Thesis

(1) Evaluate the difference in pore structure among shale, carbonate, sandstone, and limestone samples.

(2) Identify the relations among pore space parameters, such as coordination number, connected porosity, pore and throat radius, and tortuosity for different rocks.

(3) Analyze the effect of sample size on pore connectivity and pore structure properties and determine representative elementary volume.

(4) Quantify the permeability over a considerable variation of the pore space parameters and evaluate the relationship among them.

(5) Investigate the reasons of low permeability in shale samples from mechanistic view.

(6) Construct the pore network models of four rock types to simulate single phase flow.

Outline of Thesis

The overall structure of the study takes the form of six chapters.

Chapter 1 is the introduction, which describe the uncertainties existing in shale rocks associated with pore structure and pore connectivity need to be resolved.

Chapter 2 is a literature review, which provides the former studies of digital rock models and pore network models, enumerates digital rock modelling methods, and describes the principle and apparatus of Micro-CT and FIB-SEM imaging.

Chapter 3 illustrates the procedure of digital rock model reconstruction and gives a brief description of image connectivity and image segmentation. The key point of this chapter is to

illustrate the principle of four pore network model extraction algorithms and respectively introduce their advantages and disadvantages.

Chapter 4 analyzes the data gathered and compares each of the calculated parameters in turn. In this chapter, all the samples studied in this thesis are reconstructed to measure porosity; pore radius; throat radius; geometric tortuosity; and tortuosity factor. These calculated parameters of all samples are analyzed as function of sample size to illustrate the effect of sample size on the pore structure parameters. The significance is to compare the pore structure properties of four types of rock samples: shale, sandstone, limestone and carbonate.

Chapter 5 extracts the pore network model of all samples in this thesis and predict absolute permeability for each sample. By constructing a pore network model, the coordination number results are acquired which are the best representative parameter of pore connectivity.

Chapter 6 summarizes the conclusions and makes suggestions for further work.

Chapter 2 Literature Review

Digital rock modeling is a significant method of numerical simulation of rock physics, which uses a variety of technical methods to directly obtain the internal structure of the rock formations and the authentic reproduction of the pore structure of the rock. Dvorkin (2002) summarized that the digital rock modeling technology is based on a rigorous numerical simulation of physical experiments in a realistic pore space, at the pore-scale level. Drawing on digital images to reconstruct a three-dimensional core model is an alternative method to reproduce the internal pore structure properties. By symmetrically integrating the research methods of different scholars, we divide the above methods into three categories: direct imaging method; stochastic reconstruction; and pore network model method. The purpose of direct imaging is to produce 3D images mapping the real interior structure of original stacking serial 2D images proposed by Lymberopoulos and Payatakes (1992). They adopted the traditional and laborious metal-casting method to obtain 2D serial section image. This study injected a low viscosity embedding medium into evacuated pore space under high pressure, then made the sample into a planar cut and polished it to obtain a serial slice with 7.5 µm thickness. Each new surface is photographed through an optical microscope. This study managed to determine the genus of the network by using only two sections. Vogel and Roth (2001) reconstructed network representations of soil pore structure by using 20 serial sections at a lower resolution obtained from the digital camera. Although they could acquire serial sectioning images, only $5-20$ slices per hour can be obtained, which is time-consuming, and the narrowest pores and throats are too small to be considered. The workflow is shown in Figure 1.
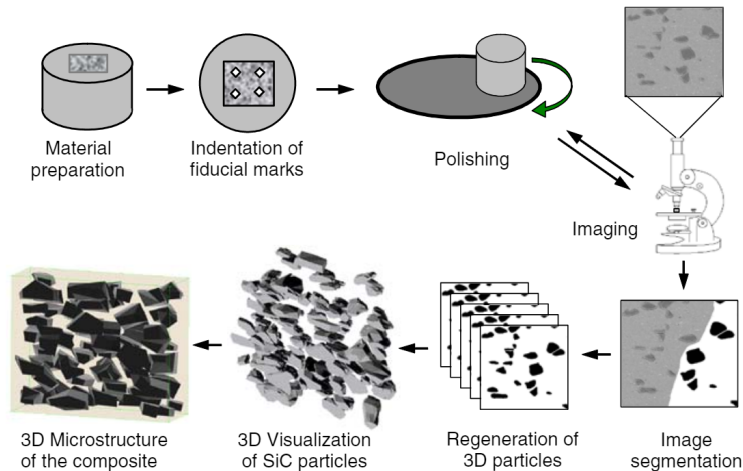
Figure 1 Workflow of Serial Sectioning Method Process (Chawla et al., 2006)

In order to avoid two-dimensional imaging generating static electricity on the rock surface and affecting the quality of the image, the serial sectioning method incorporates a micro-CT technique and a focused ion beam technique. Busch (1926) discovered that magnetic/electric fields can act as lenses for electrons. Nanometer to centimeter-scale imaging techniques, such as (focused ion beam) scanning electron microscopy, magnetic resonance imaging and X-ray (micro) tomography, have since the 1990s introduced 2D and 3D datasets of rock microstructure that allow investigation of nonlinear flow and mechanical phenomena on the length scales that are otherwise impervious to laboratory measurements. The first micro-CT technique was exhibited by Jim Elliott in the last two decades, and Dunsmur et al. (1991) first brought micro-CT technology into the petroleum field to provide high resolution images of the micro and sub-micro domains of pore space. The micro-CT technique utilizes X-ray to directly obtain stacking serial 2D images. This technique is a non-destructive method, which doesn't need to cut and polish the rock in order to obtain images. However, the highest resolution of the micro-CT technique can only read pores of 10nm or more; it would not be able to identify pores with diameters of less than 10nm. Therefore, the micro-CT

technique is only applicable to homogeneous rock, and for some homogeneous and low permeability shale samples, the micro-CT technique isn't acceptable.
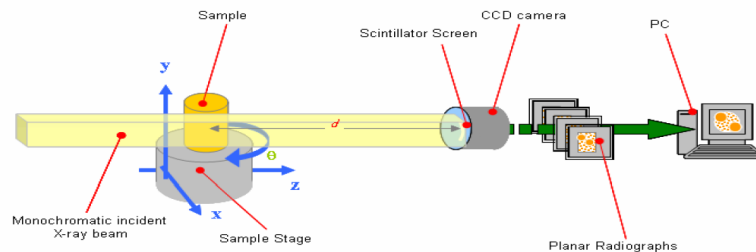
Figure 2 The schematic picture of basic components micro-CT scanner (Dong, 2009)

Tomusta and Radmilovic (2003) started to bring in an innovative 3D modeling method which combines serial section and FIB-SEM technology to get 3D models of geological materials. Knoll (1936) published the first work on the concept of Scanning Electron Microscopy (SEM). Zworykin (1942) constructed the first image using SEM. Fredrich et al. (1995) initially constructed a digital rock model using focused ion beam. Although the focused ion beam (FIB) instrument is almost identical to a SEM instrument, FIB uses a beam of ions rather than electrons. SEM is not a direct imaging technique. The focused beam of electrons is scanned across the surface of the sample and a signal is generated and detected at each point along the scan. Also, the focused ion beam can directly modify or "mill" the specimen surface, via the sputtering process, and this milling can be controlled with nanometer precision. The focused electron beam (probe) scans across the surface of the specimen via a scan generator and scan coils and the beam is addressed to a location in a matrix (x, y), remains there for a fixed time (dwell time), and then moves to the next point. At each point, a signal is generated and collected to form a 2D image. Collected signals are displayed in synch with the scan on the specimen. This technique allows the observation of organic and inorganic materials on a millimeter to nanometer scale. In addition, the resolution of FIB-SEM

technique could reach 0.4nm. Therefore, it can solve the problem of shale nanoscale pores not recognized by micro-CT.
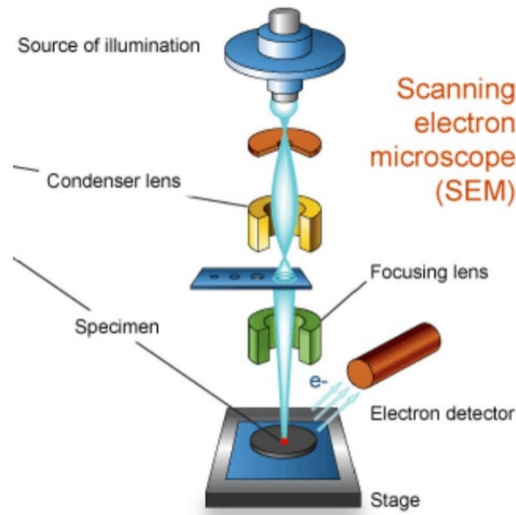
Figure 3 The Schematic Picture of Basic Component of Scanning Electron Microscope
http://www.ammrf.org.au/myscope/pdfs/sem.pdf

These image technologies are mainly used for qualitative analysis of pores. It is worth noting that the images of pore structure obtained through the direct imaging method, which can genuinely reproduce the pore structure of rock, can vary in accuracy. The 3D microstructure-based SEM accurately represents the alignment, aspect ratio, and distribution of the particles. The stochastic reconstruction method is also popular recently because the FIB-SEM technique and micro-CT technique are costly and time consuming. The stochastic method is to reconstruct the 3D digital core by a numerical method according to the statistical information of the two-dimensional high-resolution image of rock samples. But its accuracy in portraying the connectivity of the pore space has not been ideal to the present.

Then Okabe and Blunt (2004) proposed an innovative idea that multi-point geo-statistics could be used to reconstruct digital rock models. The digital rock model established by this method have

good pore connectivity, but the calculation of this method is huge, and the modeling speed is slow. Thus, in order to facilitate the study of pore structure characteristics and subsequent flow simulation, it is necessary to extract the digital core and pore network model, which is equivalent to the pore space structure of porous media. The pore network model put forward by Fatt (1956), has recently become the most popular method to study porous rocks. The pore network model is an abstract model for the geometry of complex pore spaces in real porous media. The establishment of the pore network model firstly requires the digital core corresponding to the methods of image processing and topological geometry to be processed so as to obtain the topological information of pore and throat distribution. The pore network model equates the pore space to be a number of units with different functions. The long and narrow part is the throat, and the junction of the throat is the pore body. The pore network model is helpful in describing the microscopic fluid flow mechanism and estimating transport properties.

In fact, different models have different advantages and different application scopes. Blunt and Algharbi (2004) established a three-dimensional pore structure model of sandstone through micro-CT images, extracted the pore network model by using the maximum ball algorithm, and calculated the absolute permeability and relative permeability of the rock through intrusion percolation simulation. Youssef et al. (2007) also used high resolution micro-CT laboratory analysis and partitioning of the pore space to obtain the complete and realistic description and topology of pore structure and establish the corresponding pore network model to study the fluid flow properties of carbonate. Mayka Schmitt et al. (2016) achieved pore shape classification for sandstone by using the pore network model. Nguyen (2017) adopted a stack of micro-CT images and the combined serial sectioning method to analyze the characterization of the mechanical behavior of foamed geopolymer concrete. Zhang et al. (2019) analyzed a compiled stack of SEM

images of an Eagle Ford shale sample to evaluate pore structure and complex pore connectivity by using direct modeling method. Recently, more researchers have begun to use the pore network model to observe the geometry of shale. Pore network models may provide an effective way to obtain basic hydraulic parameters for shale reservoirs, in order to understand dynamic migration of shale gas and to predict reservoir gas production. Ma (2018) built an integrated geometric and network model of a representative shale sample based on pore occurrence. His model was successful, and the resultant integrated geometric and network characteristics lead independently to the same conclusions as drawn from experimental permeability measurements made on the same Haynesville-Bossier Shale sample. Das (2019) attempted to determine the apparent permeability of Indian shale by developing a three-dimensional nano-scale pore network model to simulate the gas flow through shale while considering the micro-scale mechanisms like Knudsen diffusion, slip flow, and transition flow. The quest for a 3D-microstructure volume model to incorporate the pore network model might continue to be a great impetus to research shale samples. In this dissertation, the two models are utilized to analyze the four types of rocks to find and highlight their respective characteristics.

Chapter 3 Digital Core Reconstruction

3. 1 Image Processing Procedure

Image preprocessing plays a pivotal role in digital model reconstruction. Choosing an appropriate image processing method and dragging the maximum details for scanned grayscale images would result in more accurate measurements. The specific procedures are presented in Table 1.

```
┌─────────────────────────────────────────────┐
│     Three Dimsensional Rock Scanning Image   │
└─────────────────────────────────────────────┘
                      ↓
┌─────────────────────────────────────────────┐
│             Image Binariztion                │
└─────────────────────────────────────────────┘
                      ↓
┌─────────────────────────────────────────────┐
│              Noise Filtering                 │
└─────────────────────────────────────────────┘
                      ↓
┌─────────────────────────────────────────────┐
│       Label and Analyze Axis Connectivity    │
└─────────────────────────────────────────────┘
                      ↓
┌─────────────────────────────────────────────┐
│            Watershed Segemenation            │
├──────────────────────┬──────────────────────┤
│ Identify Pores and   │ Extract Skeleton Line │
│ Throats              │ of Pore Space         │
└──────────────────────┴──────────────────────┘
```
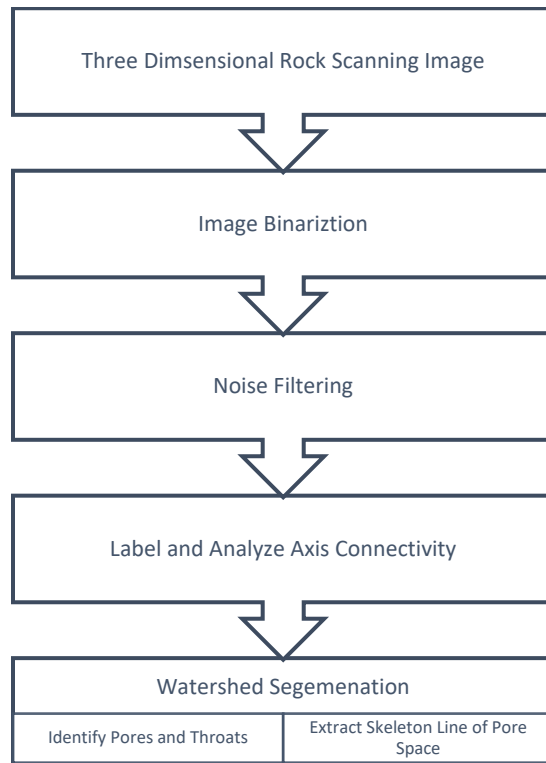
Table 1 The Basic Flowchart of Digital Images Processing

3.1.1 Image Binarization and Noise Reduction

Binarization is the process of setting the grayscale value of the pixel on the image to 0 or 255, which presents the whole image in only black and white. Image binarization dramatically reduces the amount of data in the image in comparison to the grayscale image, highlighting the contour of the target for the sample. Albeit two-dimensional rock grayscale images would contain some static information of pores and matrix, there is some image noise produced from the process of machine

scanning within them. The pore and matrix information need to be extracted by selecting an appropriate thresholding value to convert the complex SEM images and micro-CT images into binary images. Additionally, the image filtering should not be disregarded before binarization when processing images. Image filtering suppresses the noise of the target image while keeping as many of the details of the image as possible, thereby amending the quality of pictures in order to facilitate image segmentation and post-operation processing. The noise of images is listed as additive noise, multiplicative noise, and quantization noise.

(1) Additive Noise: Additive noise isn't related to the original images, which can be represented as: $f(x,y) = g(x,y) + n(x,y)$

F (x, y) represents the polluted image (noise image), g (x, y) represents the original image, and n (x, y) represents the noise. The additive noise in the image is typically generally generated in the processes of image transmission by "channel noise" and image digitization by the CCD camera.

(2) Multiplicative Noise: Multiplicative noise is related to the original images, which could be represented as: $f(x,y) = g(x,y) * n(x,y)$

Multiplicative noise in images is generally caused by particles in the film, noise in the flying-point scan image, and raster of the television scan.

(3) Quantization Noise: Quantization noise in images results from an error in the quantization process of digital modeling.

The noise of micro-CT and SEM images is mainly multiplicative. So far, there are some types of image filtering to purge noise in pictures, which are classified according to their functions as smoothing filter; enhance contrast filter; find edge filter; and adjust image frequency filter.

There are some patterns on the smoothing filter like a mean filter, median filter, anisotropic diffusive filter, and non-local mean filter. The non-local mean filter is exceptionally active on noisy data while preserving edges (best with white noise). It is generally the first choice for noisy images (Avizo® User's Guide, 2009).
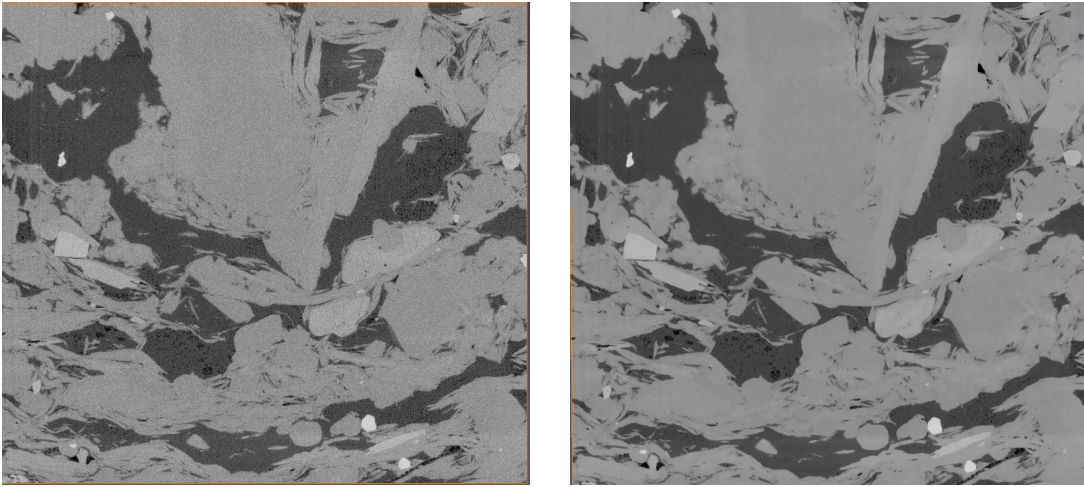
Figure 4 (a) SEM Image Before Non-local mean filter (b) SEM Image After Non-local mean filter of A Marcellus Shale Sample

In every two-dimensional digital image, each pixel can take 2k different values, where k is the bit depth of the image. This means that for an 8-bit image, each pixel can have from 1 to 28 (=256) different color levels (gray-scale levels) (Lyra, 2011). Moreover, the value dividing this range is called the image threshold, which is not a fixed magnitude, but dynamically changes according to each image and processing requirement. When converting the grayscale images to be a binary image, the appropriate thresholding value should be selected. The gray value ranges in the grayscale image is $0-255$, whereas the gray value in the binary image are 0 or 255. The thresholding is a critical value to divide the grayscale range into two parts. Different thresholding values would influence the geometrically calculated results.

Let's assume the binary image **B** [i, j] is the same as a threshold image **F**$_T$ [i, j] , which is obtained using a threshold **T** for the original gray image **F** [i, j]. Thus,

$$\bm{B}\,[i, j] = \bm{F}_T\,[i, j]$$

Where for a darker object on a lighter background

$$\bm{F}_T\,[i, j] = \begin{cases} 1, & if\ F\,[i,j] \le T \\ 0, & \text{otherwise} \end{cases}$$

The image processing software using Java (ImageJ) has ten thresholding methods to convert the grayscale images to be binary images such as Default, Huang, Minimum, Isodata, MaxEntropy, MinError, Ostu. For the Marcellus shale sample, the Ostu method would be better because this method would accentuate all organic matter pores from the grayscale SEM images. Otsu's threshold clustering algorithm searches for the threshold that minimizes the intra-class variance, defined as a weighted sum of variances of the two classes (Landini, 2017). In the image processing software Avizo®, an Interactive Thresholding operation implements binary conservation. Based on the research about the real shale samples with SEM, the high-resolution binary images of organic pores in Marcellus shale and Eagle Ford shale samples are deftly obtained. Figure 5 displays a grayscale image and its binary image of Marcellus shale sample.
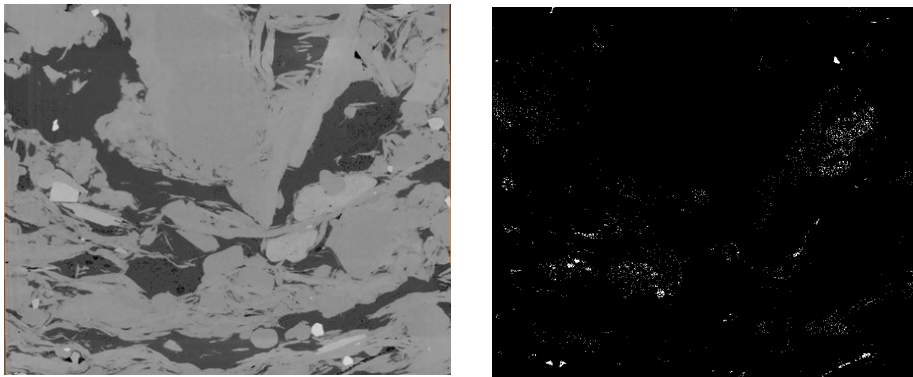
Figure 5 (a) Original SEM Image (b) Binary Image (white are pores, black are matrix) of a Marcellus Shale Sample

3.2 Image Connectivity

   For an image, the minimum unit is a pixel, and each pixel has neighboring pixels. For 2D images, there are two types of neighborhood relationships: 4 connectivity and 8 connectivity. The 4-connected pixels are neighbors to every pixel that touches one of their edges. These pixels are connected horizontally and vertically. The 8 connectivity 8-connected pixels are neighbors to every pixel that touches one of their edges or corners. These pixels are connected horizontally, vertically, and diagonally shown in Figure 6. (The Free Encyclopedia, 2019)
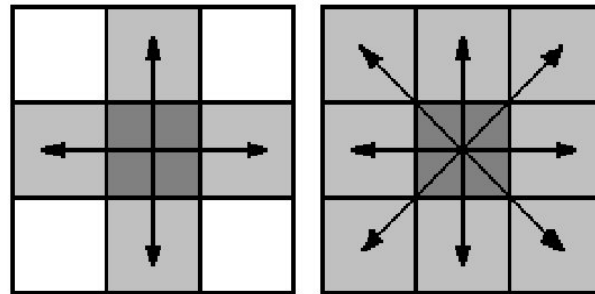
Figure 6 (a) 4-connectivity Pixel (b) 8-connectivity Pixel (Ibrahim, 2005)

   For 3D images, they have three types of neighborhood relationships: 6 connectivity; 18 connectivity and 26 connectivity shown in Figure 7. 6-connected pixels are neighbors to every pixel that touches one of their faces. 18-connected pixels are neighbors to every pixel that touches one of their faces or edges. 26 connected pixels are neighbors to every pixel that touches one of their faces, edges, or corners. (The Free Encyclopedia, 2019)
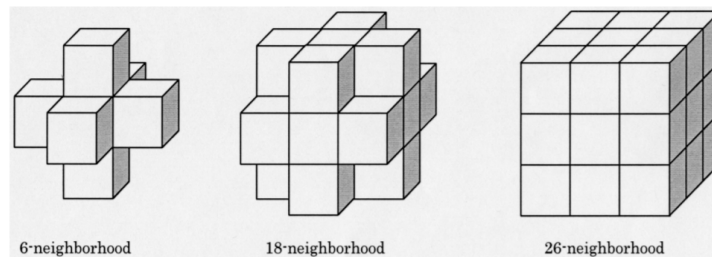
Figure 7 Three 3D Neighborhood Relationship (Toriwaki & Yonekura, 2005)

The image processing software using Java (ImageJ®) and Avizo® both use the pixel connectivity method to label connected components for SEM and Micro-CT images in this research. Each pixel's value for the binary image is either 0 or 1. The white parts are pores, for which the grayscale value is 1, and the dark parts are minerals, for which the grayscale value is 0. In this study, a seed filling algorithm is widely used to detect the connected domain between pixels. Its general steps are as follows: (1) take an unmarked pixel as the seed and mark it to establish an empty stack; (2) retrieve all adjacent pixels of the seed according to the definition of "adjacent," mark them if they are unmarked and press them into the stack; (3) take a pixel from the top of the stack as the new seed to repeat step (2); (4) repeat step (2) and (3) until the stack becomes empty again. All pixels entered in the stack are marked as one group and an attribute is given to the original seed and the group (for example, color) (Sun et al., 2016). Figure 8 displays the labeled connected components.
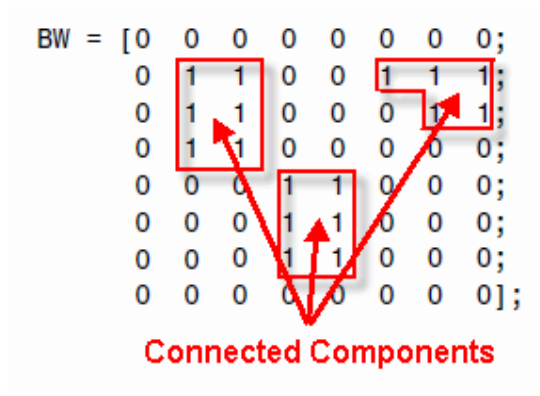
Figure 8 Connected Components Labeling https://www.mathworks.com.

Because this research takes advantage of image stacks to reconstruct 3D digital model, this study only considers the 26 connectivity pixel neighborhoods for every reconstructed sample model.
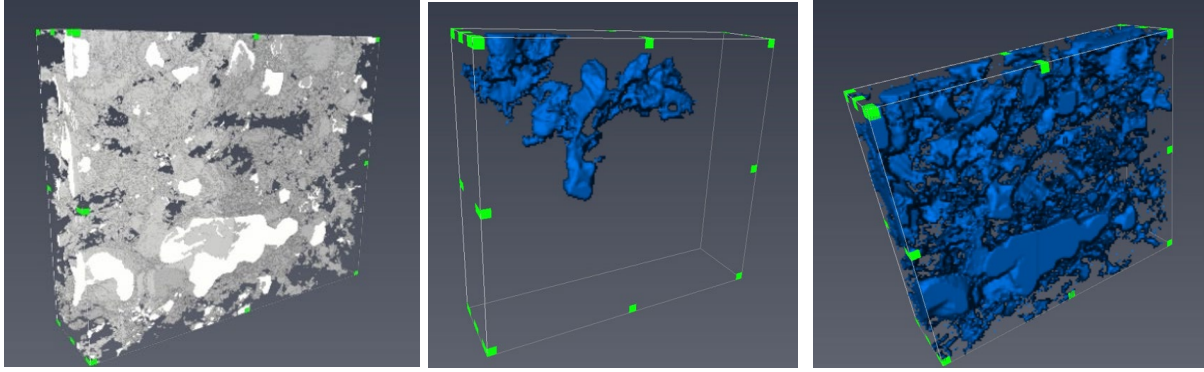
Figure 9 (a) 3D Volume Model (b)Connected Pores (c) Unconnected Pores of anEagle Ford Shale Sample
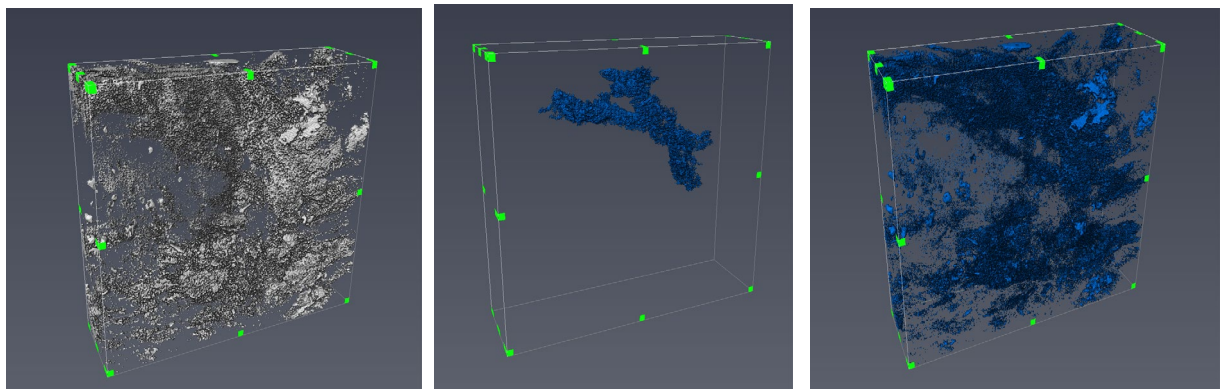
Figure 10 (a) 3D Volume Model (b) Connected Pores (c) Unconnected Pores of a Marcellus Shale Sample

3.3 Morphological Image Segmentation

The experimental Micro-CT and SEM images have some adjoining and touching pore clusters, which should be separated for proper analysis. The grayscale of SEM and Micro-CT images distributes unequally, so the watershed algorithm is used to separate objects to make deep analysis for every pore in the images. The separate objects module, an Avizo® tool, would handle the separation of interlinked pores. The separate objects module in Avizo® software is a high-level combination of watershed, distance map and H-Maxima (Avizo® user's guide, 2009).

3.3.1 The Principle of Watershed Algorithm

A watershed algorithm is a vital kind of image segmentation method. In the process of segmentation, it will use the similarity between adjacent pixels as the critical reference basis, which will consider proximity and similarity of gray value, which together constitute a closed contour. Sealing ability is an essential feature of watershed algorithms. The traditional watershed segmentation method is a kind of mathematical morphology segmentation method based on topology theory. The basic idea is to put the image as the topology of landform on geodesy, with the gray value of each pixel in the image representing that point. The elevation of each local minimum values and effect area are known as the catchment basin, while the boundary of the catchment basin forms a watershed. In the watershed algorithm, the area with a high gray value in an image is regarded as a mountain peak, and the area with a low gray value is regarded as a valley. Water is then poured in from the lowest point of the valley, and the water slowly converges in different places where the image needs to be segmented. The core idea of the watershed algorithm is to build dams (watershed lines) to prevent water from converging in different basins. In a typical watershed algorithm, a set of color images is usually converted into grayscale, and then into the gradient map, and finally, on the basis of the gradient map watershed algorithm, the segment image edge line is obtained. The following is a schematic section of the "terrain."
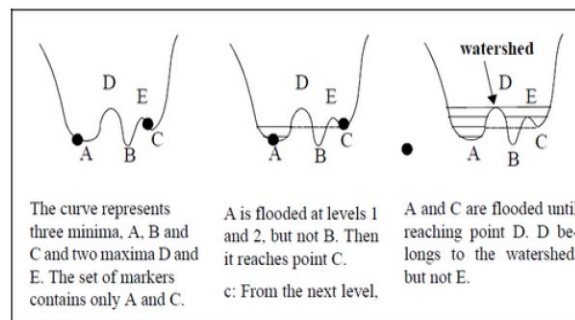
Figure 11 Watershed (Avizo® user's guide, 2009)

First, at the minimum points of the two basins, water is injected into the basin, and the water will slowly rise. The moment when the water from the two basins converges signals the proper place to build a damn (marked in black), preventing the two basins from converging into one body of water. In this way, the image is divided into two-pixel sets: one is the water injection basin pixel set, and the other is the watershed pixel set.

However, careful observation will reveal the problem that the traditional watershed algorithm, based on image gradient, generates many small water catchment basins due to the existence of too many minimal regions, resulting in image over-segmentation. Therefore, similar results must be merged. For example, with a desktop image, due to lighting, texture and other factors, the desktop will have a lot of light and dark changes, reflected in the gradient map forming a circle, and the use of the watershed algorithm will create a lot of small basins, thus dividing into a lot of small areas. But this is obviously not common sense. Because the desktop is a whole, it should belong to the same category, despite the differing texture of the different parts.

Therefore, the watershed algorithm needs to be improved. The watershed algorithm based on marker is adopted in OpenCV (a library of programming functions). The flooding process starts with a pre-defined marker image (binary image), which reduces the impact of many minimum-point basins. This process is better for overcoming the deficiency of excessive segmentation. In essence, the improved algorithm based on marker points is a method that uses prior knowledge to help segmentation. The software Avizo® adds a new tool, which computes the distance transformation. On the basis of binary image segmented by the above threshold, an object larger than the actual size of the foreground is obtained by deep expansion operation on the white foreground, and then the black part of the image after deep expansion is converted to 128 with the reverse threshold, that is, the marking of background pixels is completed. In fact, any value that is

between 0 and 255 can be used as a background marker. Different objects in the image can be identified with different values as markers, to help the watershed algorithm correctly segment the image. After separating objects, a labeling analysis module would measure, and display pore characterization such as pore diameter, pore area, and pore perimeter.
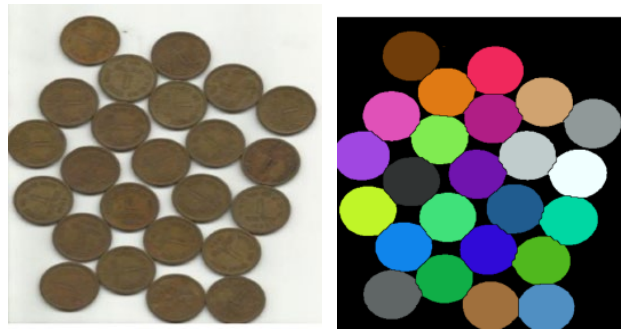
Figure 12 Image Sample (a) Before Watershed Segmentation (b) After watershed Segmentation (Kornilov et al., 2018)
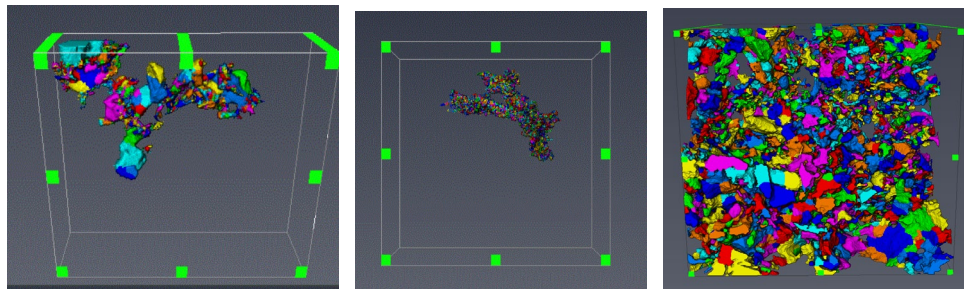
Figure 13 Watershed Segmentation of (a) Eagle Ford shale (b) Marcellus Shale (c) Carbonate C2

3.4 Pore Network Extraction

Pore network extraction, which is defined as the transformation from irregular pore space to a simplified network in the form of pores connected by throats, is significant to microstructure analysis and network modeling (Yi et al., 2017). The main advantage of pore network model is that they can accomplish simulations on many millions of pores rather than hundreds of pores currently manageable with direct numerical simulation (Raeini, 2017). Through the pore network model, transport properties such as absolute permeability, relative permeability, formation factor,

and mass transfer can be predicted efficiently (Yi et al., 2017). At the moment, the favored methods for pore network extraction should be medial axis algorithm proposed by Lindquist et al. (1993) and maximum ball algorithm proposed by Silin et al. (2003).

3.4.1 Medial-Axis Algorithm

Lindquist (1996) put forward the medial-axis is algorithm method based on the pore void space. This method regards the pores as the hollow pipes in the core, and the interconnected medial axis of the hollow pipes constitutes the medial axis of pores. The advantage of the medial-axis algorithm is that it retains the topological structure of pore void space and connectivity of pores, thus readily capturing the interconnectivity of pore space. In addition, since the algorithm is grounded in the medial axis of void space, it identifies pore and throat size expediently. The local minimum area on the medial axis is defined as throat, and the node is defined as pore body. Raeini and Blunt (2013) extended this method and deciphered the workflow of the pore network model using the medial-axis algorithm. They discretized the void space into pores and throat corners according to the voxel of void space. Firstly, the medial axis and medial surface were extracted from the distance map, which is the set of points equidistant from two or more points on the boundary as Figure 14 (Raeini, 2017). If the center of maximal sphere was located on the medial axis, this sphere was defined as a pore. Then the researchers collected the voxel faces shared by voxels of different pores to generate throat surfaces-bounding surfaces between neighboring pores (Raeini, 2017).

However, there are some problems with this algorithm. Silin and Patzek (Silin & Patzek, 2006) pointed out the medial axis algorithm would lead to ambiguous pores identification because this method cannot remove redundant links of pores and throats. Blunt (2016) further noted that the

medial axis may contain features which are not relevant for fluid flow, such as dead ends in the skeleton whenever there is any rugosity or irregularity in the pore walls.
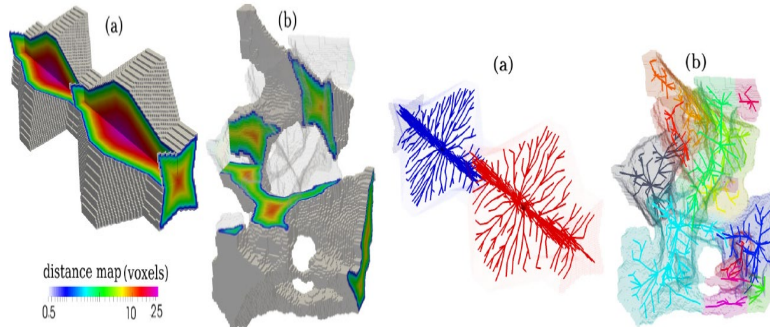
Figure 14 Distance Map for Each Pore Voxel of Medial-axis Algorithm (Raeini, 2017)

3.4.2 Maximum Ball Algorithm

The maximum ball method was pioneered by Silin et al. (2003) and a breakthrough was made on this basis by Dong and Blunt (2009) when they constructed a dendritic structure (family tree) to segment the pores and throats demonstrably. The algorithm starts with every voxel in the pore space and looks for the maximum cut ball that is in contact with the particle or boundary. Small spheres contained in other spheres will be treated as inclusions and removed, and the remaining spheres will be divided into master spheres and slave spheres to describe pore space. For any two intersecting or tangent spheres, the sphere with a larger radius is defined as the master sphere and the smaller radius sphere as the servant sphere; all larger master spheres in locality are used to represent pore bodies, and all spheres connecting adjacent pores are used to represent throat. The maximal ball algorithm could not retain the topology of pores and throats, but it would assemble discrete voxels to mimic digital balls, and then merge maximum balls into clusters. The procedure of the maximum ball algorithm was firstly developed by Dong (2009), who sorted all maximum balls from the largest to the smallest, then started from the first ball A in the image with the largest radius defined as "ancestor" and rank it as the 1st pore. The smaller overlapped pores from the 1st

pore was defined as 2nd generation, named "parents". In Figure 15, the ball B is a parent. If a ball is absorbed from two families, this ball is regarded as a throat. The same process would be repeated until the minimum ball is reached. After the process of identifying pores and throats, the pore throat chains are constructed throughout the pore space as bundle skeletons. The appealing advantage of this method is its efficiency in explicit pore identification. But Dong (2009) also alludes to the problem of this method that is the lengths of throats might be underestimated because this method cannot guarantee that every throat is located at a hydraulic restriction.
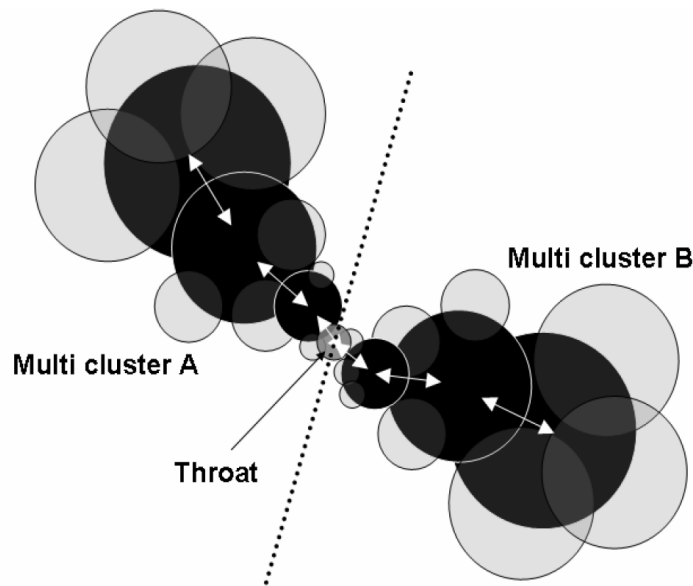
Figure 15 Family Tree of Pore Clusters (Dong, 2009)

3.4.3 Axis-Ball Algorithm

Roush and Willson (2005) first proposed combining the medial-axis and maximum ball algorithms to identify and define pores and throats. The fundamental idea of the axis-ball algorithm is building the maximal balls on a centrally located medial axis, which can both preserve the basic morphological features, and convey most of the hydraulic restrictions. The AB algorithm is coded by C++ and the flow chart is shown in Figure 16.
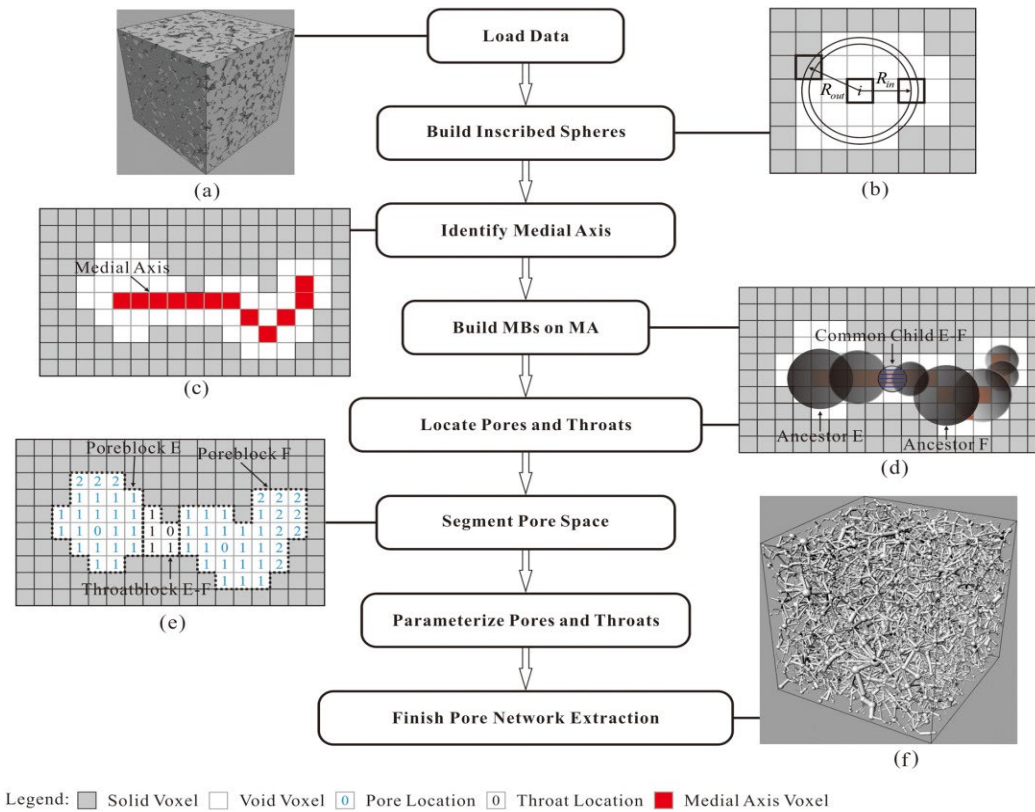
Figure 16 Workflow of Axis-Ball Algorithm (Yi et al., 2016)

Yi (2017) compared the axis-ball algorithm with medial-axis algorithm and maximal ball algorithm in terms of pore connectivity and pore throat lengths. The results are significantly different among them, listed in Figure 17.
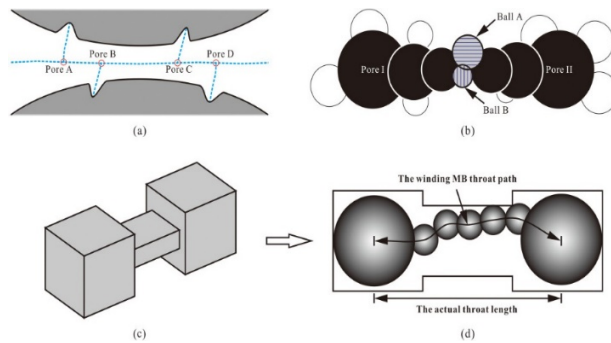
Figure 17 Thumbnail Of Maximum-Ball Algorithm And Medial-Axis Algorithm (Yi et al., 2016)

3.4.4 Application of the Watershed Algorithm

This method is to use a seeded watershed algorithm to segment the void space into pores originally investigated by Thompson et al. (2005) and Sheppard et al. (2006). But this method received a little attention until recently. This method mainly uses a distance map as the medial axis. If the distance from the center of the void voxel is larger than any neighboring points, it is named as a peak point, which should be considered as a pore. The peak point is then passed as a marker to find the basin. Gostick (2017) explains the watershed segmentation algorithm using cubic packings of spheres. First of all, the method needs to finish distance map transformation of void space, then segment the pore space resulting from the marker based watershed algorithm. In Figure 18, the interstitial space between four disks represents a pore, and the constriction between two disks represents a throat connecting two pores. But this watershed algorithm has a problem proposed by Gostick (2017), which is that the image could include erroneous peaks and generally fall along the ridges in the distance transform. So, Gostick (2017) updated this method using the snow algorithm. The snow algorithm would eliminate peaks on saddles and plateaus, merge peaks that are too near each other, then assign void voxels to the appropriate pores using marker-based watershed. The advantage of this method is that could determine pore connectivity relatively easily (Gostick, 2017).

Figure 18Marker-Based Watershed Algorithm Procedure (Gostick, 2017)

3.4.5 Hybrid Algorithm

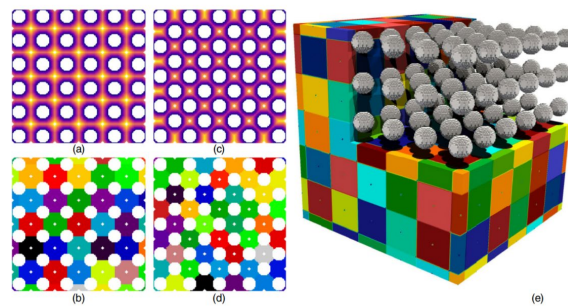This dissertation mainly uses the software Avizo® to extract pore network from digital images and analyze the transport properties for different rock samples such as (shale, sandstone, limestone and carbonate). The algorithm of Avizo® is a hybrid algorithm proposed by Youssef (2006).

This hybrid algorithm combines thinning and distance map based techniques to create the Distance Ordered Homotopic Thinning method, which uses the distance map to compute the shortest distance of each point from void space to background. The thinning algorithm is used to get the skeletonization of pore space and retain the topology, and then the distance map is used to mark each point of the skeleton with the minimum distance to the boundary of the space (Youssef et al., 2007). Youssef et al. (2007) illustrated the workflow of the hybrid algorithm for the pore network model as Figure 19. The first step is to identify the channel lines based on the skeleton of the pore space. In the meantime, the connectivity number for each line is determined and the length of each line is calculated, resulting in the tortuosity being found. The second step is to partition the skeleton and lines based different pores. Finally, the researcher partitions the pore space into individual pores using the voxel growth algorithm, then the reconstruction of labeled pores would be separated automatically. This pore network extraction method maintains the advantages of media axis and watershed algorithm, i.e. retaining the topology of void space. On the basis of the above algorithms, this hybrid algorithm could be able to determine pore connectivity and tortuosity. Figure 20 and Figure 21 present the pore network model extracted from the aforementioned algorithms.
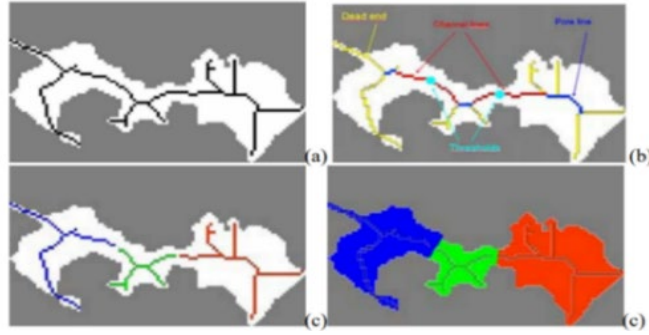
Figure 19 Geometric Separation And Label Connected Components(Youssef et al., 2007)
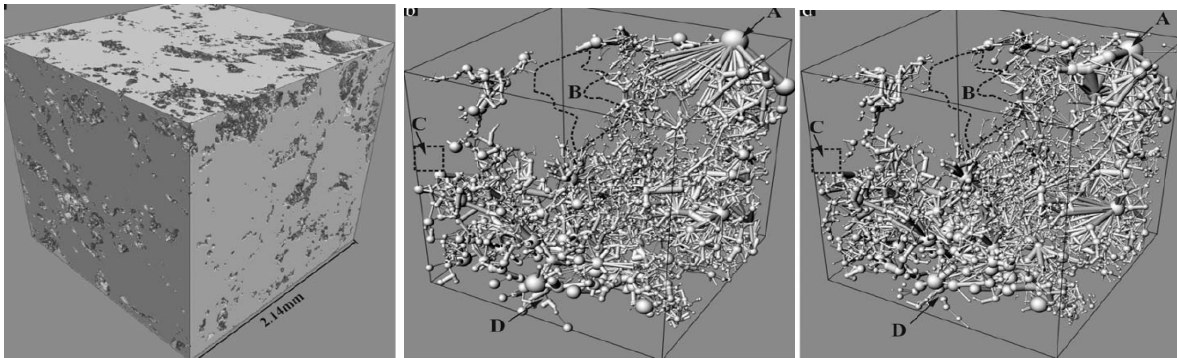

Figure 20 (a) Carbonate C2 3D Volume Model (b) Coresponding MA Network (c) Coressponding AB Network (Yi et al., 2017)
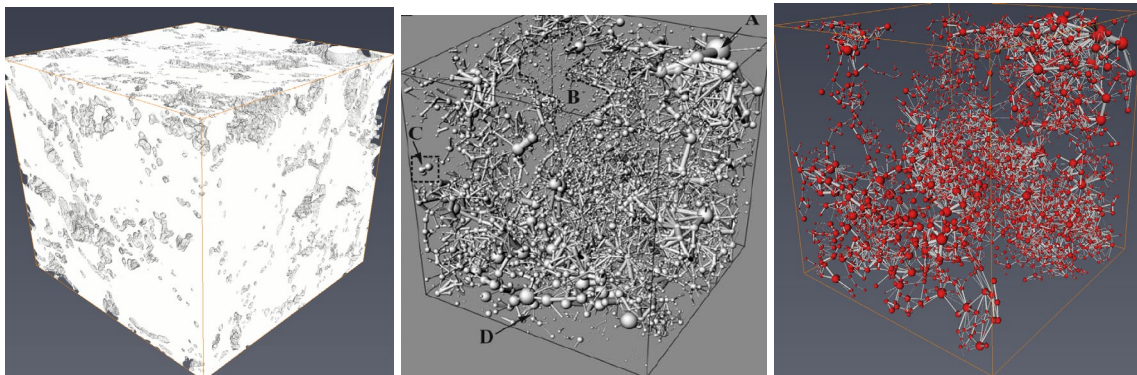

Figure 21(a) Carbonate C2 3D Volume Model from Avizo® (b) Coresponding MB Network (c) Corespodning Network from Avizo®

Chapter 4 Pore Structure Characterization Parameters

This thesis utilizes 22 rock samples to compare rock structure properties of different rock types: shale, sandstone, limestone, and carbonate. The 22 rock samples, listed in Table 2, consist of two shale samples, five carbonate samples, two limestone samples, and thirteen sandstone samples. The two shale samples are scanned, at the University of Oklahoma, with the image resolution of 10 nm/pixel using FIB-SEM technology, and the other rock samples are micro-CT images from Imperial College London.

No.	Samples	Resolution(μm/pixel)	Size (pixel^3)	Rock Type	Porosity (%)
1	Eagle Ford	0.01	2136*1986*600	Shale	---
2	Marcellus	0.01	2048*1768*600	Shale	---
3	S1	8.683	300*300*300	sandstone	14.1
4	S2	4.956	300*300*300	sandstone	24.6
5	S3	9.1	300*300*300	sandstone	16.9
6	S4	8.96	300*300*300	sandstone	17.1
7	S5	3.997	300*300*300	sandstone	21.1
8	S6	5.1	300*300*300	sandstone	24
9	S7	4.803	300*300*300	sandstone	25.1
10	S8	4.892	300*300*300	sandstone	34
11	S9	3.398	300*300*300	sandstone	22.2
12	C1	2.85	300*300*300	carbonate	23.3
13	C2	5.345	300*300*300	carbonate	16.8
14	Berea	5.345	400*400*400	sandstone	19.6
15	Bentheimer1	3.00035	1024*1024*1024	sandstone	---
16	Ketton1	3.00006	1024*1024*1024	carbonate	---
17	Ketton2	2.645	1024*1024*1024	limestone	---
18	Doddington	2.7745	1024*1024*1024	sandstone	---
19	Estaillades1	3.31136	650*650*650	carbonate	---
20	Estaillades2	3.31136	500*500*500	carbonate	---
21	Estaillades3	2.6825	1024*1024*1024	limestone	---
22	Bentheimer2	3.0035	1024*1024*1024	sandstone	---

Table 2 Image Information of The Studied Rock Samples

4.1 Porosity Distribution

After reconstructing 3D digital core samples, the porosity is measured by counting the number of voxels in the void space from the whole images (Dong, 2009). In reservoir characterization, total porosity is used for overall hydrocarbon storage assessment, while effective porosity is used for hydrocarbon production assessment. It is therefore important to gain insights into both types of porosity (Goral & Deo, 2018). For further analysis, connected porosity and total porosity of the given samples are investigated as a function of sample size. In this dissertation, the software Avizo® and ImageJ® were mainly used to measure the connected and total porosity. As shown in Figure 22 and Figure 23, it is obvious that the total porosity calculated by the two software are almost equivalent. The results of effective porosity, however, vary widely. This dissimilarity might arise from the process of adjusting thresholding calculated by ImageJ® software, which leads to a lower accuracy in the connected porosity calculated by ImageJ® than by Avizo®. Moreover, Hemes et al. (2015) consider that for the FIB-SEM data, manual cleaning of the results was applied in Avizo®. Thus, for further images, the connected porosity and total porosity are only calculated by Avizo®.

4.11 Porosity vs Sample Size for Shale Samples

Figure 22 and Figure 23 show the variation of porosity for Eagle Ford and Marcellus shale samples with sample size increases, and all curves exhibit a negative slope. The total porosity of the whole Eagle Ford sample is 12.5%, whereas the connected porosity is only 1.52%. For the Eagle Ford shale sample, the connected porosity is almost ten orders of magnitude smaller than the total porosity. A possible explanation for this disparity is that there are more occluded pores in shale samples. The total porosity of the Eagle Ford shale sample declines steadily from 15.8% to 12.5% as the sample size increases from 1μm to 6 μm. The connected porosity is 12.4% at 1μm,

and it drops to be 1.5% at 6µm. The connected porosity of the Eagle Ford shale sample is reduced by ten-fold with the increased sample size.

For the Marcellus shale sample, the total porosity of the whole sample is 1.27, however, the connected porosity of the Marcellus shale sample is only 0.17%, which is also ten times smaller than the total porosity, like the Eagle Ford shale sample. The total porosity drops from 0.27% to 0.17% as the sample increases from 1µm to 6µm. According to the different observations of two shale samples, it is evident that the connected porosity and total porosity of Marcellus shale are smaller than the Eagle Ford shale sample, and that the connected and total porosity of both shale samples are both influenced by sample size.
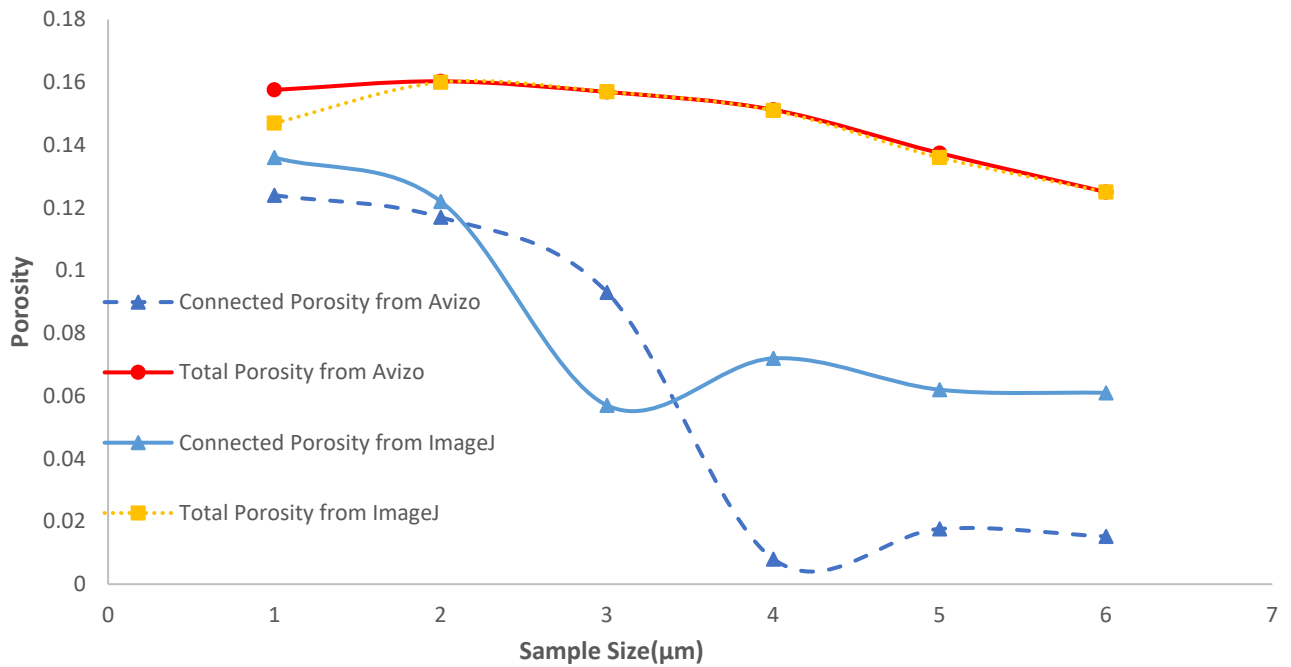

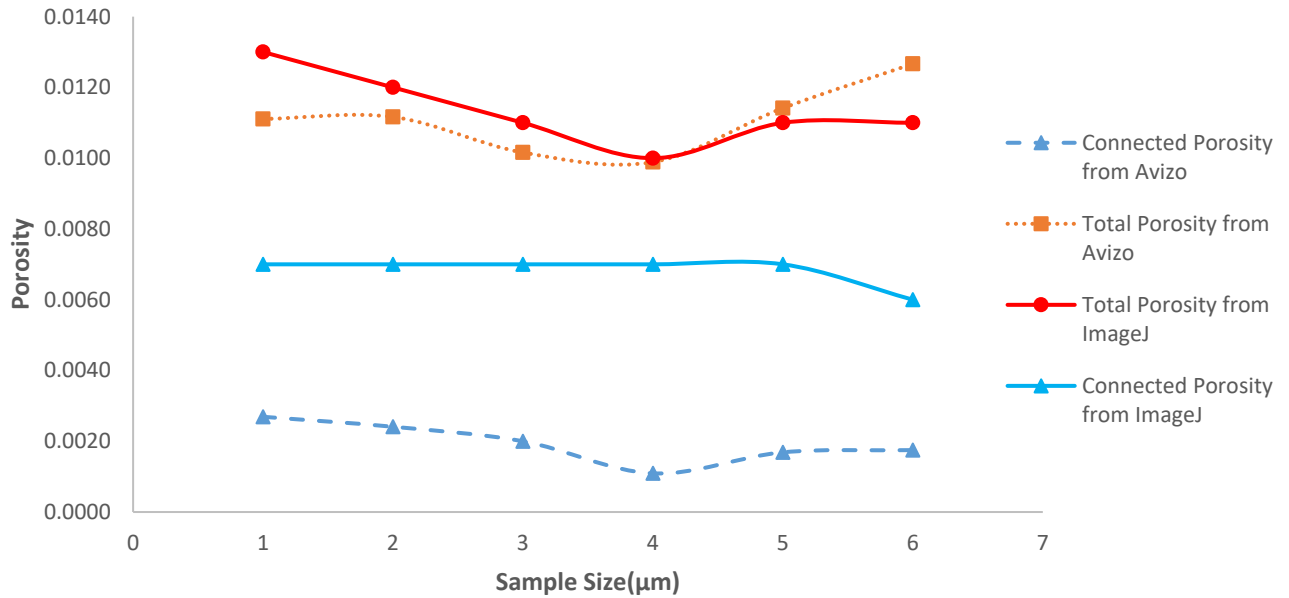**Figure 22 Porosity vs Sample Size(µm) for an Eagle Ford Shale Sample**

Figure 23 Porosity vs Sample Size (μm) for a Marcellus Shale Sample

4.1.2. Porosity vs Sample Size for Sandstone

Figure 24 − Figure 36 present the porosity distribution for 13 sandstone samples; some of them are distributed along a negative slope curve as the sample size increases from 0.2 to 3mm. Still, a few curves show a direct relationship between porosity and sample size, by which the connected porosity and total porosity would increase as sample size increases, as shown in Figure 24. Also, we find the effective porosity curve and total porosity curve of the sandstone sample (with a total porosity of the whole sample over 20%) could overlap with each other, such as happened with sample S2. If the total porosity of the full sandstone is less than 20%, there will be a 0.1% difference between connected porosity and total porosity. The connected porosity for these sandstone samples is between 14% and 33.8%. The total porosity of these sandstone samples ranges from 14.1% and 34%. In these thirteen sandstone samples, the sample S8 has the highest total porosity (34%) and connected porosity (33.8%), whereas the connected and total porosity of sandstone S1 (14% and 14.1%, respectively) is smallest in these sandstone samples.

32

Although 300 contiguous images are taken of each sandstone sample in this study, the resolution of each sample is different. Interestingly, if the image resolution of sandstone is less than 5µm/pixel, the connected porosity and total porosity appear especially close. When the sample size increases, the connected porosity and total porosity just rise or fall only 1% ~ 3%.
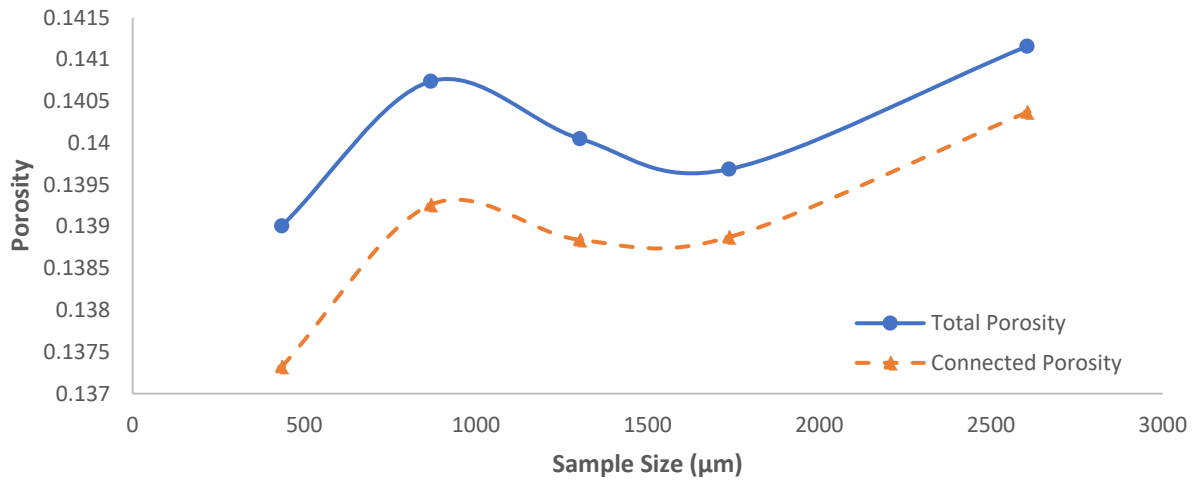

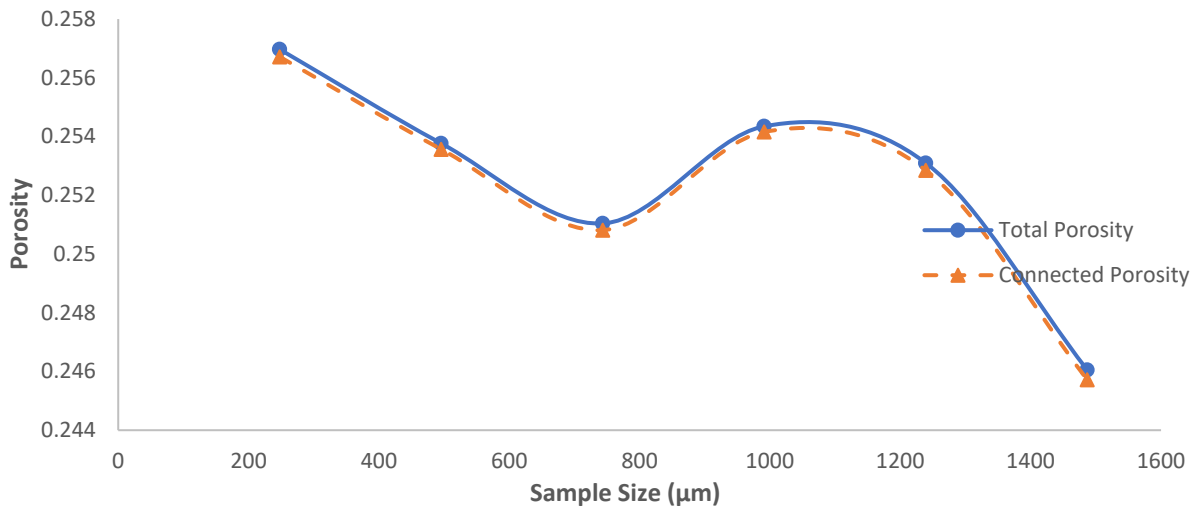**Figure 24 Porosity vs Sample Size (µm) for Sandstone S1 Sample**

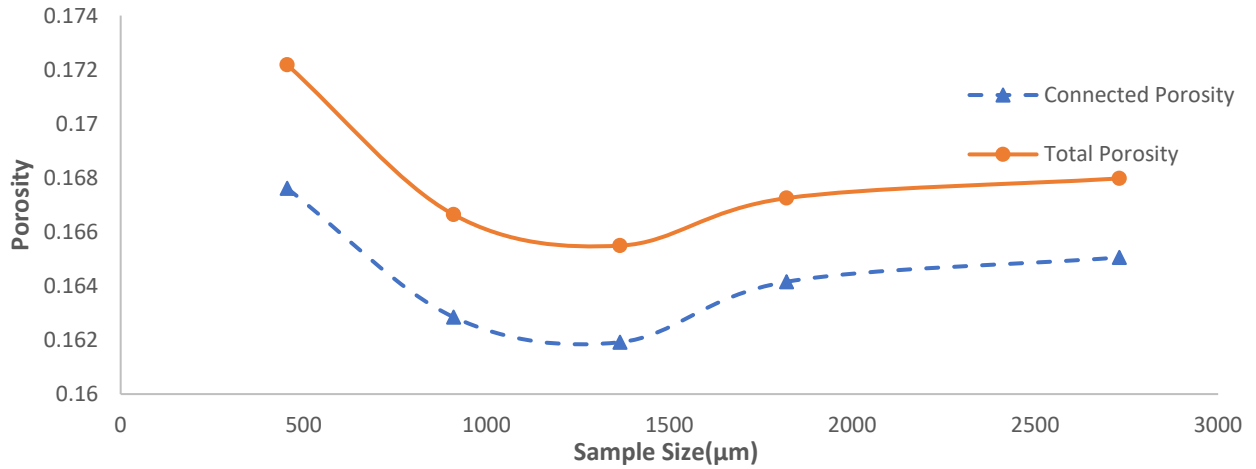**Figure 25 Porosity vs Sample Size (µm) for Sandstone S2 Sample**

Figure 26 Porosity vs Sample Size (μm) for Sandstone S3 Sample
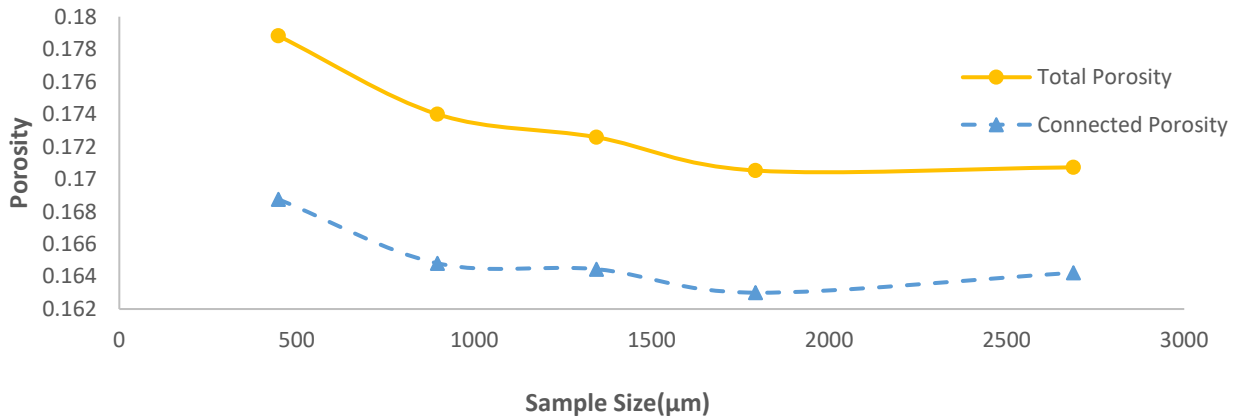

Figure 27 Porosity vs Sample Size (μm) for Sandstone S4 Sample
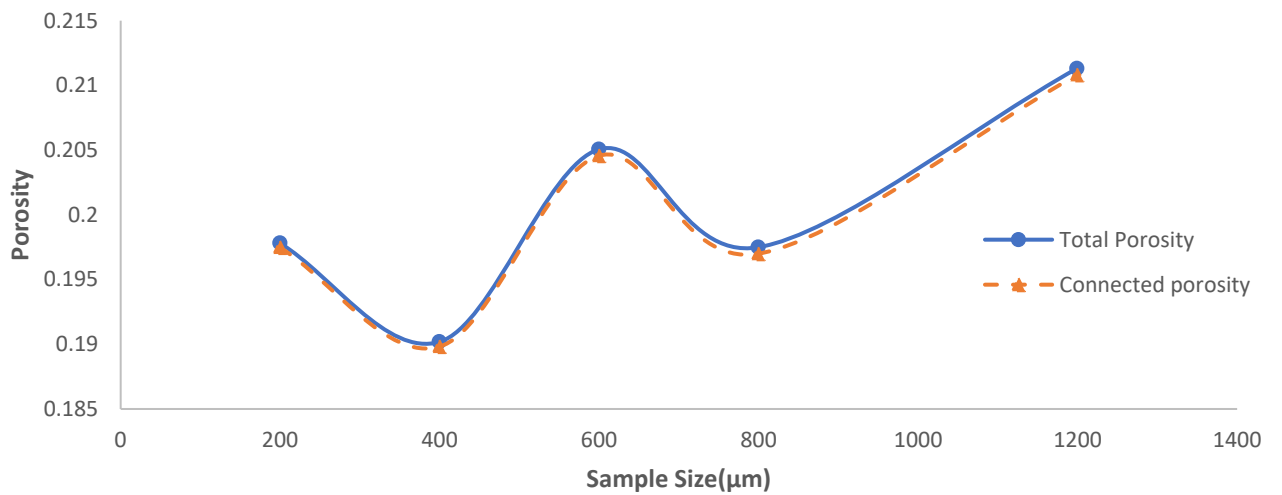

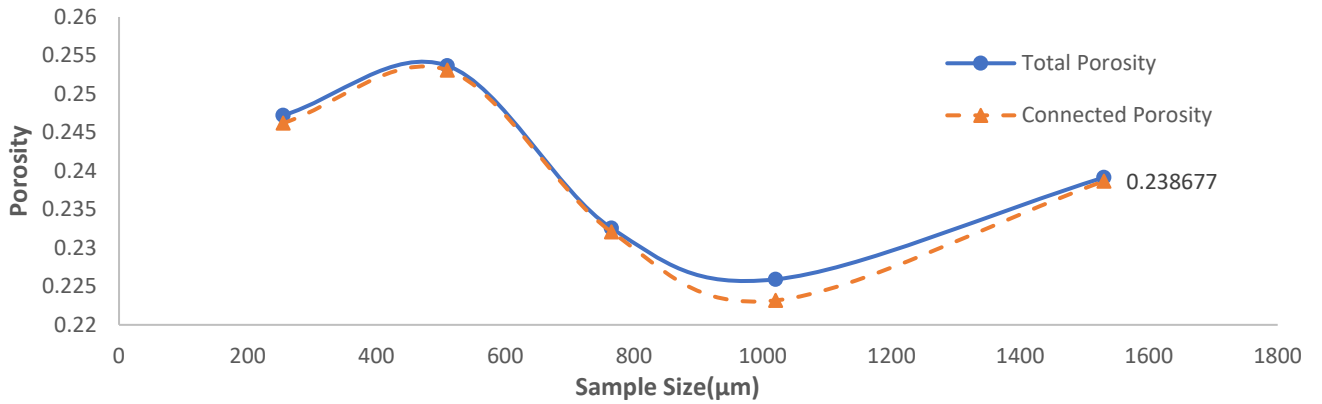**Figure 28 Porosity vs Sample Size (μm) for Sandstone S5 Sample**

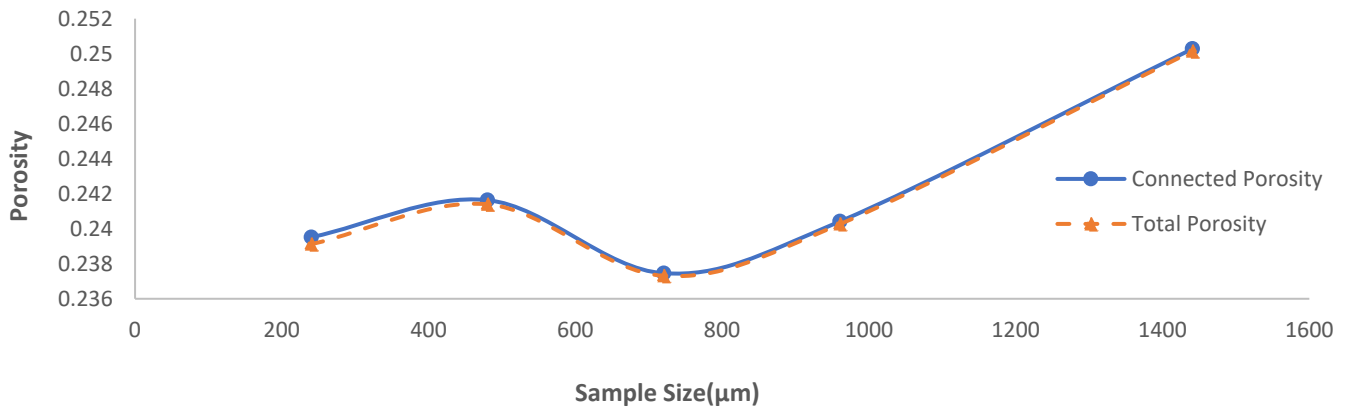**Figure 29 Porosity vs Sample Size (μm) for Sandstone S6 Sample**

Figure 30 Porosity vs Sample Size (μm) for Sandstone S7 Sample
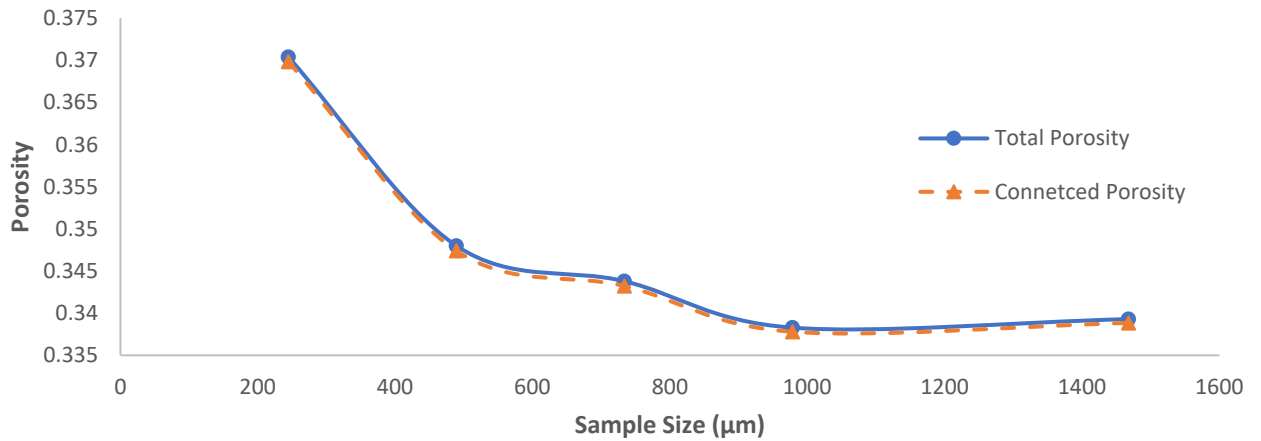

Figure 31 Porosity vs Sample Size (μm) for Sandstone S8 Sample
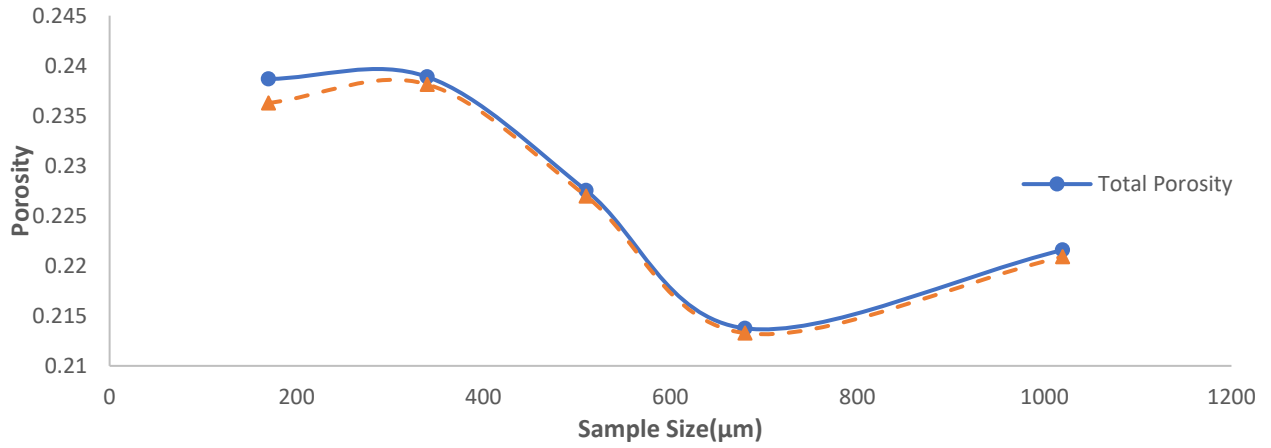
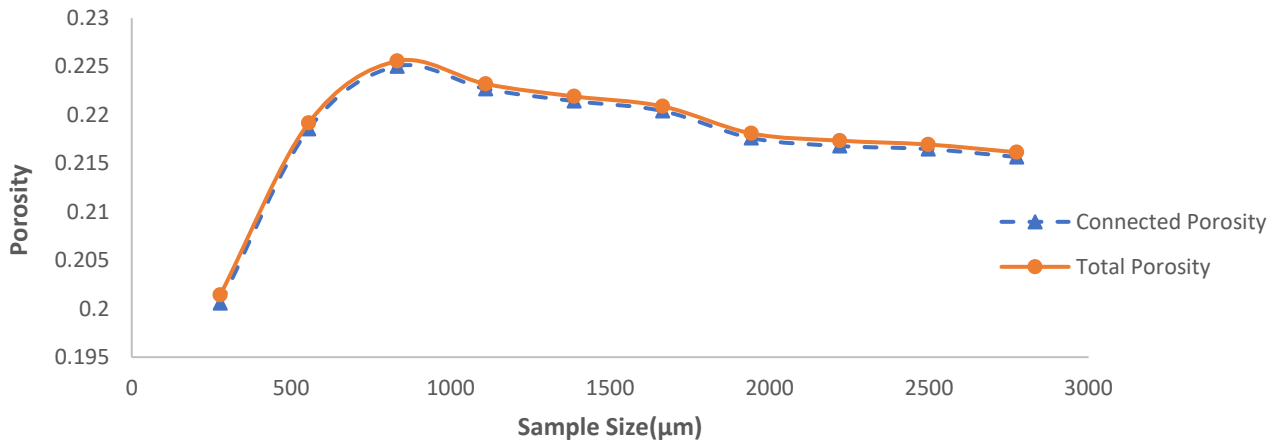**Figure 32 Porosity vs Sample Size (μm) for Sandstone S9 Sample**

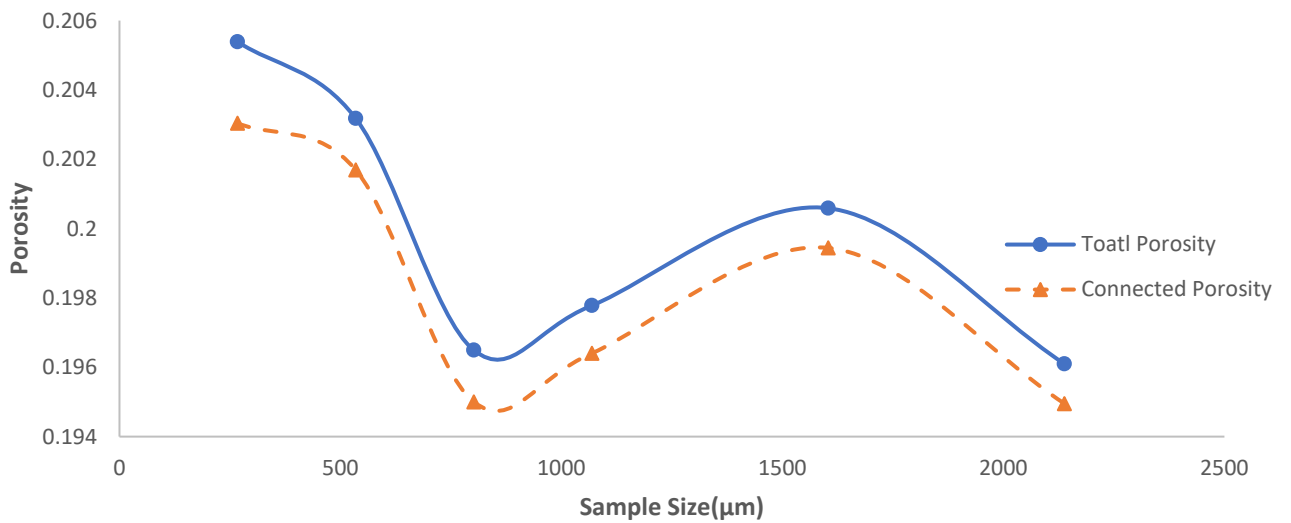**Figure 33 Porosity vs Sample Size (μm) for a Doddington Sandstone Sample**

Figure 34 Porosity vs Sample Size (μm) for a Berea Sandstone Sample
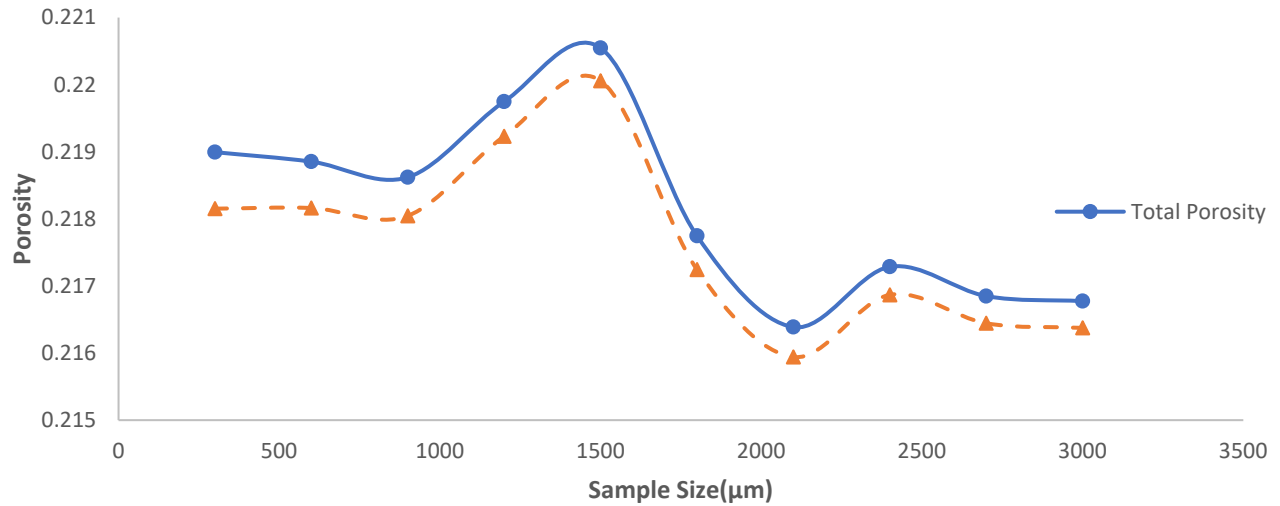
Figure 35 Porosity vs Sample Size (μm) for Bentheimer1 Sandstone Sample
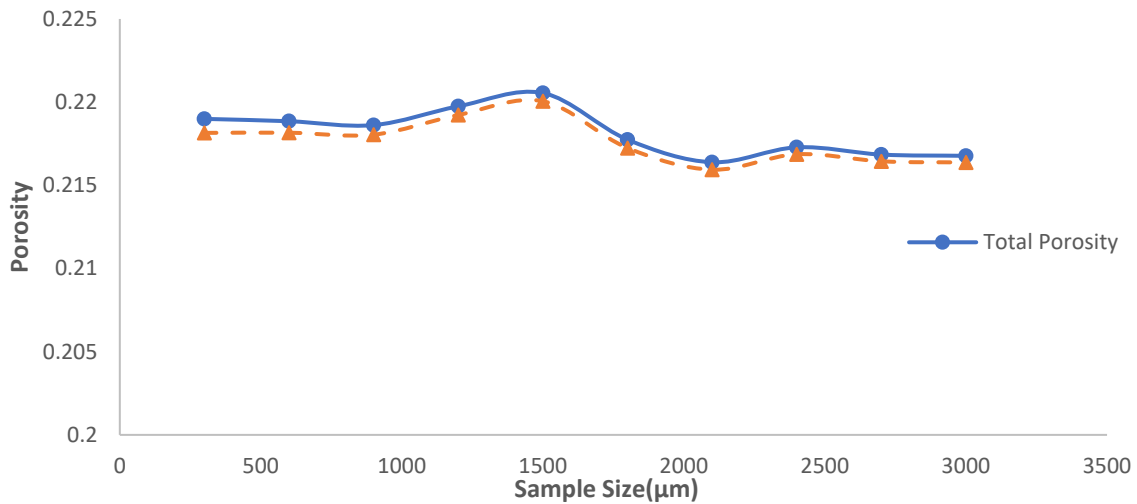
Figure 36 Porosity vs Sample Size (μm) for Bentheimer 2 Sandstone Sample

4.1.3. Porosity vs Sample Size for Carbonate

Figure 37 − Figure 41 display the porosity variation for carbonate samples, and these figures plot the total porosity and connected porosity for carbonate samples as the sample size increases. The total porosity of these five carbonate samples is between 13.3% and 23.1%, and the connected porosity is between 13.2% and 21.1%. What is striking in these figures is only the first three

samples have the same trend for connected porosity and total porosity curves, while the overall porosity curves of the other two sandstone samples have a notably different tendency.

For these carbonate samples in this study, the connected porosity and total porosity would increase as the sample size increases. Moreover, most of the time, the effective porosity outpaces the total porosity. For example, as sample size increased for sample C1, the connected porosity increases from 10.68% to 21.11%, while the total porosity rises from 13.96% to be 23.1%. For the other four carbonate samples, the connected porosity and total porosity increase by 1%~3%. Vuggy pores produced in carbonate samples might explain this.

Figure 37 Porosity vs Sample Size (µm) for Carbonate C1 Sample

Figure 38 Porosity vs Sample Size (µm) for Carbonate C2 Sample

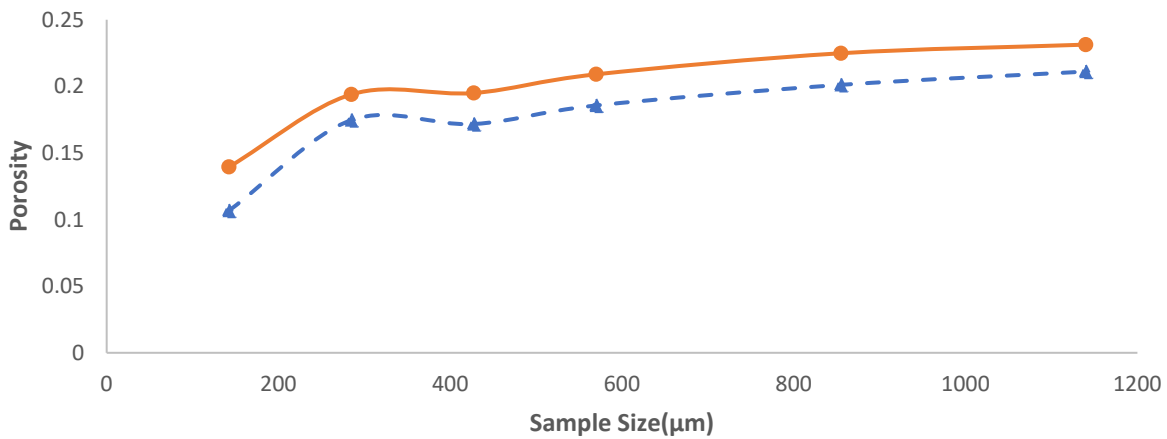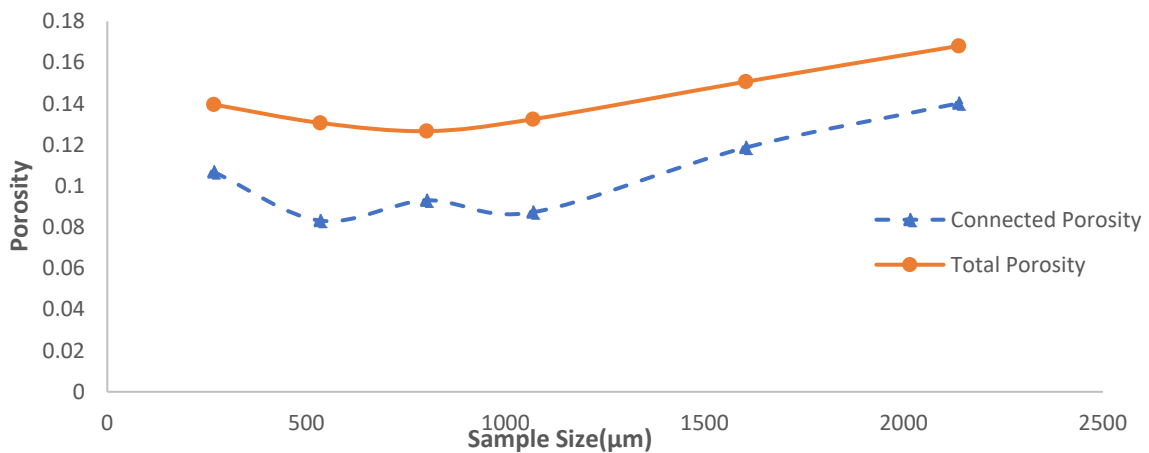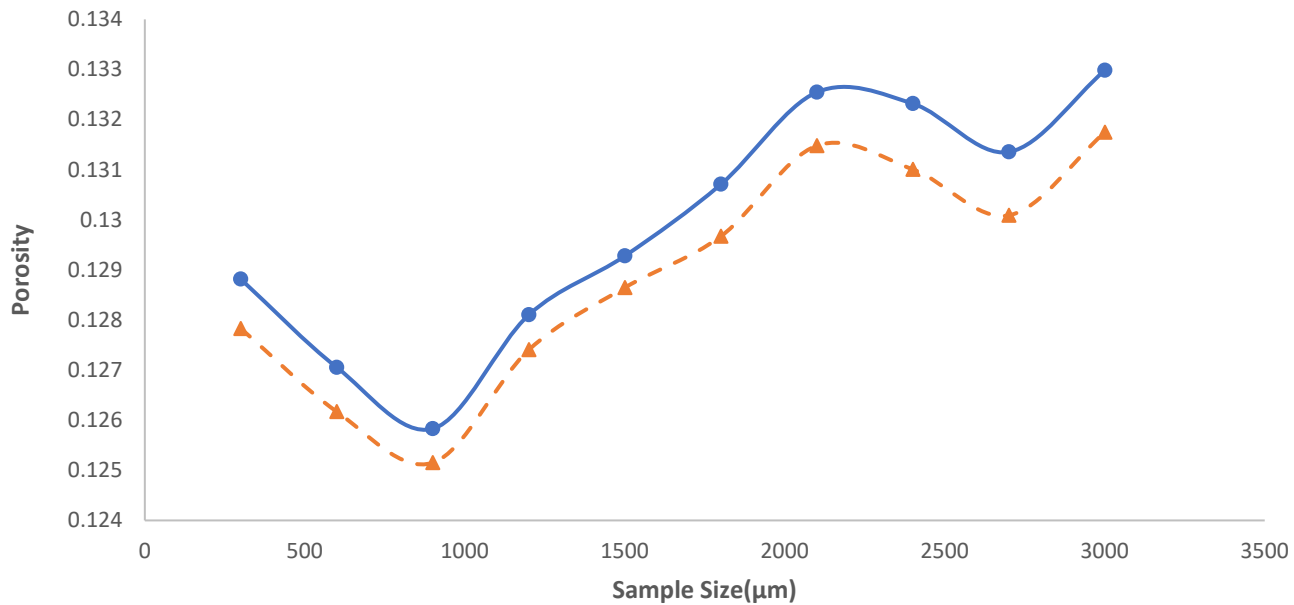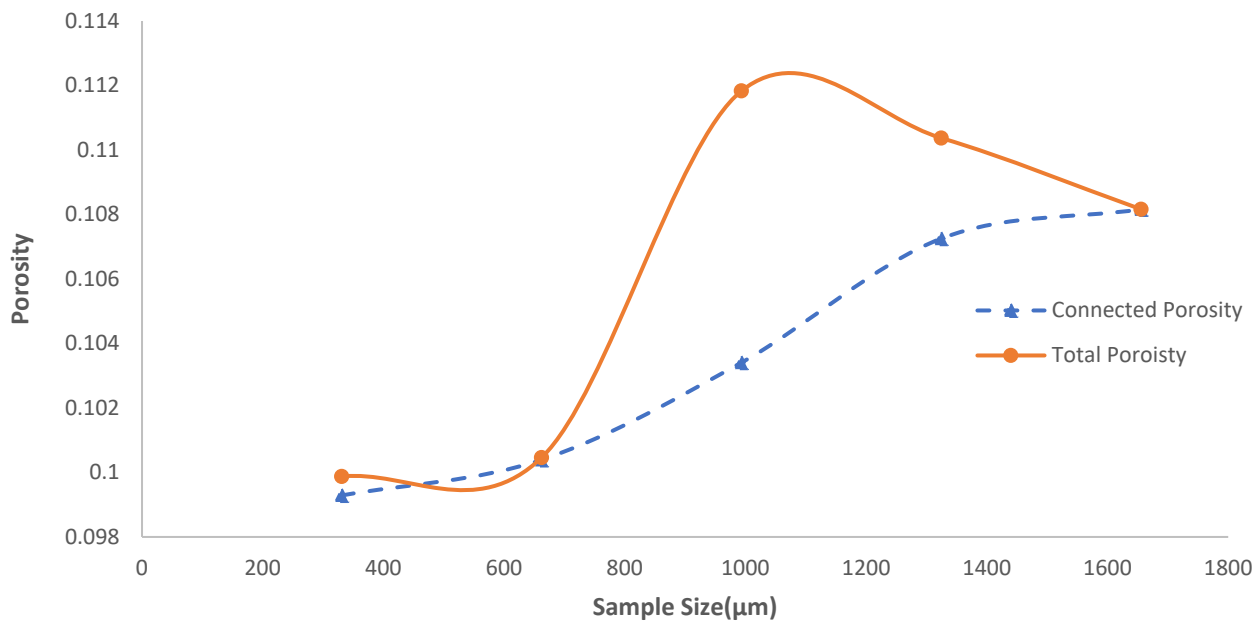**Figure 39 Porosity vs Sample Size (μm) for a Ketton Carbonate Sample**

Figure 40 Porosity vs Sample Size (μm) for Estaillades 1 Carbonate Sample
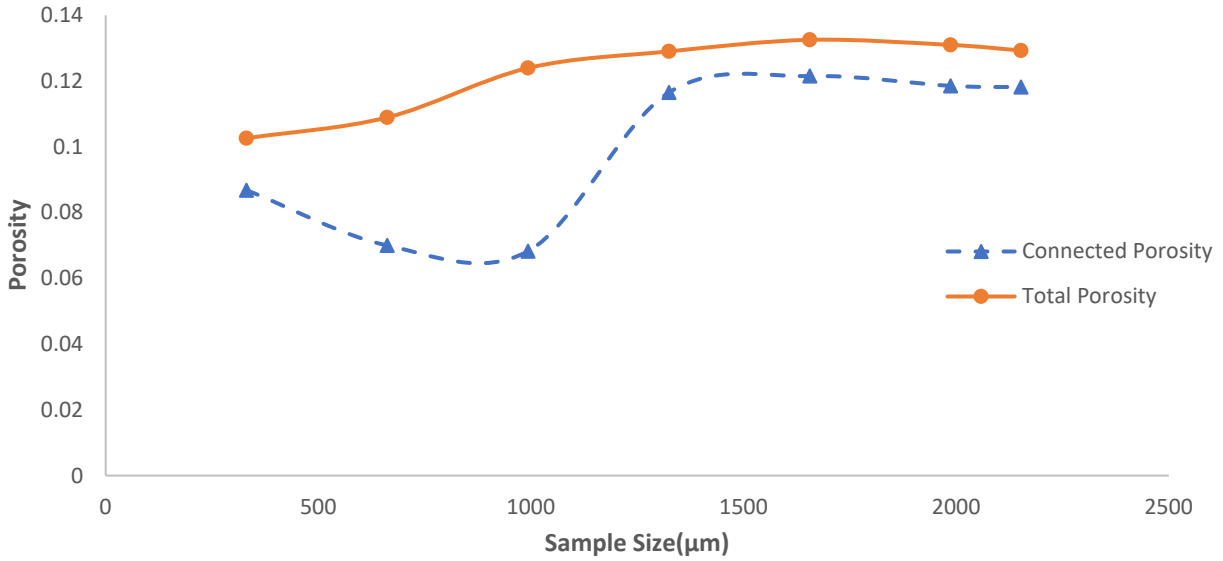
Figure 41 Porosity vs Sample Size (µm) for Estaillades 2 Carbonate Sample

4.1.4. Porosity vs Sample Size for Limestone samples

Figure 42 and Figure 43 present the connected and total porosity of Ketton limestone and Estaillades limestone samples as a function of sample size. As shown in Figure 42, the results of connected porosity and total porosity of Estaillades limestone fluctuates slightly as sample size increases. With the sample size increasing from 200µm to 2800µm, the total porosity ranges from 5.5% to 7.5%, and the connected porosity fluctuates from 3% to 5.5%. The connected porosity is almost half of the total porosity for the Estaillades limestone sample.

Figure 43 shows the distribution trend of connected porosity and total porosity of Ketton limestone. Quite clearly, the connected porosity and total porosity are greatly affected by the sample size in comparison with Estaillades limestone. The total porosity of Ketton limestone is bounded between 14.7% and 17.1%, and the connected porosity varies from 0.146 to 0.169. Given this, it is evident that the value of connected porosity and total porosity are close. It is somewhat unusual that the porosity distribution of Ketton limestone forms two camel curves, which have two

prominent tips. This might because the Ketton limestone sample is dissolved porous oolite limestone. However, because of a lack of limestone samples, the characteristics of porosity for limestone are hard to determine.
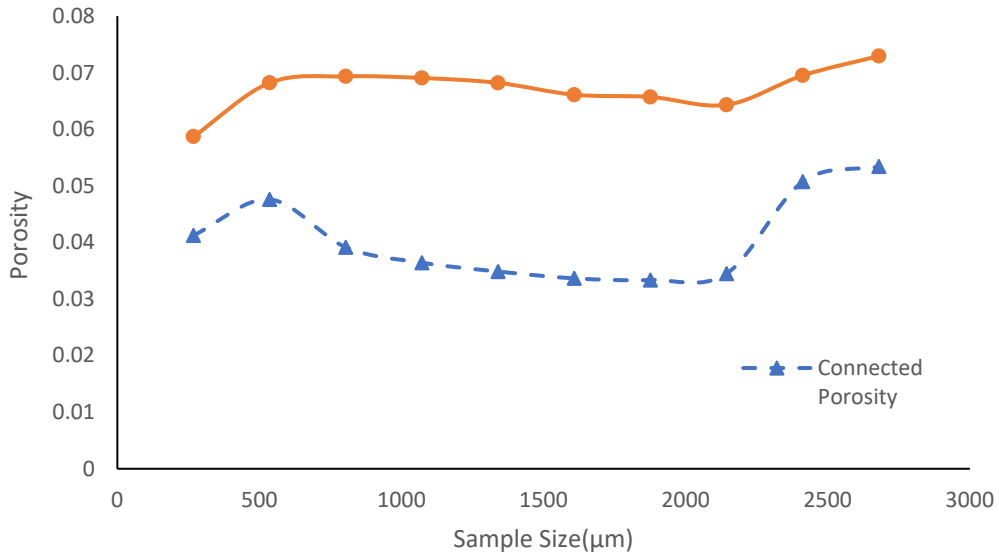

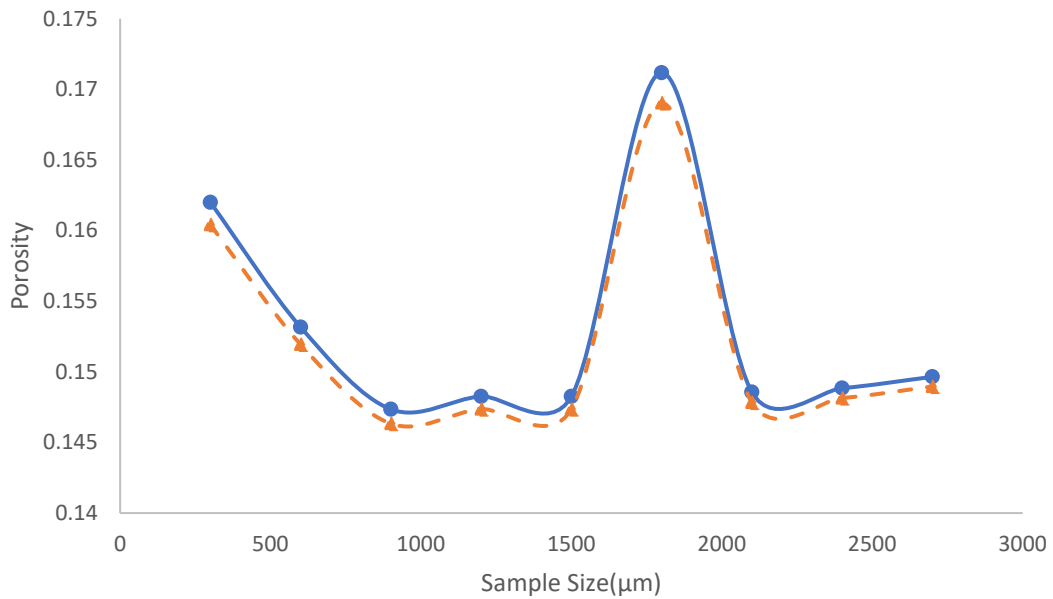**Figure 42 Porosity vs Sample Size (μm) for an Estaillades Limestone Sample**

Figure 43 Porosity vs Sample Size (μm) for a Ketton Limestone Sample

4.1.5 Porosity REV

By comparing the connected porosity and total porosity of these four types of rock samples, we find that the connected porosity and total porosity of the two shale samples are the lowest of the 22 samples in this study. In terms of the sample size, the connected and total porosity of the shale sample declines as the sample size increases, but for the carbonate samples, the connected and total porosity of them rise with the increasing sample size. For the limestone and sandstone samples of this study, both cases have occurred. This intriguing phenomenon with these samples may arise from their different representative elementary volume (REV). In the theory of composite materials, REV is the smallest volume over which a measurement can be made that will yield a value representative of the whole (Hill, 1963).

Robinson (2011) put forth that the porosity would have a random fluctuation on the microscopic spatial scale, i.e. in region I as shown in Figure 44. Bear (2002) considered that for homogeneous porous media, a minimum REV is defined as the left-hand boundary of region II. For heterogeneous porous media, REV can theoretically be achieved at scales intermediate between the erratic fluctuations of region I and the macroscopic heterogeneity of region III, although the presence of region II for real heterogeneous systems may be difficult to delineate with confidence (Zhang et al., 2000; Baveye et al., 2002; Robinson et al., 2010). The samples of this study accord with the previous observations.
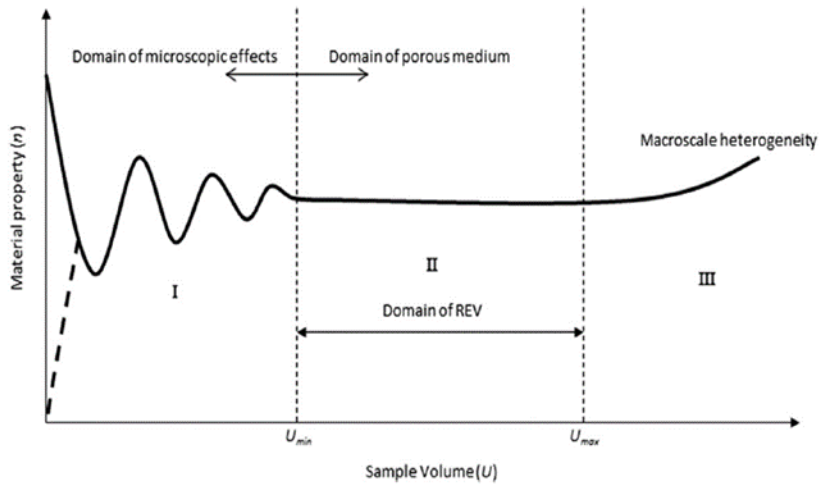
Figure 44 Conceptual Scheme Representing the Idealized Relationship Between Material Property (n) and the Sample Volume (U) and Showing the Representative Elementary Volume Region. (Robinson et al., 2011, Taiwo et al., 2016)

For the shale samples in this study, they might not reach their REV, resulting in a total porosity and connected porosity that gradually drops as the sample size increases. For the other three types of rock, the sample size of them might surpass the domain of REV, which would lead to the connected porosity and total porosity rising as sample size increases. Moreover, since the rocks have different lithofacies, their REV values are different, the porosity REV for the cube geometry ranged between 0.37 and 2.0 mm, depending on the porous medium, which is equivalent to approximately 1–7 grain diameters (Robinson et al., 2010). According to the porosity distribution, we could determine that the REV of sandstone samples S3, S4, S8 are around 1.7mm, and that the REV of Estaillades limestone is about 1mm, both of which are consistent with the above conclusion.

4.2 Pore Radius Distribution

In this section, the pore size distributions of all samples in this study are plotted. Assuming cylindrical shape for the pores, the pore size distribution of shale samples is analyzed by measuring

the area of each orifice from 2D images. This calculation of pore size may include some deviations from the actual results, since the pore area should be the accumulation of the real solid points in pore space. The pore size distribution of samples is displayed by calculating the probability distribution and the number of pores with different pore radii. Each sample's pore radius probability distribution follows the Gaussian distribution $F(x)= \frac{1}{\sigma\sqrt{2\pi}}e^{-\frac{(x-u)^{2}}{2\sigma^{2}}}$ (Zhang, Moghanloo & Davudov, 2019).

4.2.1 Pore Radius Distribution for Shale Samples

As can be seen in Figure 45 to Figure 47, all observed pores of Eagle Ford shale and Marcellus shale samples are in the orders of nanoscale and microscale. For the Eagle Ford shale sample, the minimum observed pore radius is 5 nm limited by the image resolution; the effective pore size distribution of the Eagle Ford sample is bounded between 0.01 and 1μm. For the Marcellus shale sample, the minimum pore radius is around 1nm, and the maximum pore radius is near 1μm. Like the Eagle Ford shale sample, the effective pore radius of Marcellus ranges from 0.01 and 1μm. Furthermore, the pores in the Marcellus shale sample outnumbers those in the Eagle Ford shale sample, especially those with a radius between 0.01 and 0.1 micrometer.
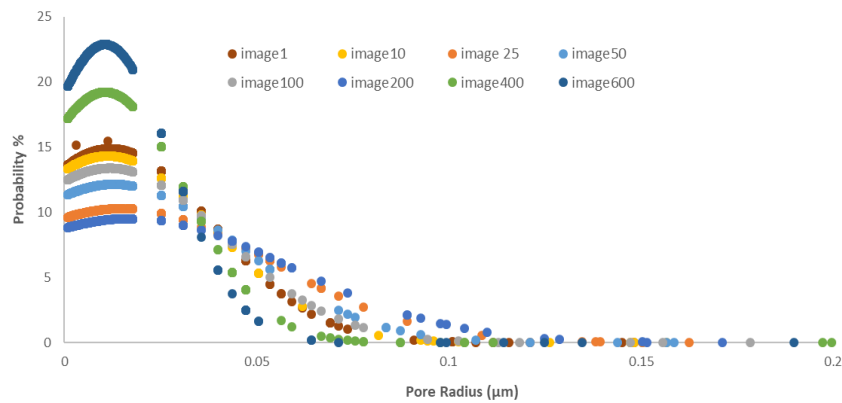

Figure 45 Pore Radius Distribution Function for an Eagle Ford Shale Sample (Zhang et al., 2019)
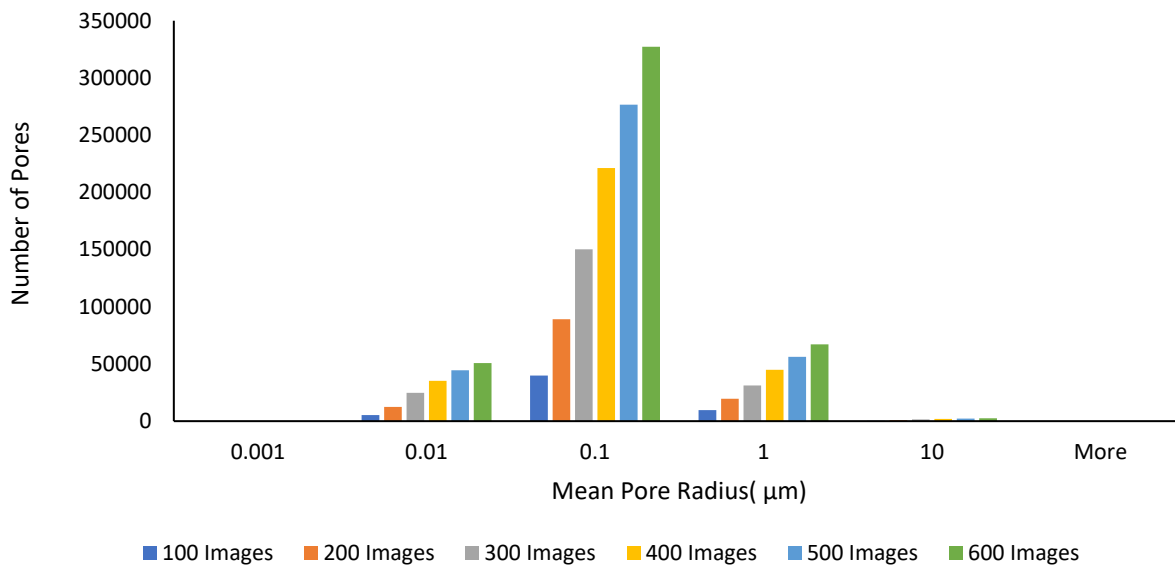
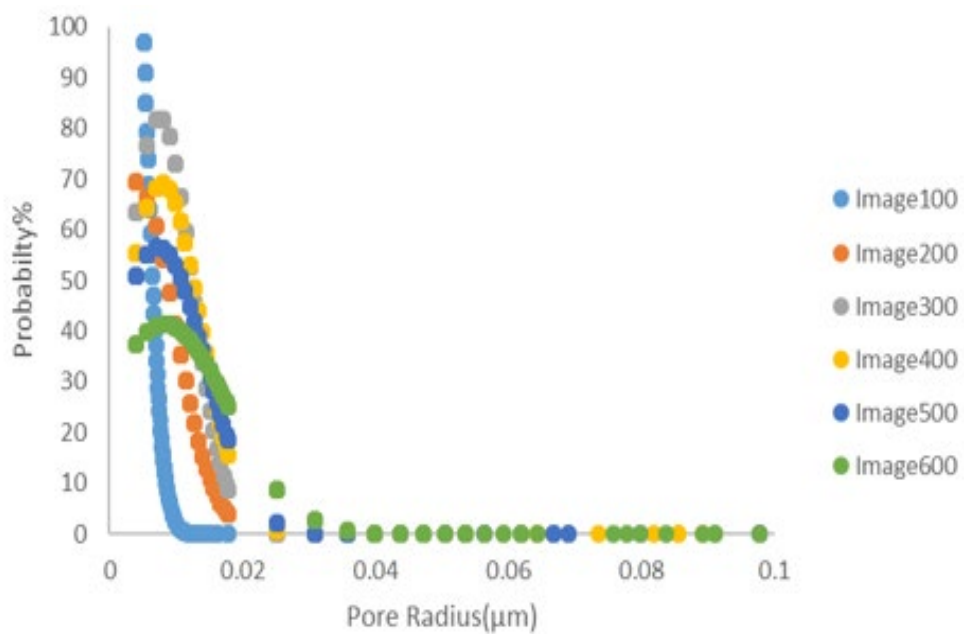**Figure 46 Histogram of Pore Radius for an Eagle Ford Shale Sample**

Figure 47 Pore Radius Distribution Function for a Marcellus Shale Sample
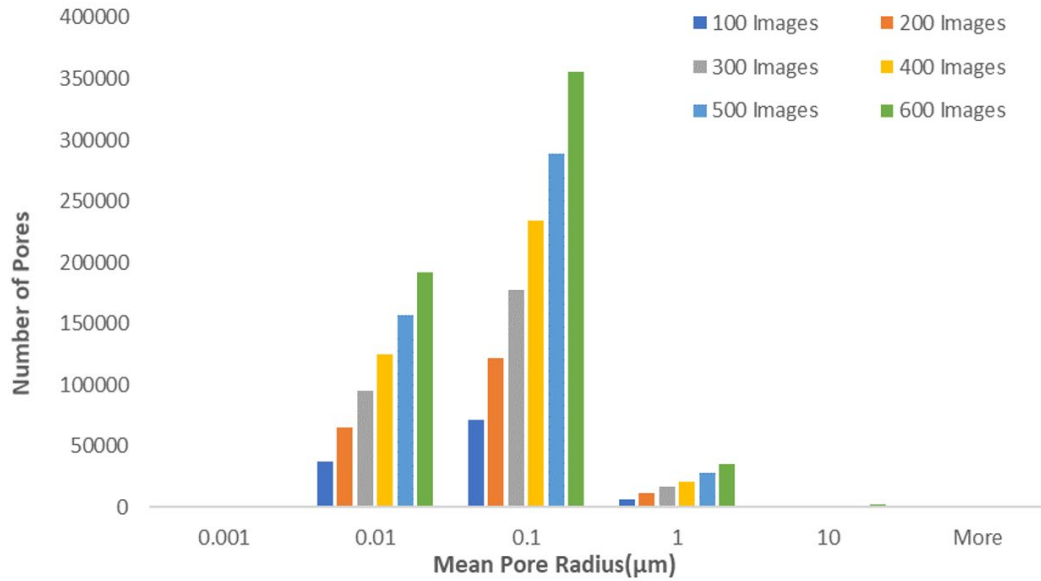
Figure 48 Histogram of Pore Radius for a Marcellus Shale Sample

4.2.2 Pore Radius Distribution for Sandstone Samples

Figure 49 − Figure 58 present the pore size distribution of the 10 sandstone samples. As shown in the graphs and histograms, the equivalent pore radius of each sample ranges from 10 to 300μm, except for the Berea sandstone sample, for which the pore radius ranges from 0.01 to 30μm. The difference might be due to the lower image resolution for the Berea sandstone sample than those for the other nine samples. Contrary to the curves of shale samples, the overall pore size distribution for all sandstone samples is normal, without scattered points. Furthermore, what stands out in these figures is that more than half of the pores are between 10 and 50 μm, meaning that the range of effective pore radius is ten or hundred times more massive than that of shale samples.
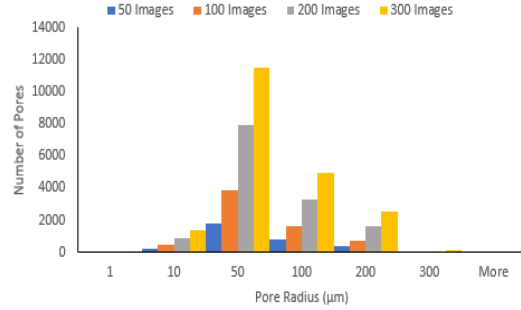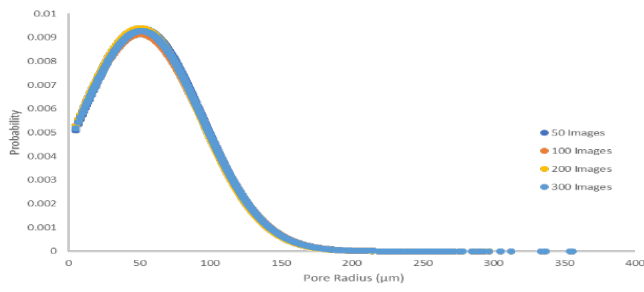
Figure 49 (a) Pore Radius Distribution Function (b) Histogram of Pore Radius for Sandstone S1 Sample
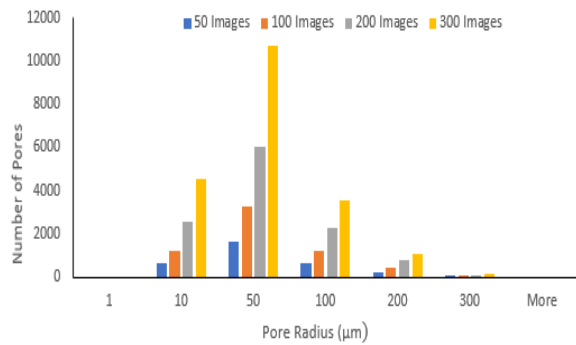

Figure 50 (a) Pore Radius Distribution Function (b) Histogram of Pore Radius for Sandstone S2 Sample

Figure 51 (a) Pore Radius Distribution Function (b) Histogram of Pore Radius for Sandstone S3 Sample

Figure 52 (a) Pore Radius Distribution Function (b) Histogram of Pore Radius for Sandstone S4 Sample

Figure 53 (a) Pore Radius Distribution Function (b) Histogram of Pore Radius for Sandstone S5 Sample
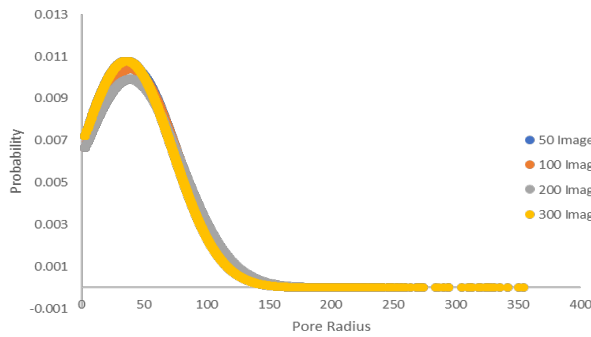

Figure 54 (a) Pore Radius Distribution Function (b) Histogram of Pore Radius for Sandstone S6 Sample

Figure 55 (a) Pore Radius Distribution Function (b) Histogram of Pore Radius for Sandstone S7 Sample
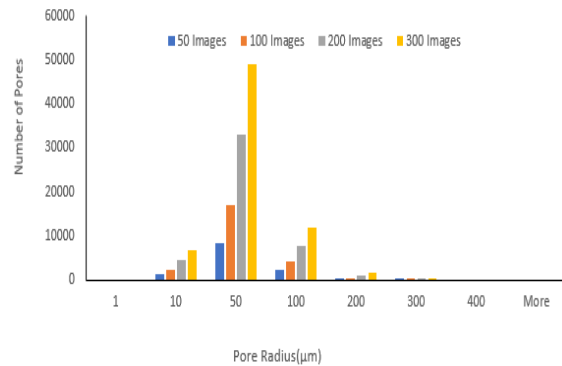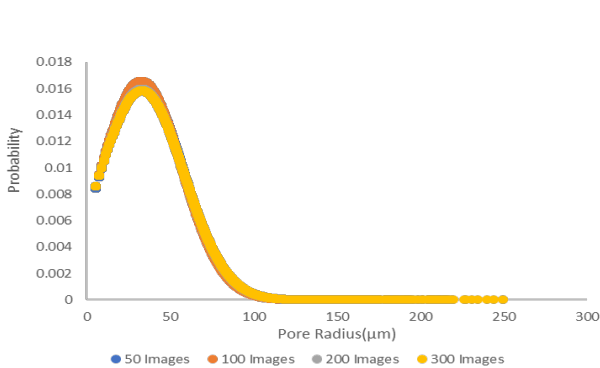

Figure 56 (a) Pore Radius Distribution Function (b) Histogram of Pore Radius for Sandstone S8 Sample
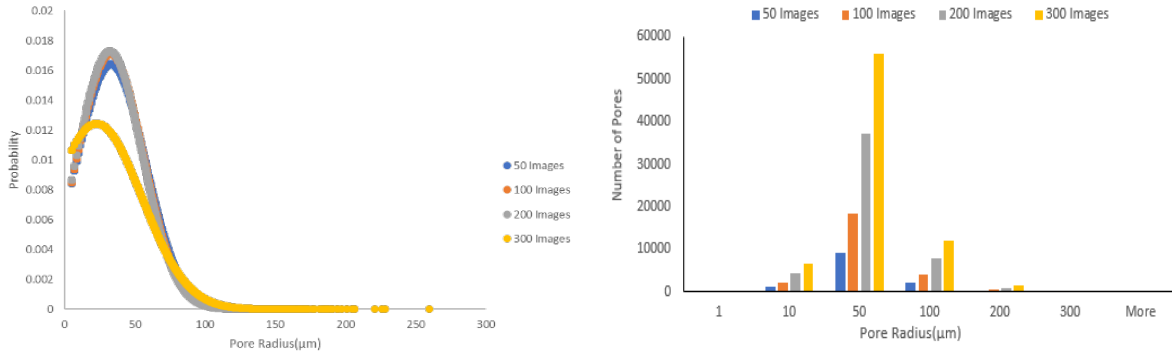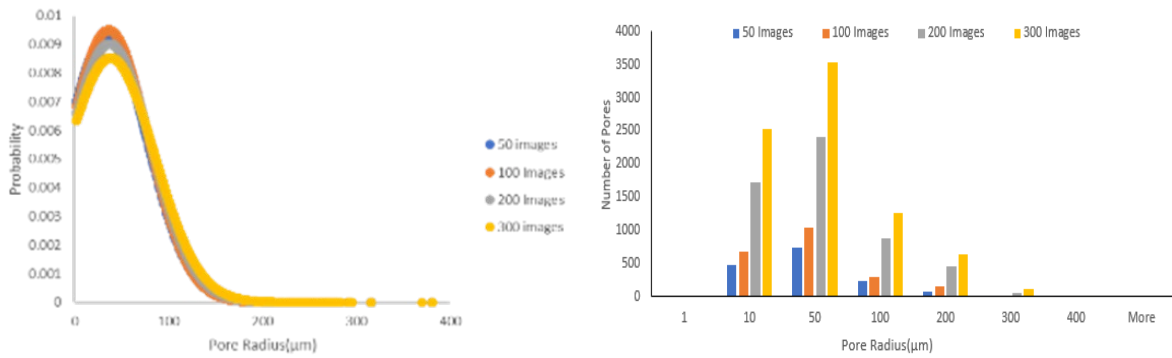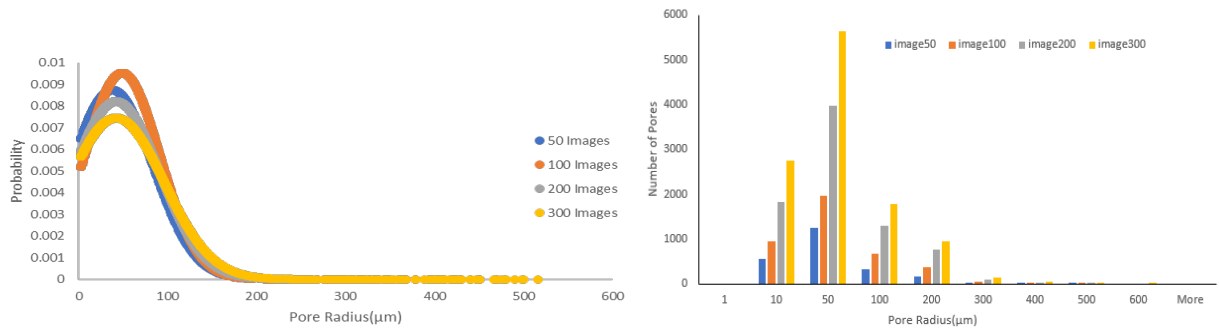

Figure 57 (a) Pore Radius Distribution Function (b) Histogram of Pore Radius for Sandstone S9 Sample

Figure 58 (a) Pore Radius Distribution Function (b) Histogram of Pore Radius for a Berea Sandstone Sample

4.2.3 Pore Size Distribution for Carbonate Samples

The pore size distribution of the two carbonate samples is shown from Figure 59 to Figure 60. For carbonate C1 − C2, there is no difference from sandstone S1 − S9. The effective radius of pores is bounded between 10 and 200μm. But for carbonate sample C1, the 10μm pores account for a substantial proportion, while the sandstone samples and carbonate sample C2 contain a more significant number of 50μm pores.
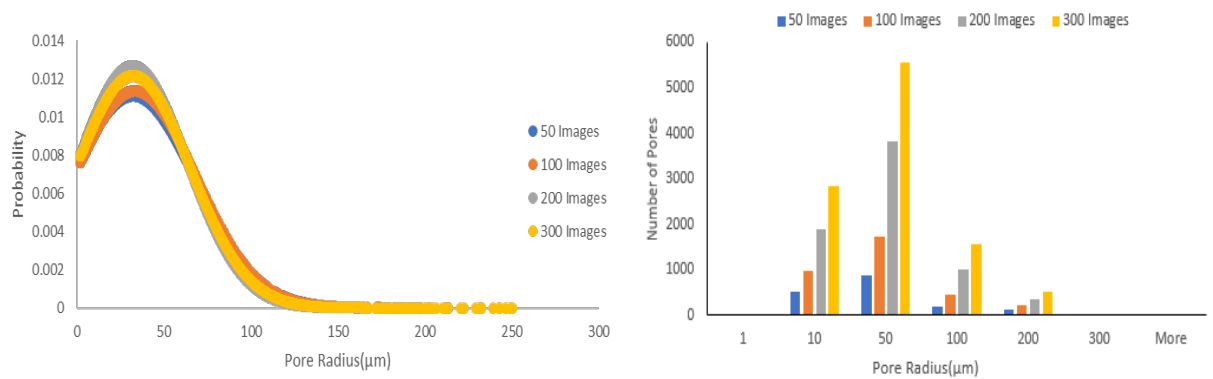

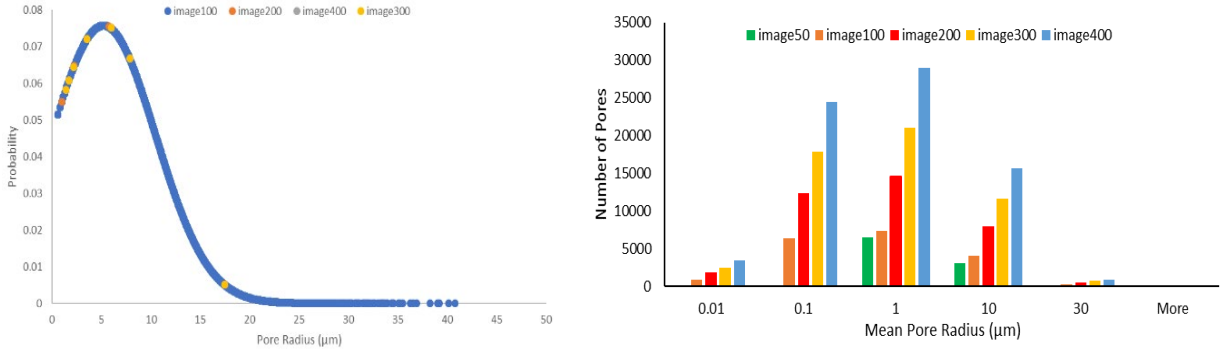**Figure 59 (a) Pore Radius Distribution Function (b) Histogram of Pore Radius for Carbonate C1 Sample**
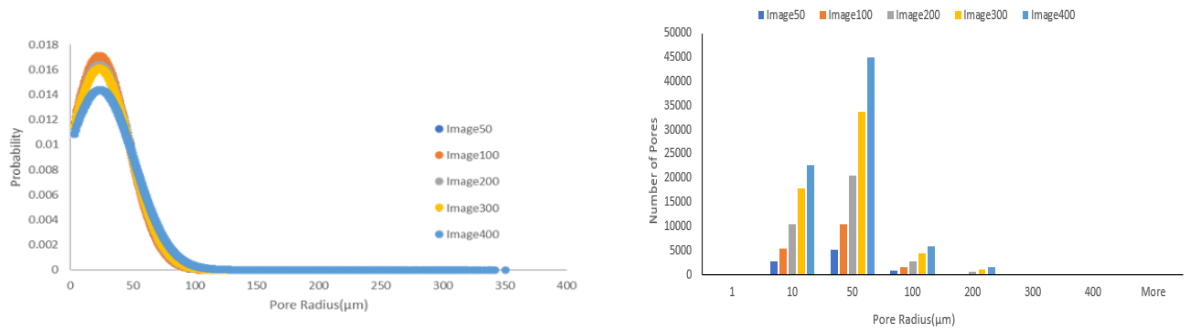
Figure 60 (a) Pore Radius Distribution Function (b) Histogram of Pore Radius for Carbonate C2 Sample

4.2.4 Pore Size Distribution for Limestone Samples

Figure 61 and Figure 62 depict the pore radius distribution of two limestone samples. As shown in Figure 61, the pore size distribution of Ketton limestone from a discontinuous curve like shale sample (e.g. Eagle Ford). The effective pore radius distribution of Ketton limestone is bounded between 1 and 100μm, whereas the pore radius distribution of Estaillades limestone is a continuous curve similar to sandstone and carbonate samples(as shown in Fig. 62), and its effective radius is between 10 and 100μm, like those of sandstone and carbonate.
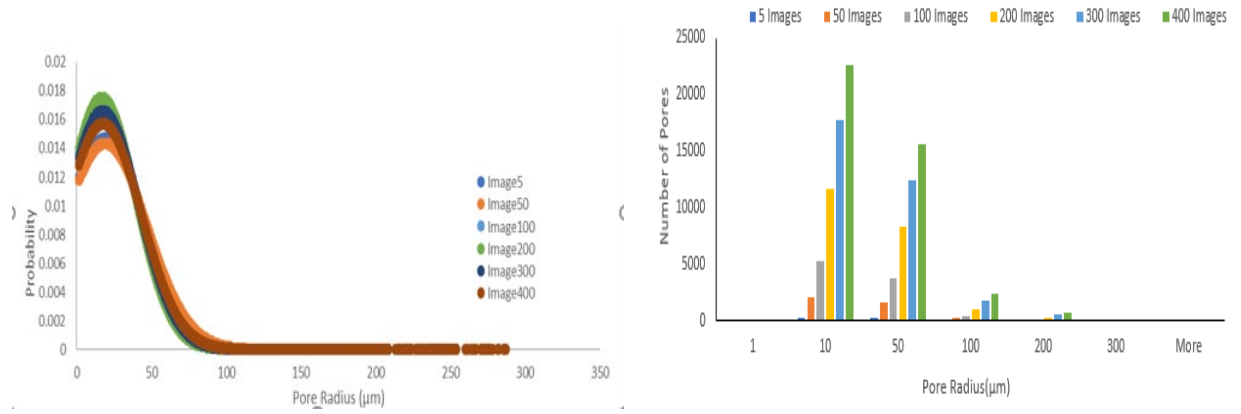

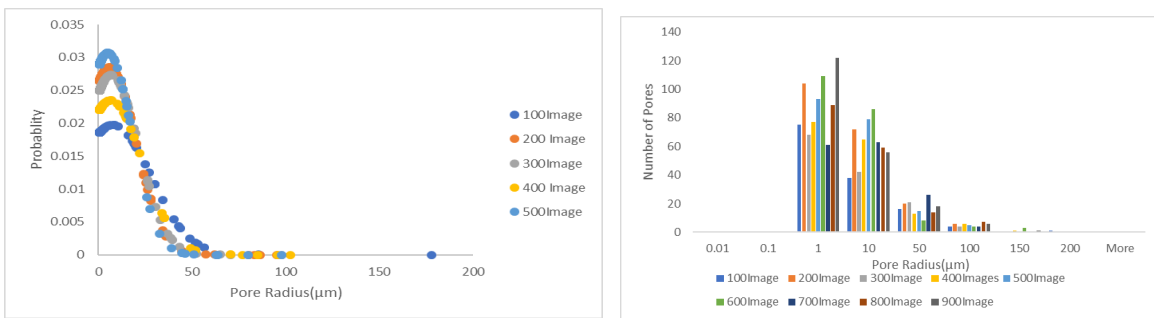**Figure 61 (a) Pore Radius Distribution Function (b) Histogram of Pore Radius for a Ketton Limestone Sample**
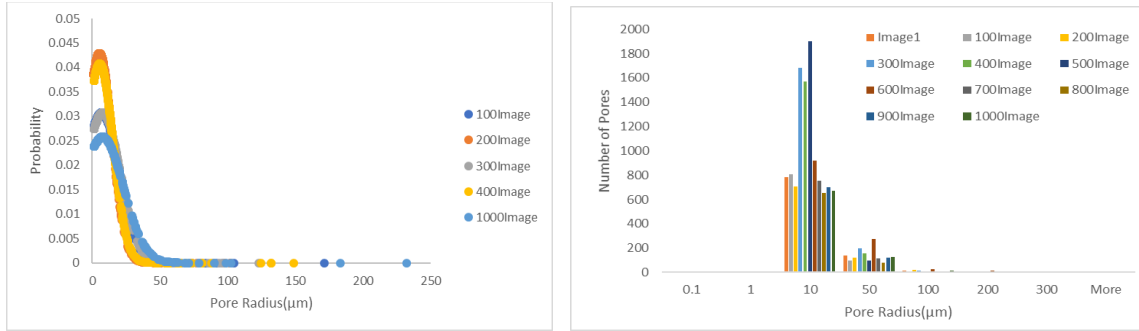
Figure 61 (a) Pore Radius Distribution Function (b) Histogram of Pore Radius for an Estaillades Limestone Sample

4.3. Throat Radius Distribution

In general, the pore structure characteristics of rocks pertain to the geometric shape, size, interconnection relation of the pores, and throat of rocks, which can be divided into the geometric structure and topological structure. "Pore throat" refers to a narrow channel connecting pores in rock mass or soil mass. The size of the throat often has a significant influence on permeability. The larger the throat is, the more fluid can flow in rock or soil mass. The pore structure schematic diagram is shown in Figure 63, which also describes the difference between pore and throat. For reservoir rocks, pores reflect the reservoir storage capacity for fluid, while the throat controls the fluid transport capacity within the reservoir. The throat size of samples thus plays a vital role in the analysis of pore structure. In this chapter, the Avizo® Label Analysis module is applied to compute and compare a set of measures for each 3D reconstructed image, such as the throat radius, connected pores radius, and total pore radius. In theory, Avizo® assumes that the equivalent diameter measure computes the diameter of the spherical particle of the same volume for a particle. So, the equivalent diameter of pores and throats are given by the following formula: Equivalent

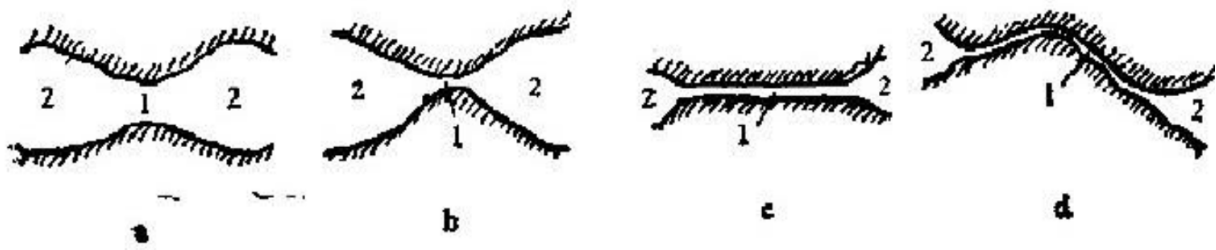Diameter $= \sqrt[3]{\frac{6 \times Volume3d}{\pi}}$.

Figure 62 The Diagram of Pore Bodies and Pore Throats (1 is pore throat, 2 is pore body)

4.3.1 Throat Radius Distribution for Shale Samples

Figure 64 plots the radius distribution of connected pores, total pores, and pore throats for the whole Eagle Ford shale sample. As Figure 64 points out, the peak points of the three distribution curves are distinct. As a result of the vertices of the normal distribution corresponding to the average of the data, the mean radius of connected pores is larger than the mean radius of total pores and throats.

As shown in Figure 65, the mean radius of connected pores is approaching 0.1μm, which is two times higher than the mean radius of total pores. Also, the total pore radius distribution roughly overlaps with and throats radius distribution except for the peak point. Figure 65 describes the effective throat radius distribution; the effective radius of the throat is in the range of 0.01 and 1μm, which is the same as the pore radius distribution.
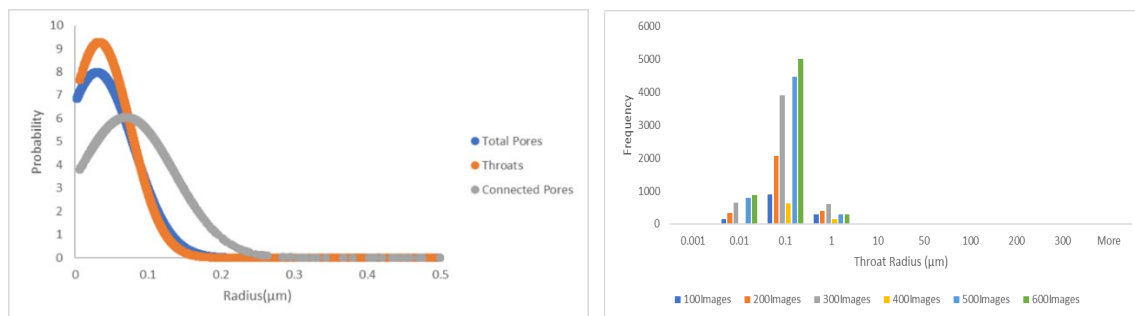

Figure 63 Throat Radius Distribution Function (b) Histogram of Throat Radius for an Eagle Ford shale Sample
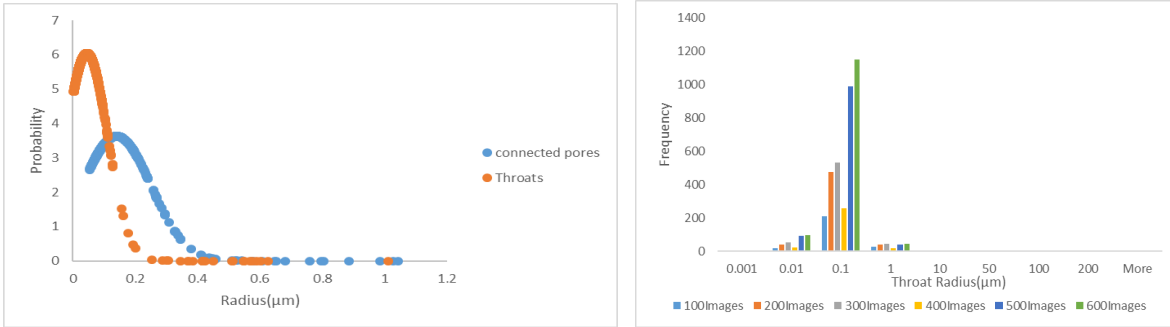
Figure 64 Throat Radius Distribution Function (b) Histogram of Throat Radius for a Marcellus shale Sample

4.3.2 Throat Radius Distribution for Sandstone Samples

In this section, nine sandstone samples are measured and compared with each other. Figures 66 − 74 below reveal the radius distribution of connected pores, total pores, and throats for sandstone samples S1− S9. What is striking in these figures is that the curve of sandstone samples each have a different vertex. The distribution of the throat radius has very high vertices, but it corresponds to the smallest radius with 10-20μm. Conversely, the distribution curve of connected pore radius always has the largest mean pore radius (50 − 70μm). The curve of the total pore radius distribution is between them and closer to the distribution curve of connected pores, which indicates that the connected pores always have a bigger radius. Further, the histograms describe that the effective radius of throats for the nine sandstone samples varies from 10 to 100μm; the number of throats with 50μm forms a significant portion of total throats.

Figure 65 Throat Radius Distribution (b) Histogram of Throat Radius for a sandstone S1 Sample

Figure 66 Throat Radius Distribution (b) Histogram of Throat Radius for Sandstone S2 Sample

Figure 67 Throat Radius Distribution (b) Histogram of Throat Radius for Sandstone S3 Sample

55

Figure 68 Throat Radius Distribution (b) Histogram of Throat Radius for Sandstone S4 Sample

Figure 69 Throat Radius Distribution (b) Histogram of Throat Radius for Sandstone S5 Sample

Figure 70 Throat Radius Distribution (b) Histogram of Throat Radius for Sandstone S6 Sample

Figure 71 Throat Radius Distribution (b) Histogram of Throat Radius for Sandstone S7 Sample
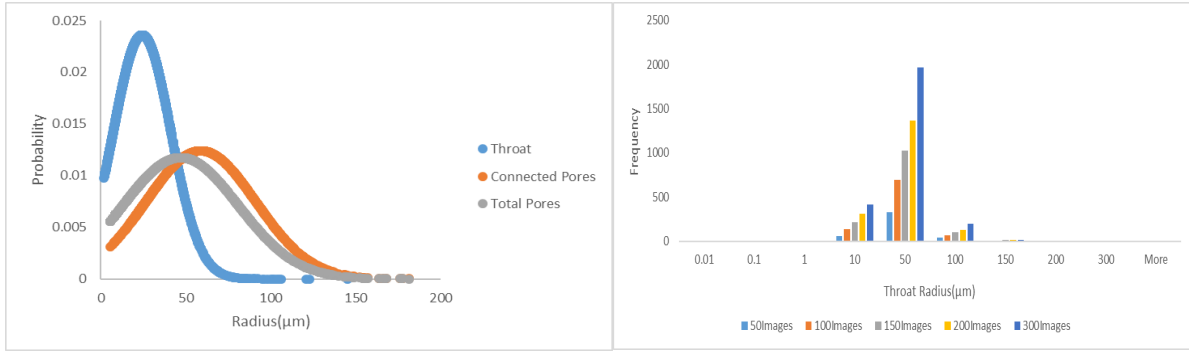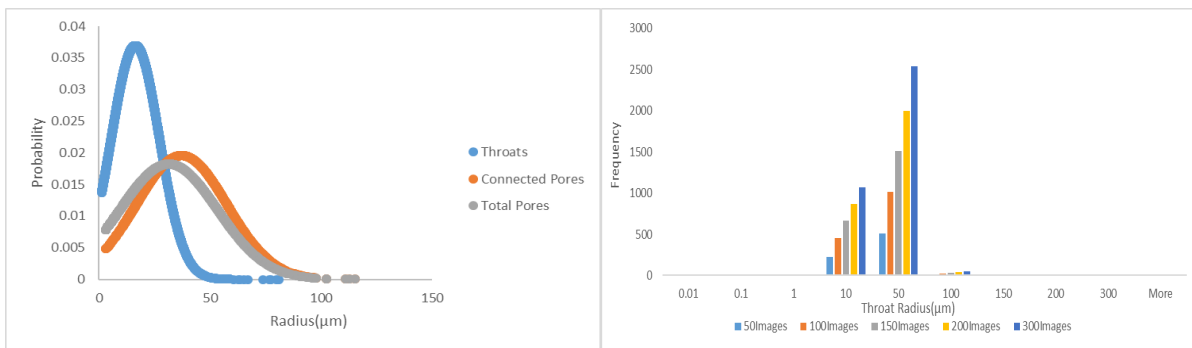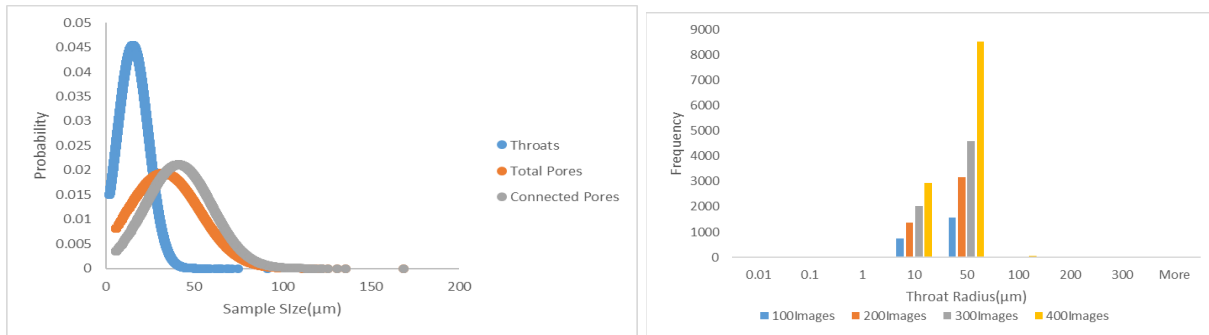

Figure 72 Throat Radius Distribution (b) Histogram of Throat Radius for Sandstone S8 Sample

Figure 73 Throat Radius Distribution (b) Histogram of Throat Radius for Sandstone S9 Sample
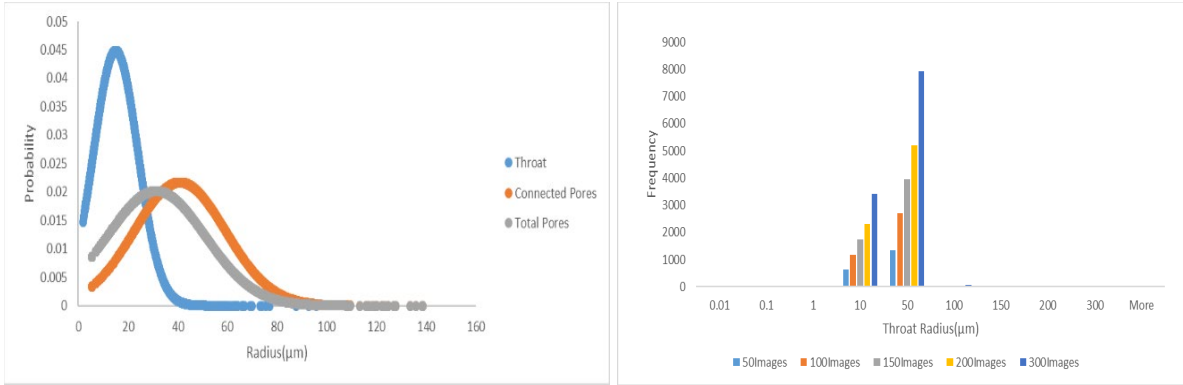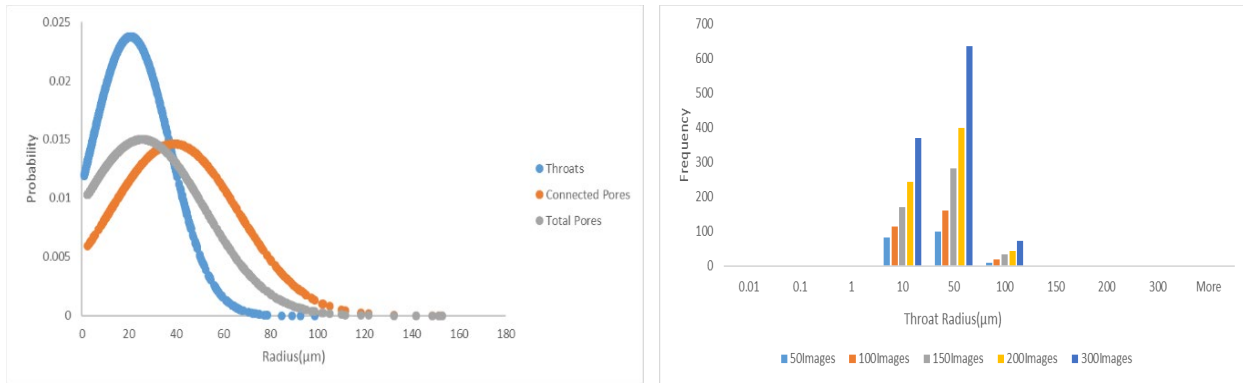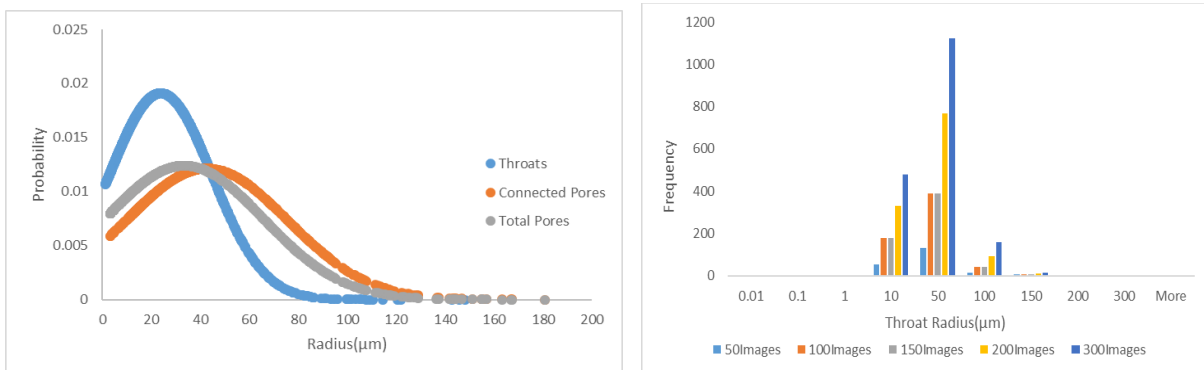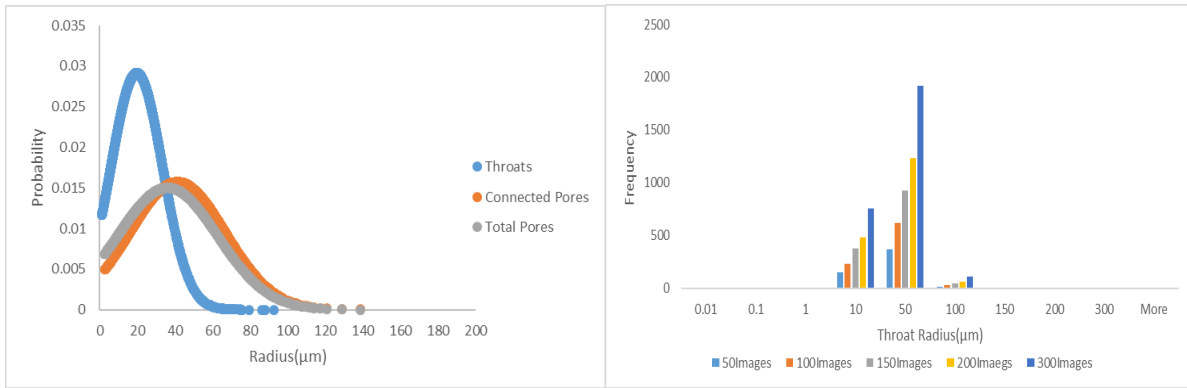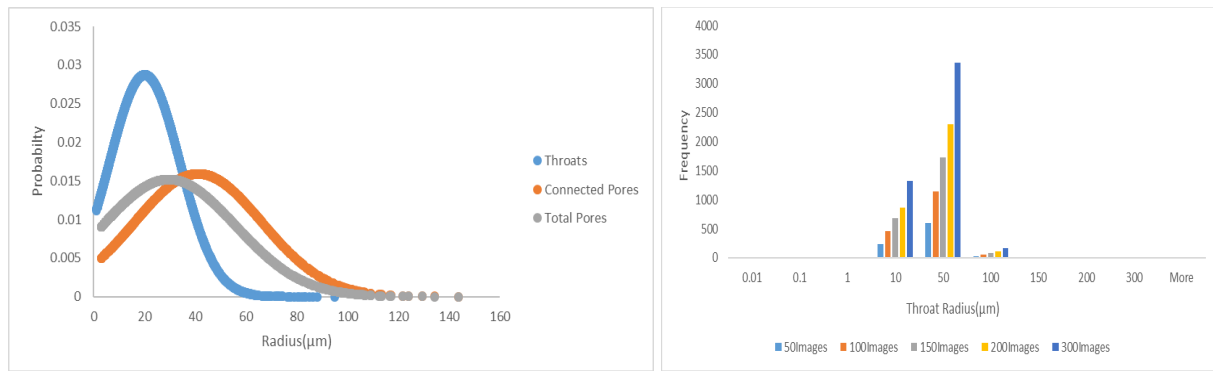
4.3.3 Throat Radius Distribution for Carbonate Samples

Figure 75 and Figure 76 depict the pore and throat distribution of carbonate samples. More obviously, the distribution curves of connected and total pores overlap entirely with each other,

which might indicate that all pores in these carbonate samples are connected. For carbonate samples in this section, the distributions of connected pores and total pores distribution have a broad range, from 0 to100µm, and their mean radius is all around 30µm. For the distribution curves of throats, their peak point is at the mean throat radius of 20µm, and the effective radius of throats ranges from 10 and 100µm. The throats with 50µm account for a large part of total throats, similar to sandstone samples.

Figure 74 Throat Radius Distribution (b) Histogram of Throat Radius for Carbonate C1 Sample
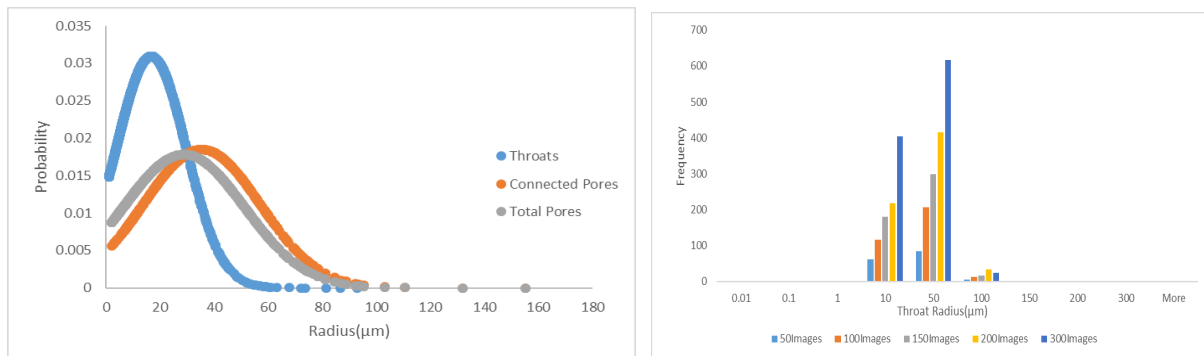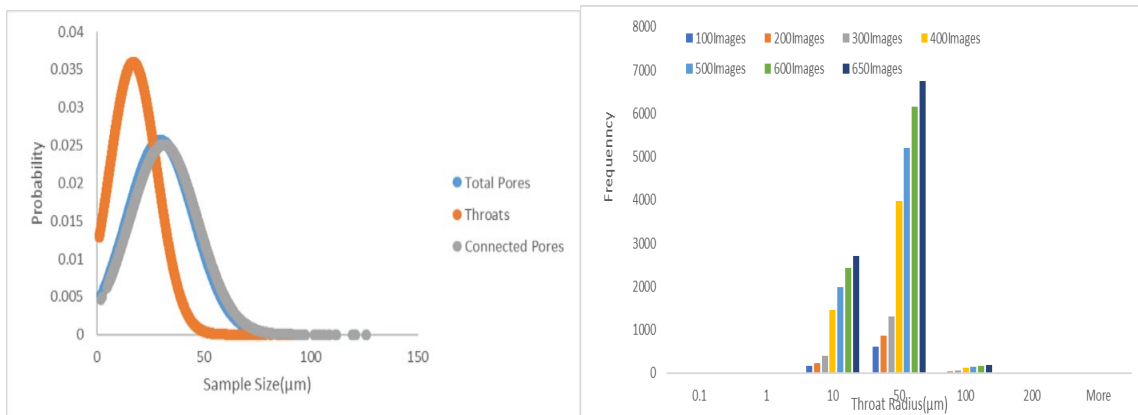

Figure 75 Throat Radius Distribution (b) Histogram of Throat Radius for Carbonate C2 Sample

4.3.4 Throat Radius Distribution for Limestone Samples

In this section, Figure 77 and Figure 78 show the radius distribution of connected pores, total pores, and total throats for Ketton limestone and Estaillades limestone. Comparing the two

limestone types yields a noteworthy difference between them. The Ketton limestone shows an interesting phenomenon: the full pore radius distribution overlaps with the distribution of throat radius in Ketton limestone. Yet, for the Estaillades limestone, the distribution of connected pores and total pores overlap entirely with each other. The mean throat radii of Ketton limestone and Estaillades limestone are around 25 and 50µm, respectively. The effective throat radius of Ketton limestone is bounded between 10 and 100µm; with throats of the 10µm radius making up a large percentage of total throats. For the Estaillades limestone, the effective throat radius ranges from 1 to 50µm, and this sample also has a large number of 10µm throats.
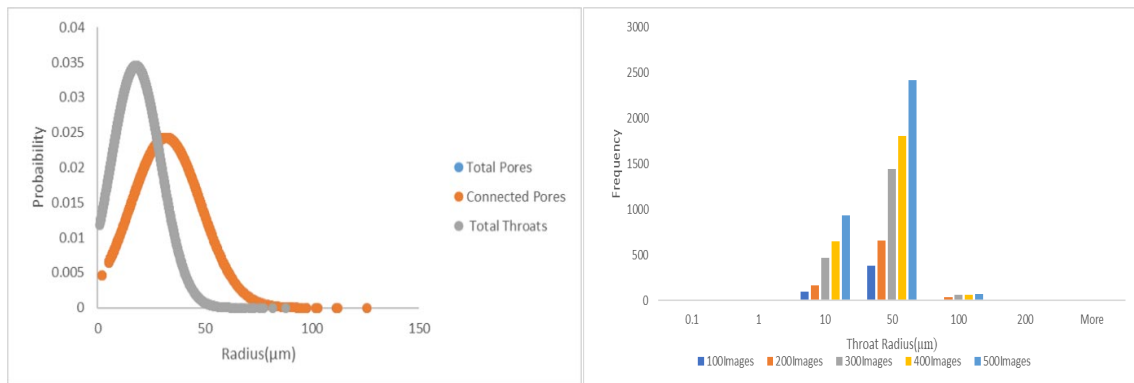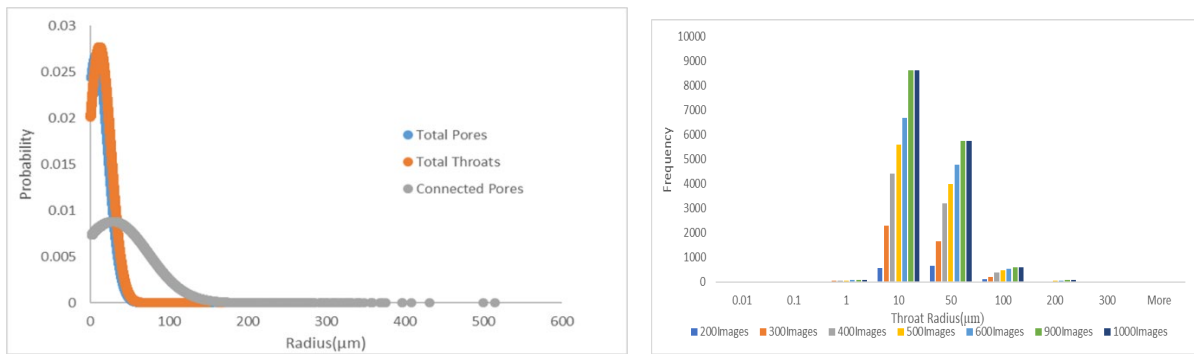

Figure 76 Throat Radius Distribution (b) Histogram of Throat Radius for a Ketton Limestone Sample
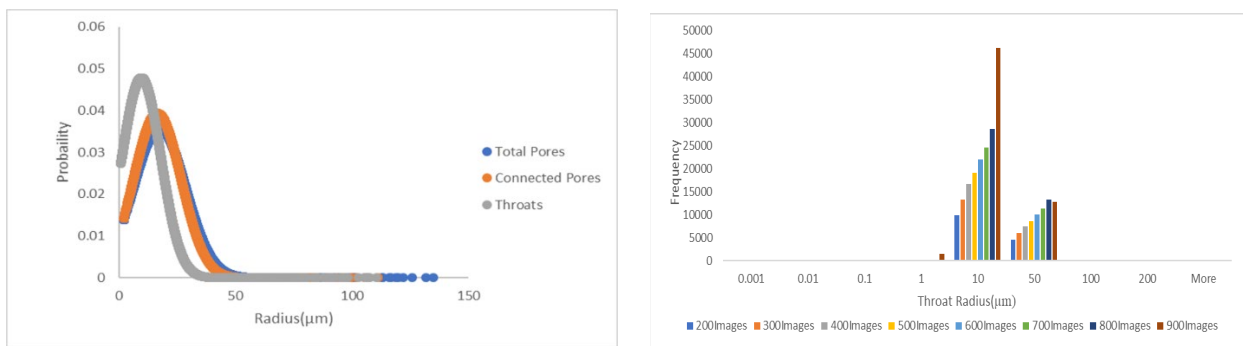

Figure 77 Throat Radius Distribution (b) Histogram of Throat Radius for an Estaillades Limestone Sample

4.4 Geometric Tortuosity

Tortuosity is a physical parameter that has a profound impact on the fluid flow through porous media. Carman (1937) first introduced the concept of tortuosity as the ratio between the actual length of the paths that fluid travels through the pore to the length of porous media. The geometric tortuosity is generally defined as the actual path length divided by the exact distance. Compared to hydraulic tortuosity, the geometrical tortuosity has a smaller value ($\tau g < \tau h$). The hydraulic tortuosity is calculated based on the flow path, which lies precisely along the streamline and practically has a smooth line. Meanwhile, geometric tortuosity is calculated on a pathway that takes the shortest possible path that crosses the streamlines (Ghanbarian et al., 2013, Amien et al., 2019). In this section, the geometric tortuosity of each sample considered in the thesis is measured by the Trace Correlation Lines module of Avizo®.

(a)   (b)

Figure 78 (a) Hydraulic Tortuosity and (b) Geometric Tortuosity (Amien et al., 2019)

4.4.1 Geometric Tortuosity for Shale Samples

The computed geometric tortuosity results of two shale samples are illustrated in Figure 80. The data in Figure 80 indicate that the geometric tortuosity of the Eagle Ford shale sample is about 3.5, whereas this value is around 1.8 for the Marcellus shale sample. The geometric tortuosity of Eagle Ford shale is almost 2-fold higher than that of the Marcellus shale sample. Also, for these two shale samples, the geometric tortuosity in X and Y direction are all zero. These phenomena may arise from the high complexity of pathways in the pore structure of shale. For all synthetic samples,

the more complex the pore structure is, the higher the tortuosity is (Amien et al., 2019). This explanation might directly account for why the geometric tortuosity of Eagle shale is higher than that of the Marcellus. Furthermore, there is no fluctuation in the geometric tortuosity curves shown in Figure 80. Hence, it indicates that the effect of sample size does not influence the geometric tortuosity of shale samples.
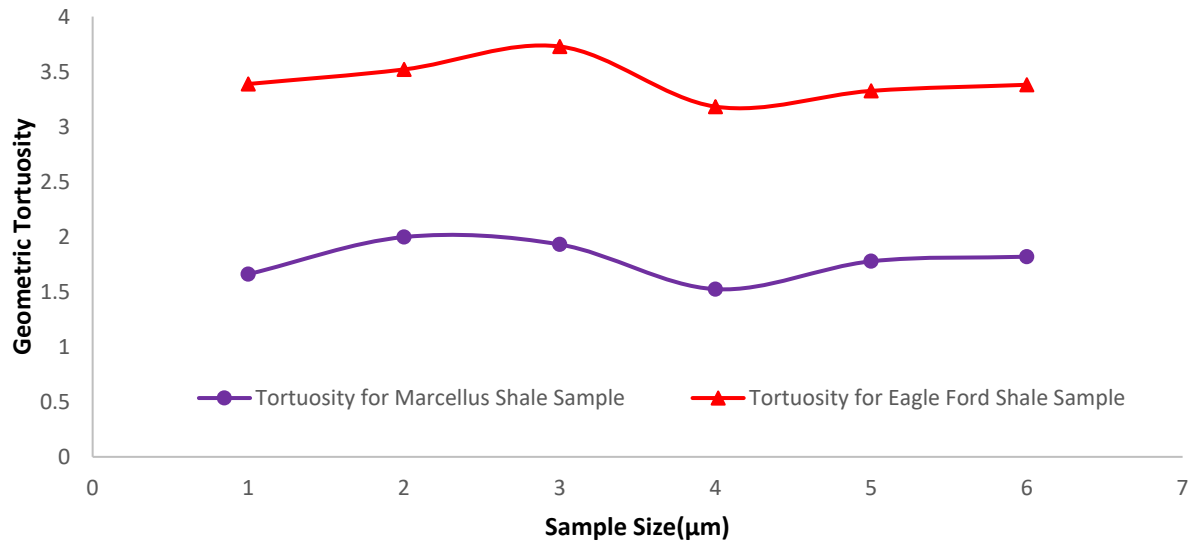

Figure 79 Geometric Tortuosity vs Sample Size for an Eagle Ford Shale Sample and a Marcellus Shale Sample

4.4.2 Geometric Tortuosity for Sandstone Samples

The following Figures (81 − 93) show the geometric tortuosity for the thirteen sandstone samples in this study. The geometric tortuosity of the sandstone samples is not like that of shale samples, which can be measured in three directions. The geometric tortuosity of the thirteen sandstone samples is basically around two, especially in the z-direction. What is unexpected is that, as shown in Figure 82, the geometric tortuosity of sandstone S2 reaches to 4 or 5 in both the x and y direction. Moreover, the trend of three lines of geometric tortuosity for each sandstone sample firstly increases then remains the same as the sample size increases. So, the REV of sandstone could be

reflected by the geometric tortuosity curves. The tortuosity vs sample size plots obtained for the shale samples are higher than those obtained for the sandstone samples. This phenomenon follows the principle of fluid flow: if the tortuosity is higher, the resistance to fluid transport through the porous medium would also be higher, since higher tortuosity leads to reduced permeability. The shale sample has higher tortuosity, because of the complex pore structure of shale, than sandstone, which would make the fluid flow more difficult in the shale.

Figure 80 Geometric Tortuosity vs Sample Size for Sandstone S1 Sample

Figure 81 Geometric Tortuosity vs Sample Size for Sandstone S2 Sample

Figure 82 Geometric Tortuosity vs Sample Size for Sandstone S3 Sample

Figure 83 Geometric Tortuosity vs Sample Size for Sandstone S4 Sample

Figure 84 Geometric Tortuosity vs Sample Size for Sandstone S5 Sample

Figure 85 Geometric Tortuosity vs Sample Size for Sandstone S6 Sample

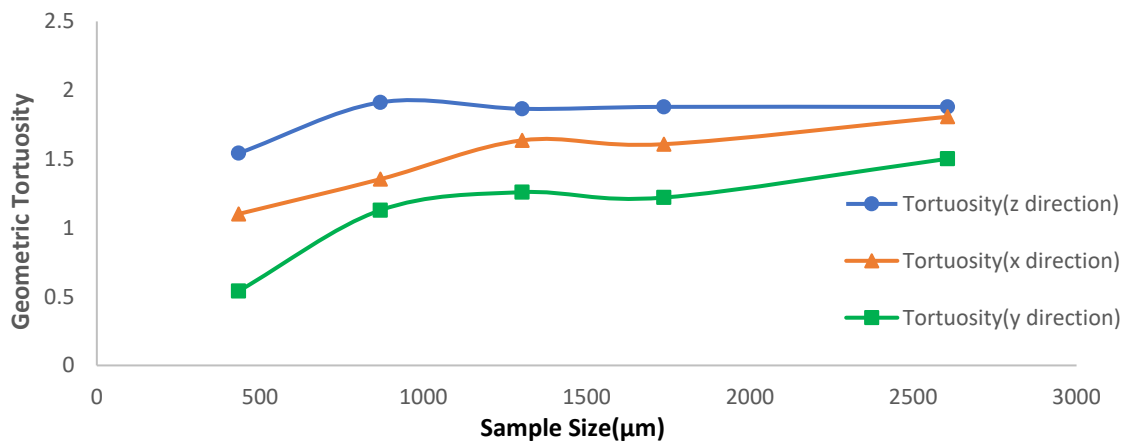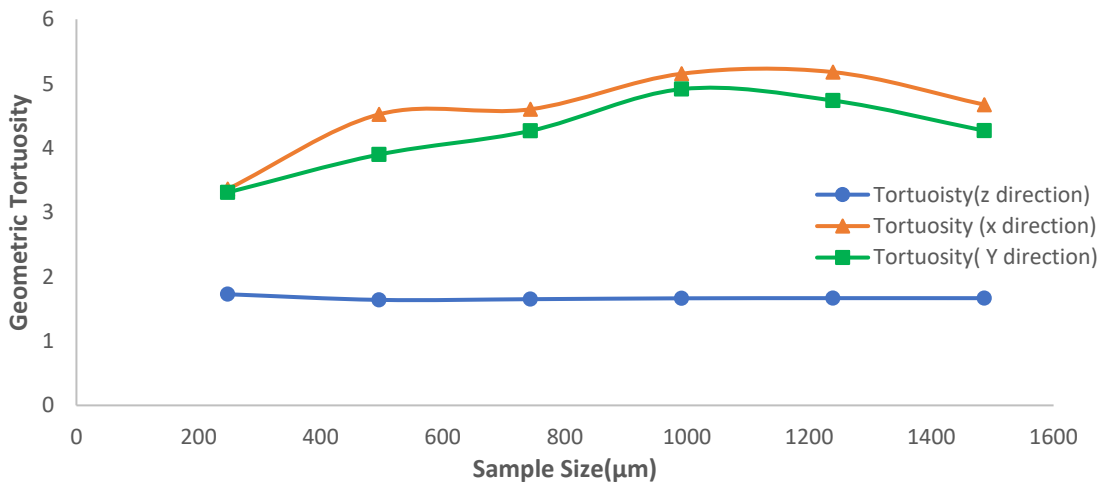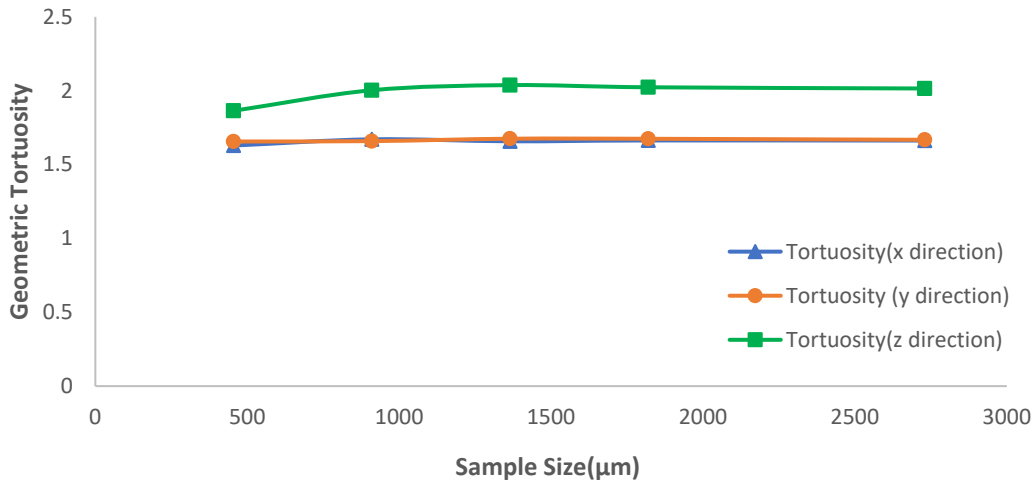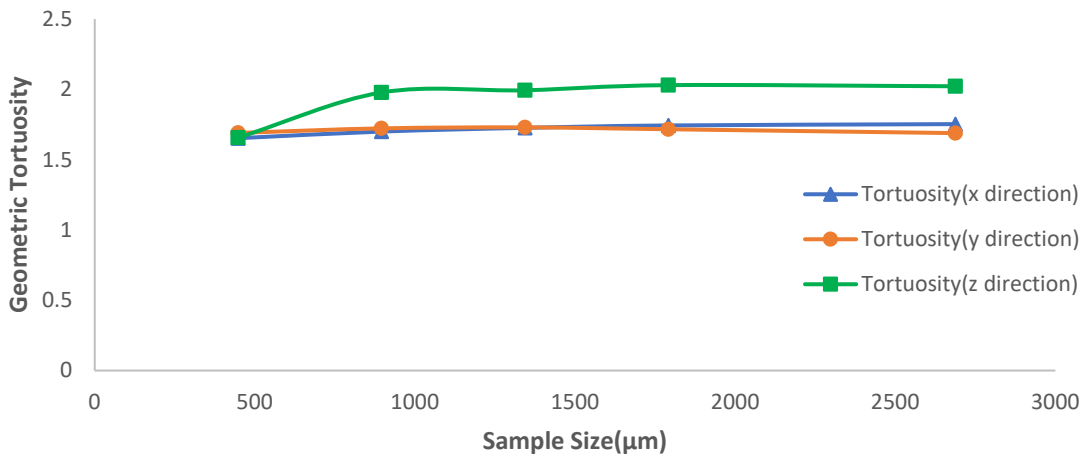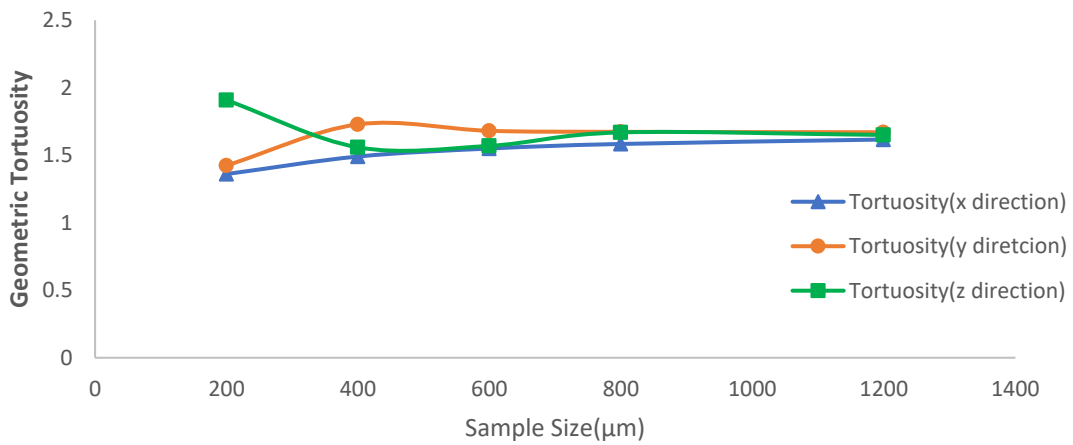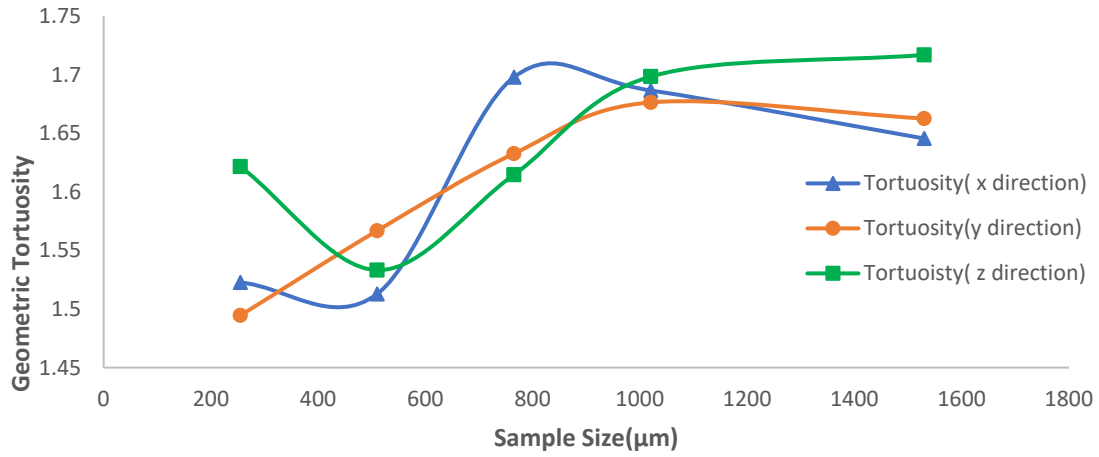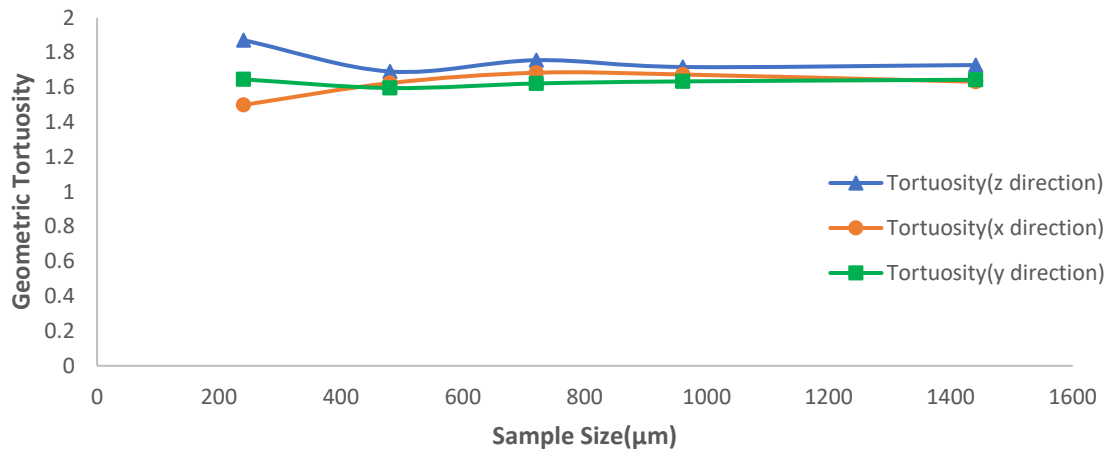**Figure 86 Geometric Tortuosity vs Sample Size for Sandstone S7 Sample**
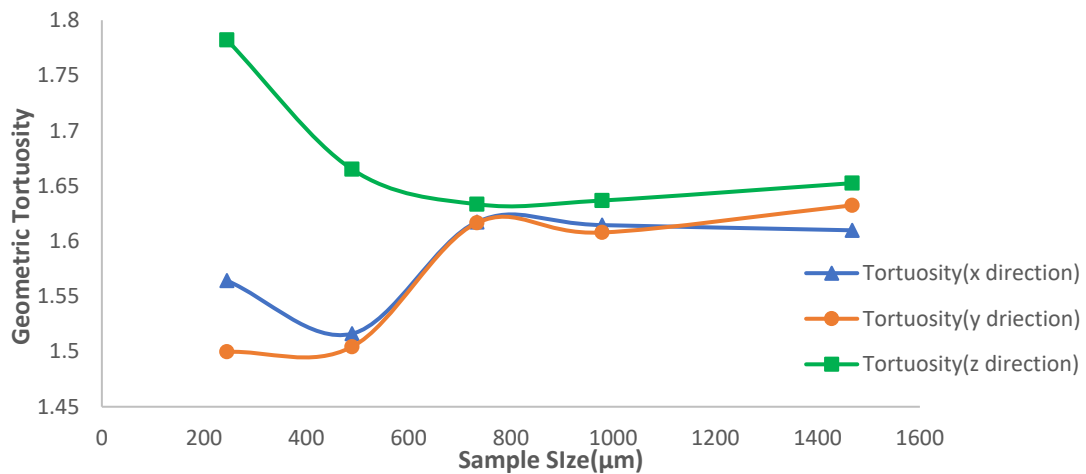
Figure 87 Geometric Tortuosity vs Sample Size for Sandstone S8 Sample
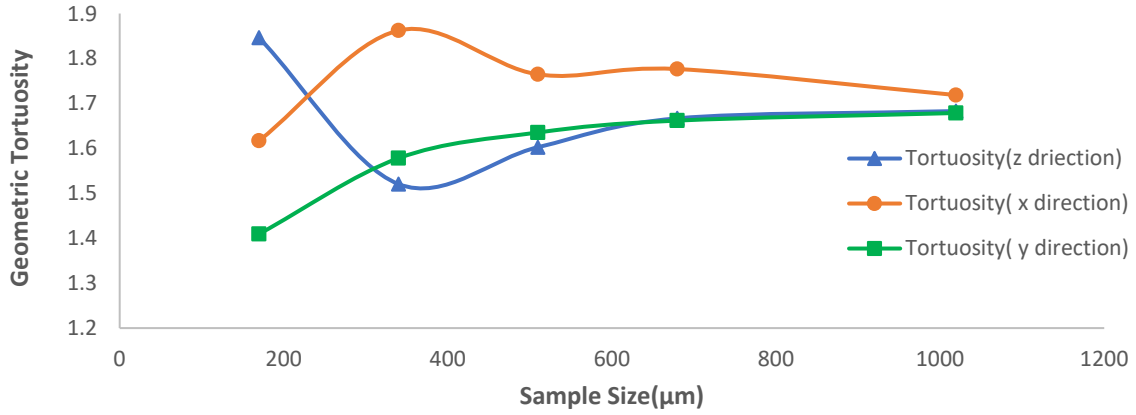
Figure 88 Geometric Tortuosity vs Sample Size for Sandstone S9 Sample
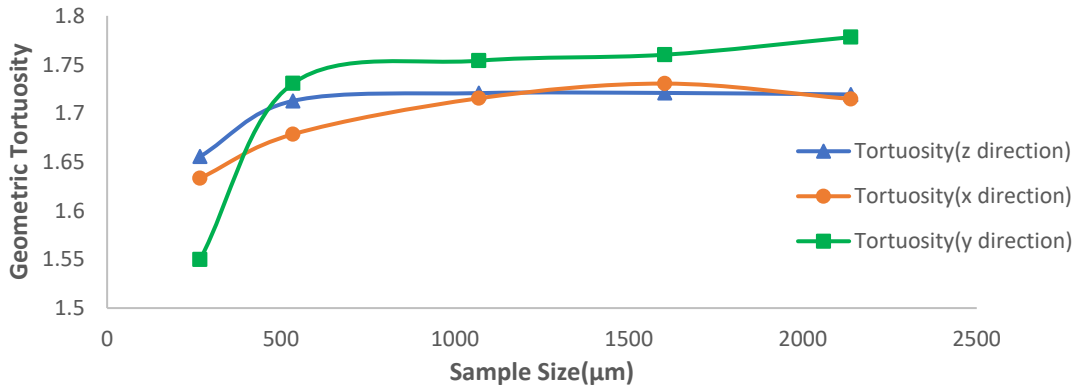
Figure 89 Geometric Tortuosity vs Sample Size for a Berea Sandstone Sample
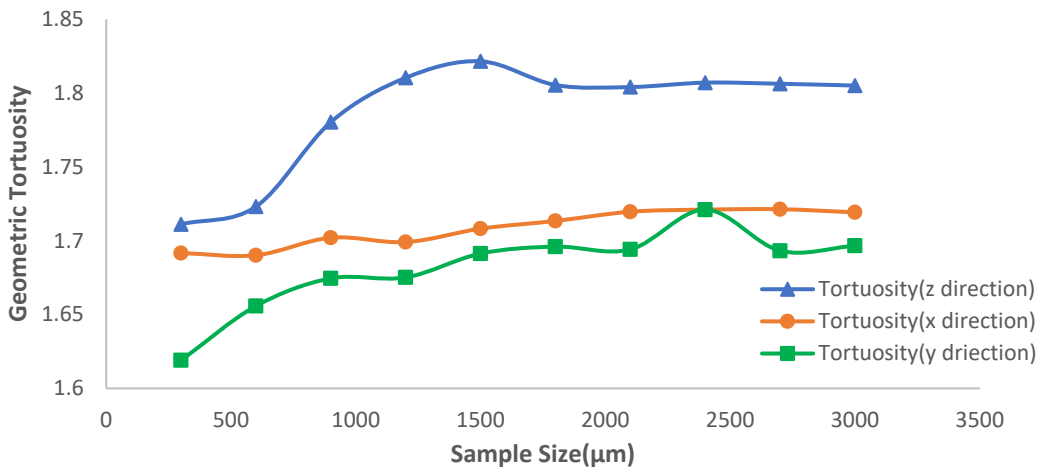
Figure 90 Geometric Tortuosity vs Sample Size for Bentheimer1 Sandstone Sample
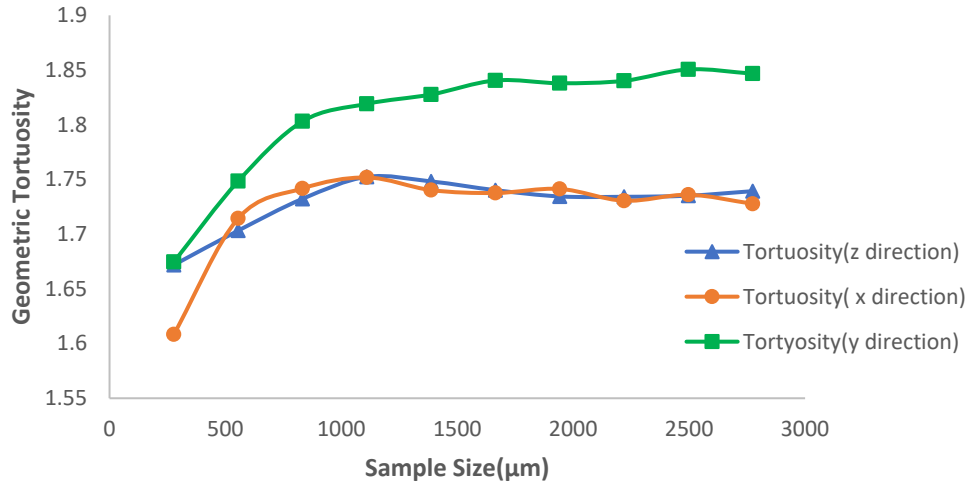
Figure 91 Geometric Tortuosity vs Sample Size for a Doddington Sandstone Sample
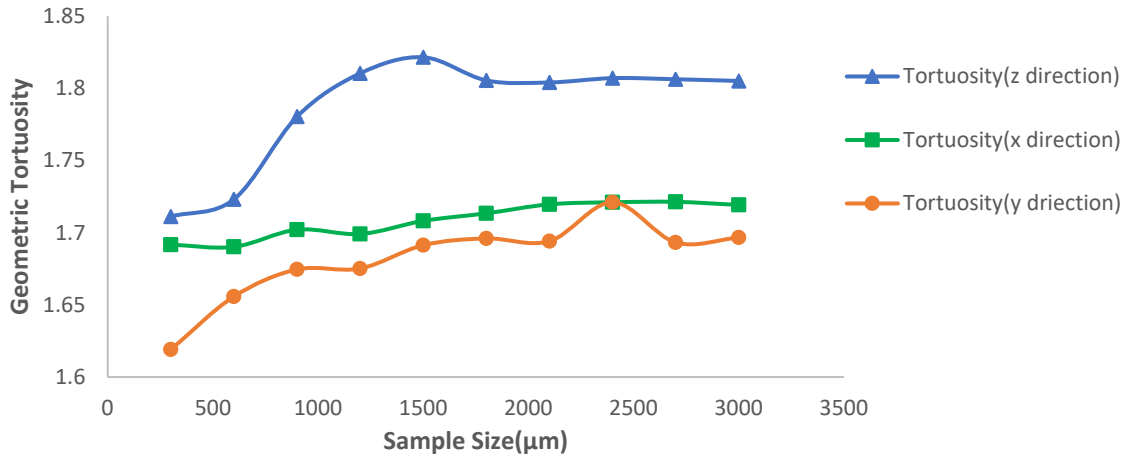
Figure 92 Geometric Tortuosity vs Sample Size for Bentheimer 2 Sandstone Sample

4.4.3 Geometric Tortuosity for Carbonate Samples

The geometric tortuosity of carbonate samples is shown in below Figures(94 − 98). As shown in the statistics, the geometric tortuosity of carbonate remains steady as the sample size increases. The geometric tortuosity of these carbonate samples lies in the range of 1.5 to 2, which is smaller than that of the sandstone samples. These curves of carbonate are incredibly flat, with an average slope of 1:2500.
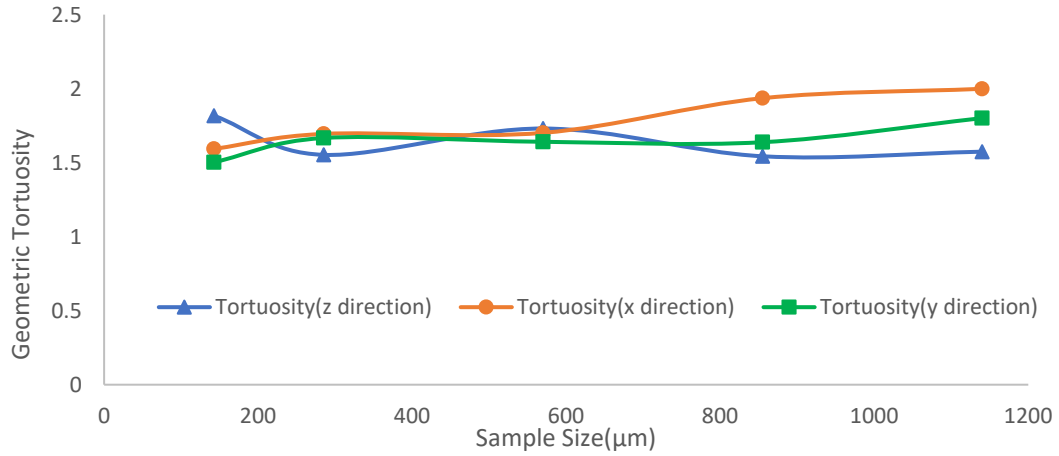
Figure 93 Geometric Tortuosity vs Sample Size for Carbonate C1 Sample
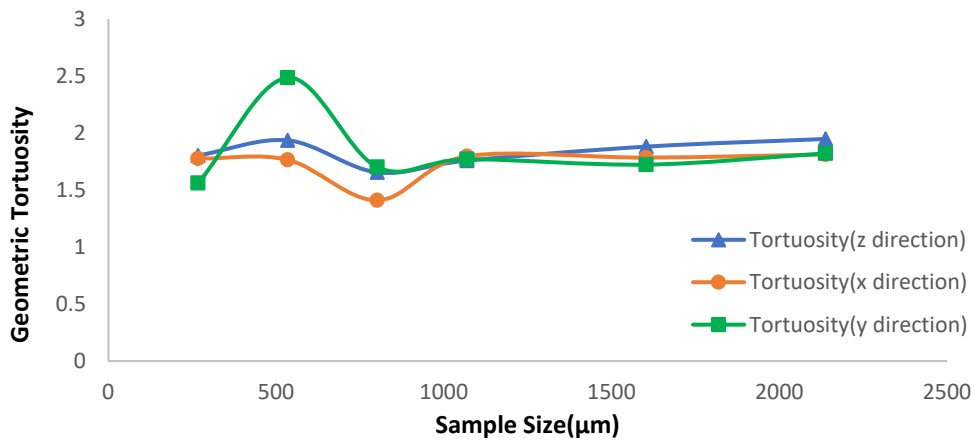
Figure 94 Geometric Tortuosity vs Sample Size for Carbonate C2 Sample

Figure 95 Geometric Tortuosity vs Sample Size for Ketton Carbonate Sample

Figure 96 Geometric Tortuosity vs Sample Size for Estaillades 1 Carbonate Sample

Figure 97 Geometric Tortuosity vs Sample Size for Estaillades 2 Carbonate Sample

4.4.4 Geometric Tortuosity for Limestone Samples

The two below Figures (99 − 100) separately depict the geometric tortuosity as a function of sample size for Estaillades limestone and Ketton limestone samples. Figure 99 shows that the geometric tortuosity of Estaillades limestone remains steady with increasing sample size, between 1.5 and 2, in all three measured directions. The three geometric tortuosity curves corroborate the finding (above 4.1.5) that the REV of Estaillades is around 1mm. While the geometric tortuosity of Estaillades limestone is not affected by sample size, the geometric tortuosity of Ketton limestone

along three pathways fluctuates significantly as sample size increases. Moreover, the geometric tortuosity along x and y directions form an inverted "v" shape. Since the limestone sample is limited in this study, it is unwise to draw conclusions regarding on geometric tortuosity and sample size for limestone.

Figure 98 Geometric Tortuosity vs Sample Size for a Ketton Limestone Sample

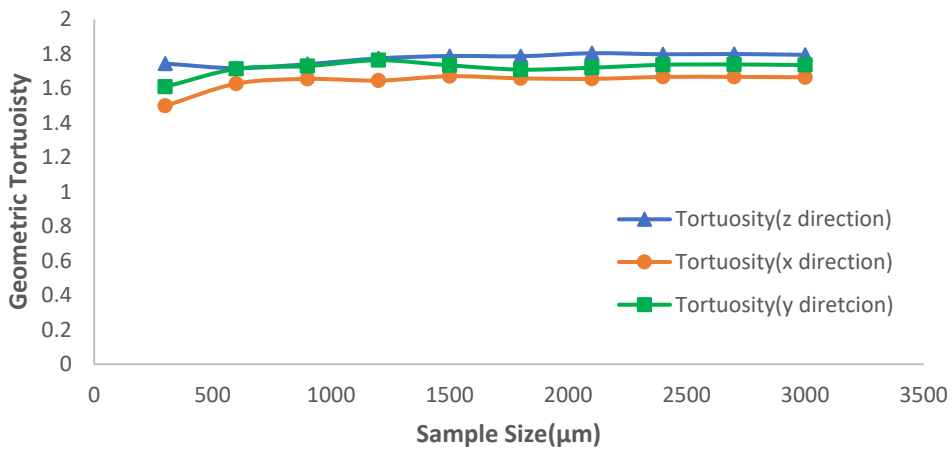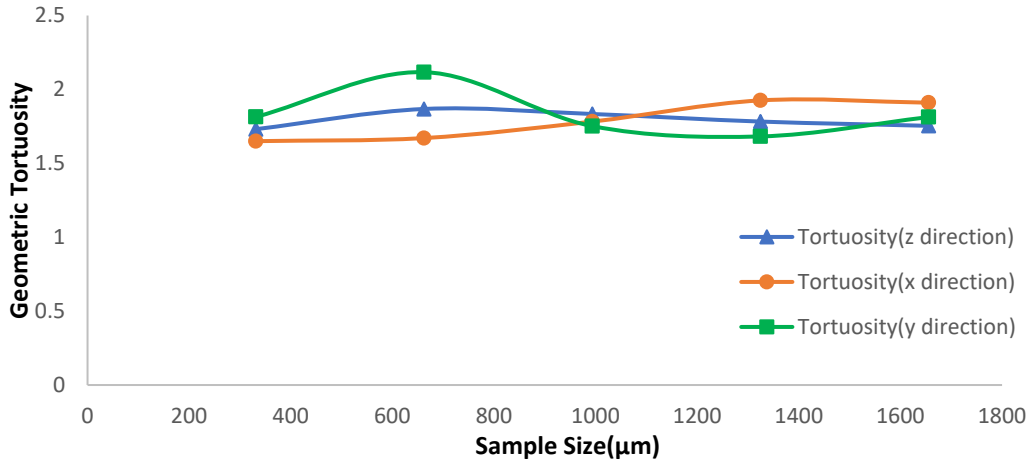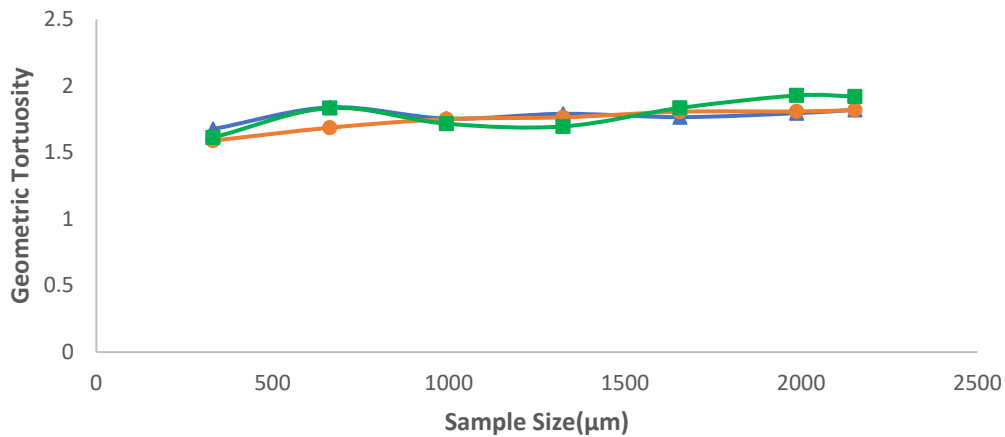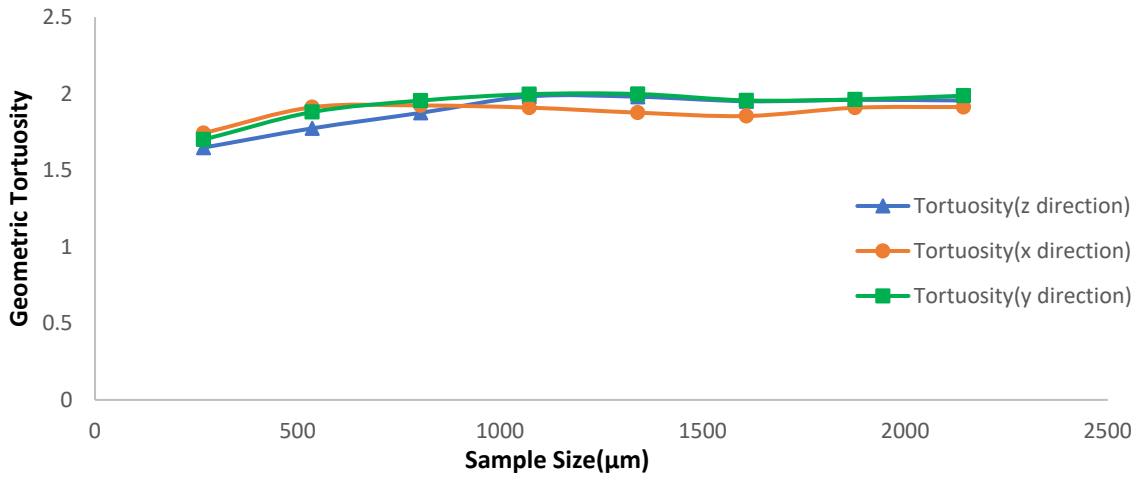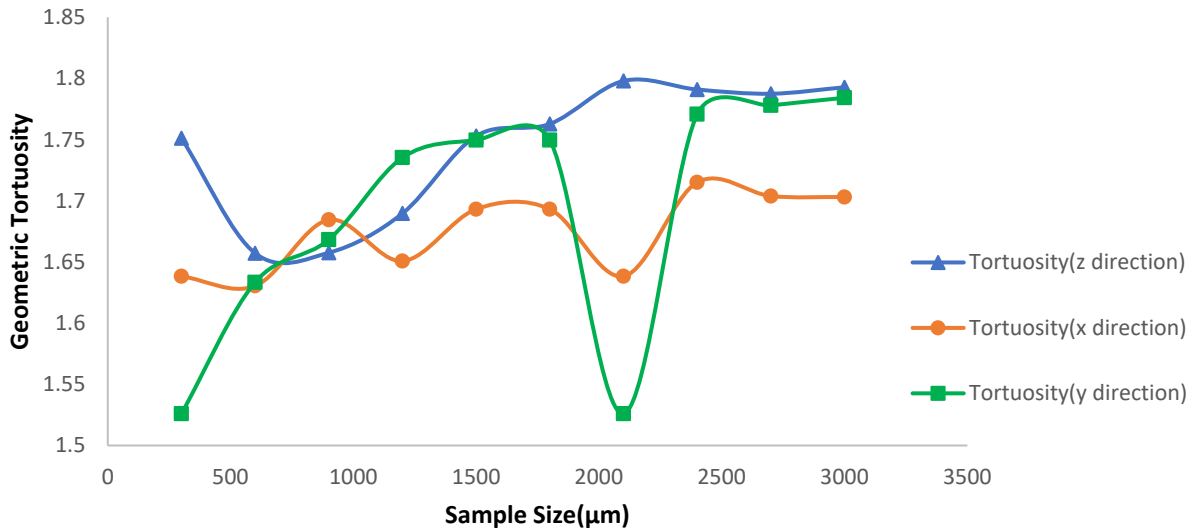**Figure 99 Geometric Tortuosity vs Sample Size for Estaillades Limestone Sample**

4.4.5 Geometric Tortuosity REV

For all 22 samples in the study, the value of geometric tortuosity is almost no more than two, except for the Eagle Ford shale sample. Additionally, the curves of different samples universally increase or decrease upon initial sample size increases, but then at larger sample sizes, the geometric tortuosity levels off. For the two shale samples, their REV appears to be higher than 5µm, judging by the geometric tortuosity curves. Because the number of image slices is limited, it is difficult to determine the specific REV for the shale samples in this study. Among the 13 sandstone samples, except for S2 and S6, the REV is determined: the REV of S1, S4, and Doddington sandstone samples are between 1mm and 1.5mm; the REV of S3, S5, S7, S9, and Berea sandstone samples are close to 0.5mm; the REV of S8 is around 0.7mm. For the carbonate samples, the REV of carbonate C1 and Ketton carbonate samples are approximately 0.3mm; the REV of carbonate C2 and Estaillades 2 is close to 1mm. For the limestone samples, only Estaillades limestone REV can be observed, and is around 0.5mm. The geometric tortuosity is a good predictor for determining REV, but the REV of geometric tortuosity distribution is smaller than that of porosity distribution.

Furthermore, the geometric tortuosity of sandstone, carbonate, and limestone samples are anisotropic. This feature might result not only from the complexity of pore structure but also from the bedding effect. The bedding effect can cause the geometric tortuosity in the direction perpendicular to the bedding planes to have a larger value than the tortuosity in the direction parallel to the bedding (Peng et al., 2015).

4.5. Totruosity Factor

There is an open-source MATLAB code (Taufactor®) that has been used to measure the tortuosity factor for the samples in this dissertation. Taufactor calculates the directional tortuosity

factor (τ) along three mutually perpendicular axes of interconnected "diffusive phases" (or porous phases) through a three-dimensional volume. In theory, the tortuosity factor quantifies the geometric interconnectivity of pore space, taking into account the changing cross-sectional area of pores (Backeberg et al., 2017). Backeberg also pointed out that in a homogenous system, the tortuosity factor value tends towards a maximum value with an increasing length unit of the test axis. If there are no interconnected pathways across the tested volume, the computation fails, and TauFactor returns a value of infinity. Due to the heterogeneity of mineral distributions in natural shales, the tortuosity factor will vary from sample to sample. Additionally, the resolution and image memory of each sample influence the result of the tortuosity factor calculation. Because there are some samples with 1024*1024* 1024 pixels or 650*650*650 pixels micro-CT images in this disseration, these samples cannot be used in the Taufactor code. Thus, in this section, only shale, sandstone, and several carbonates are compared.

4.5.1 Tortuosity Factor for Shale Samples

The data presented in Figure 101 and Figure 102 show that the tortuosity factor of the Eagle Ford shale sample is around 600 at 6μm, and the tortuosity factor of Marcellus is about 400 when the sample size is 2μm. For the Marcellus shale sample, due to the problem of image memory, it cannot be run if the number of images is over 300. Moreover, getting a larger tortuosity factor result fits the conclusion of Berkeberg that the tortuosity factor would increase, even to infinity, for a sample with low pore connectivity. This phenomenon reflects that shale has inferior connectivity. The effect of sample size can also influence the tortuosity factor.
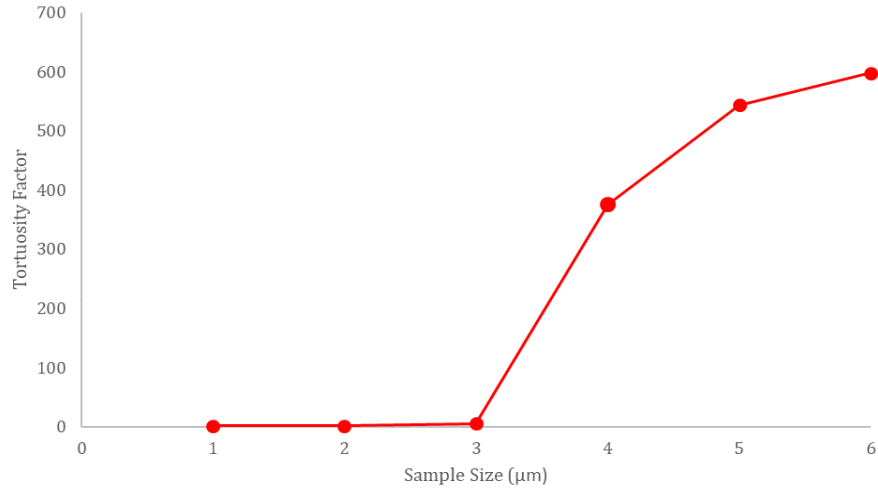
Figure 100 Tortuosity Factor vs Sample Size for an Eagle Ford Shale Sample
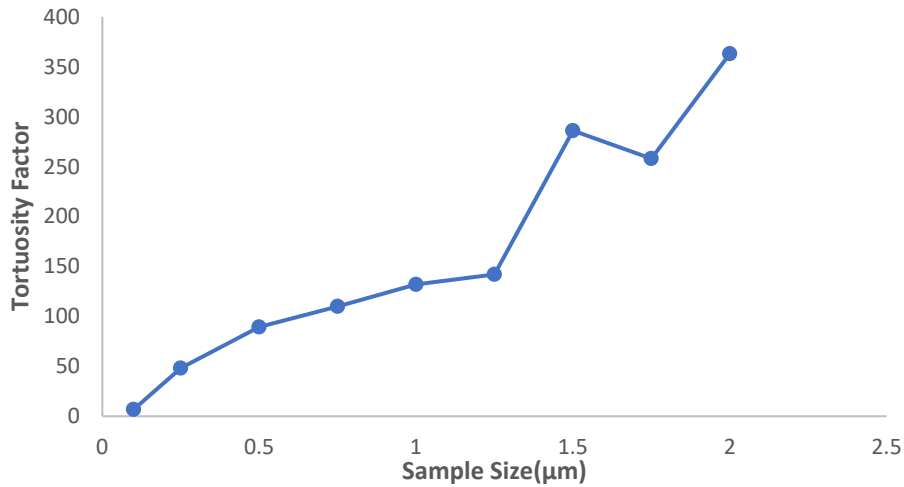
Figure 101 Tortuosity Factor vs Sample Size for a Marcellus Shale Sample

4.5.2 Tortuosity Factor for Sandstone Samples

As can be seen in Figures $103 - 107$, the tortuosity factor of sandstone samples S1− S9 and Berea sandstone are shown as a function of sample size. It is apparent from these figures that the tortuosity factor of each sandstone sample rises as the sample size increases. The tortuosity is mainly bound between 3 and 4. Only sandstone S1, S3, and S4 have higher tortuosity factors, with the tortuosity factor of S4 reaching to 20 with a sample size of 3mm. Moreover, interestingly, these samples all have lower porosity. Therefore, the results for sandstone suggest a link between the

tortuosity factor and porosity. If the sample has a higher tortuosity factor, its total porosity should be smaller.

Figure 102 (a) Tortuosity Factor vs Sample Size for Sandstone S1 Sample (b) Tortuosity Factor vs Sample Size for Sandstone S2 Sample
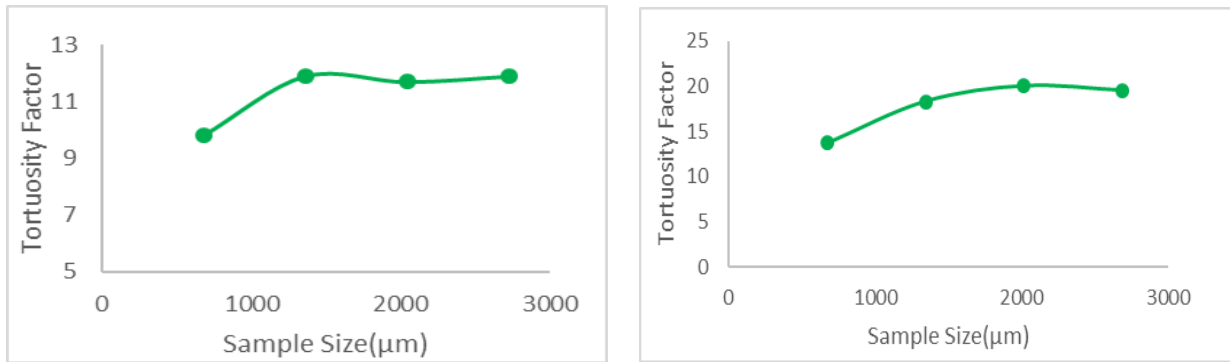
Figure 103 (a) Tortuosity Factor vs Sample Size for Sandstone S3 Sample (b) Tortuosity Factor vs Sample Size for Sandstone S4 Sample
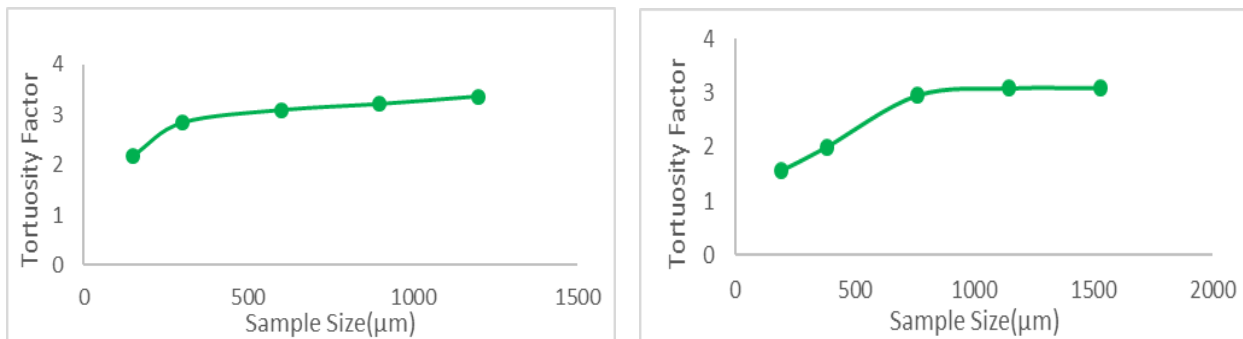
Figure 104 (a) Tortuosity Factor vs Sample Size for Sandstone S5 Sample (b) Tortuosity Factor vs Sample Size for Sandstone S6 Sample
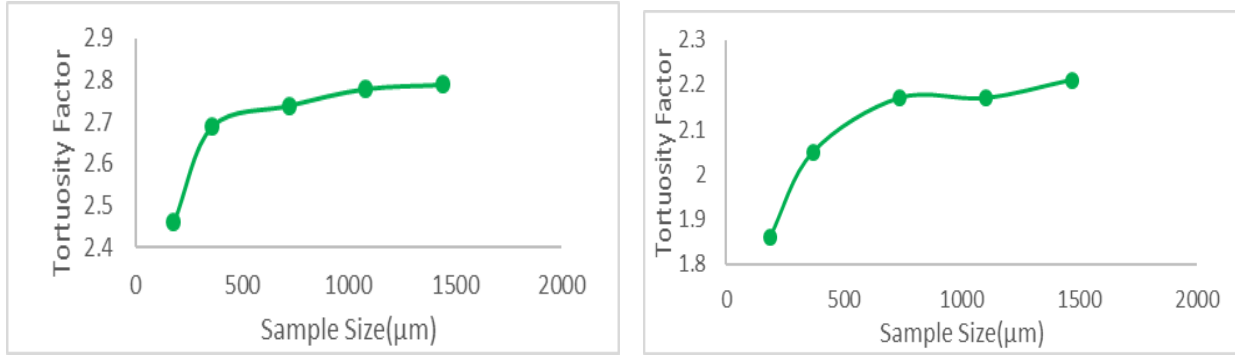
Figure 105 (a) Tortuosity Factor vs Sample Size for Sandstone S7 Sample (b) Tortuosity Factor vs Sample Size for Sandstone S8 Sample
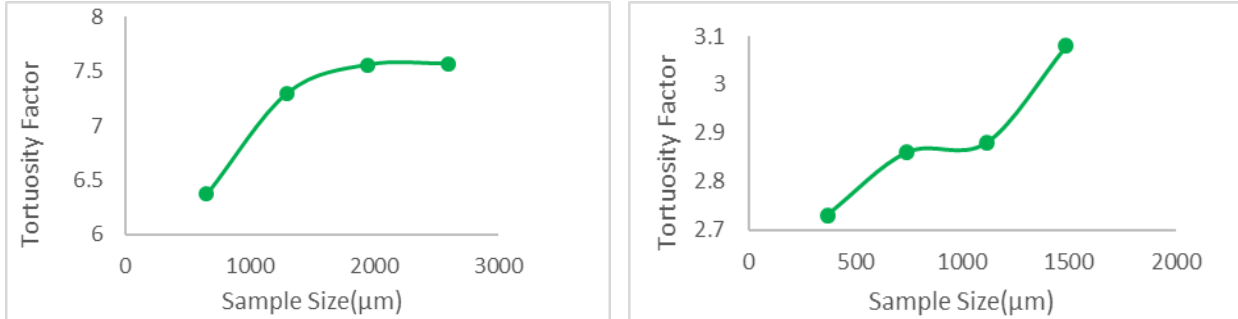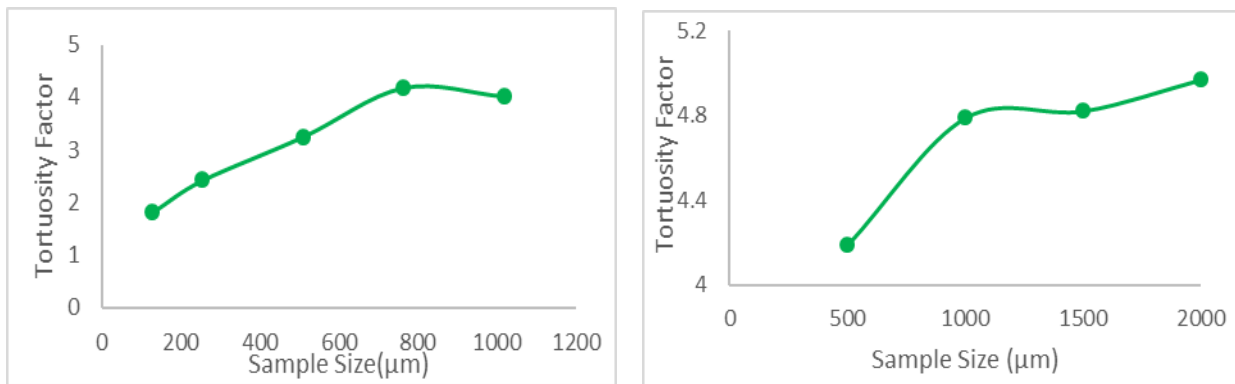

Figure 106 (a) Tortuosity Factor vs Sample Size for Sandstone S9 Sample (b) Tortuosity Factor vs Sample Size for a Berea Sandstone Sample

4.5.3 Tortuosity Factor for Carbonate Samples

Figures 108 (a) and (b) illustrate the tortuosity factor of carbonate C1 and C2 samples, in spite of the fact that there are only two carbonate samples compared. Both carbonate C1 and C2 fit the supposition that a sample with higher porosity would present a lower tortuosity factor. The porosity of carbonate C1 is 23.3%, and its tortuosity factor is around 7. The tortuosity factor of carbonate C2 almost reaches to 50, and its porosity is just 16.8%.
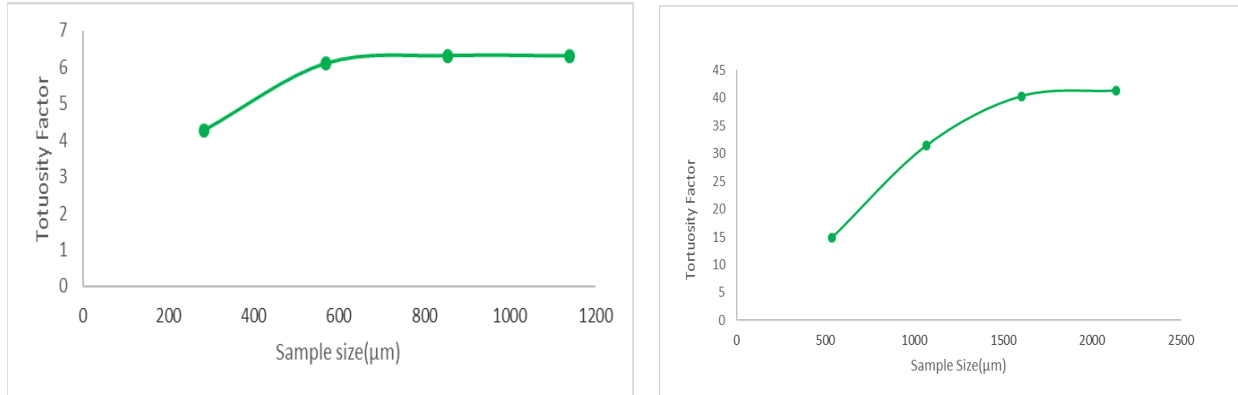
Figure 107 (a) Tortuosity Factor vs Sample Size for Carbonate C1 Sample, (b) Tortuosity Factor vs Sample Size for Carbonate C2 Sample

Based on these tortuosity factor results of the three types of rocks, we find that, except for the tortuosity factor of the shale reaching hundreds of degrees, the tortuosity factor of carbonate and sandstone samples are almost similar. According to these results, it clearly indicates that the pore connectivity of shale is worse than those of carbonate and sandstone. Furthermore, Lee and Kozak (1986) proposed that for either of these constrained geometries, the tortuosity factor is a monotonically decreasing function of porosity. This conclusion also directly reflects that shale's large tortuosity corresponds to its small porosity. The results for sandstone and carbonate samples are all precisely in line with this conclusion.

Chapter5 Pore Connectivity

5.1 Average Coordination Number

  The coordination number refers to the number of throats connect to the pores. The coordination number is the best predictor to reflect pore connectivity. In this thesis, each sample's pore network model is extracted using the image processing software Avizo®. Avizo® and Avizo® XPNM Extension allow for access to different statistics from a labeled and separated pore space. According to the pore network model, the coordination number appears.

5.1.1 Average Coordination Number for Shale Samples

Figure 109 − Figure 110 provide the coordination number distribution for Eagle Ford shale and Marcellus shale samples. For the Eagle Ford shale sample, its average coordination number ranges from 2.8 to 3.3, with increasing sample size. The upper coordination number of Eagle Ford is more than 20. Approximately 30% of pores have a coordination number of 0 (isolated pores) and 1 (dead ends). For the Marcellus shale sample, the average coordination number is between 4 and 5, which remains nearly constant as the sample size increases. The upper bound of coordination number in the Marcellus shale sample is higher than 25, and more than 20% of pores are isolated pores or dead-end pores. Though coordination number isn't a direct predictor of permeability, the presence of isolated and dead-end pores might account for ultra-low permeability for these two shale samples. By comparing Marcellus shale and Eagle Ford shale samples, the average coordination number of Eagle Ford is lower than that of the Marcellus shale. However, there are more pores with a coordination number of 0 in the Marcellus shale sample than in the Eagle Ford shale sample.
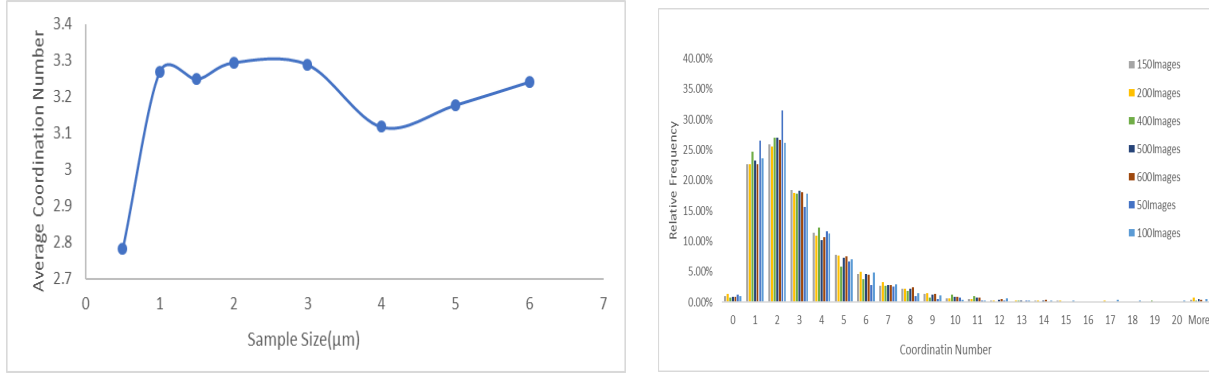
Figure 108 (a) Average Coordination with Sample Size(µm) (b) Histogram of Coordination Number for an Eagle Ford Shale Sample

Figure 109 (a) Average Coordination with Sample Size(µm) (b) Histogram of Coordination Number for a Marcellus Shale Sample

5.1.2 Average Coordination Number for Sandstone Samples

The following Figures $(111-120)$ provide the coordination number distribution of ten sandstone samples. What stands out in these graphs is that there are no isolated pores in the sandstone sample, and a dead-end pore concentration of only $10\%-25\%$ in these sandstone samples. Their average coordination number lies almost completely in the range of $2.92-2.99$, $3-5$ and $6-7$, with the upper bound of coordination number for sandstone sample S2 around 20. The largest coordination number of the other sandstone samples can generally reach 11 or 15. Additionally, the coordination number for half of the pores for these sandstone samples lie in the interval 1 to 4, and the

coordination number of these sandstone samples mostly is in the range of $2 - 6$. In contrast to the above shale samples, the sandstone samples have ostensibly better connectivity.

Figure 110 (a) Average Coordination with Sample Size(μm) (b) Histogram of Coordination Number for Sandstone Sample S1

Figure 111 (a) Average Coordination with Sample Size(μm) (b) Histogram of Coordination Number for Sandstone Sample S2
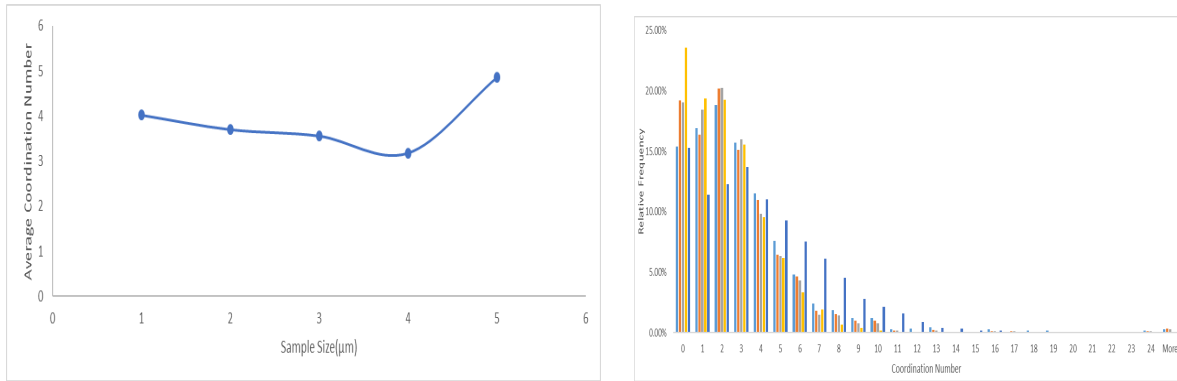

Figure 112 (a) Average Coordination with Sample Size(μm) (b) Histogram of Coordination Number for Sandstone Sample S3

Figure 113 (a) Average Coordination with Sample Size(μm) (b) Histogram of Coordination Number for Sandstone Sample S4

Figure 114 (a) Average Coordination with Sample Size(μm) (b) Histogram of Coordination Number for Sandstone Sample S5

Figure 115 (a) Average Coordination with Sample Size(μm) (b) Histogram of Coordination Number for Sandstone Sample S6

Figure 116 (a) Average Coordination with Sample Size(μm) (b) Histogram of Coordination Number for Sandstone Sample S7
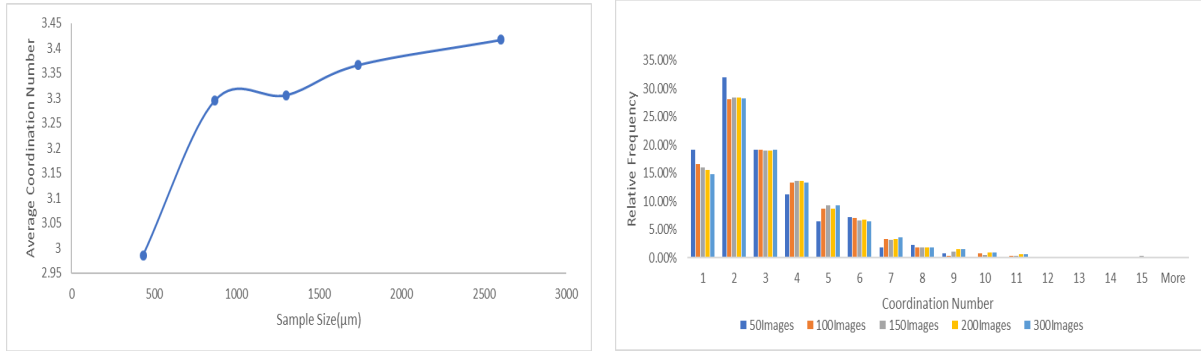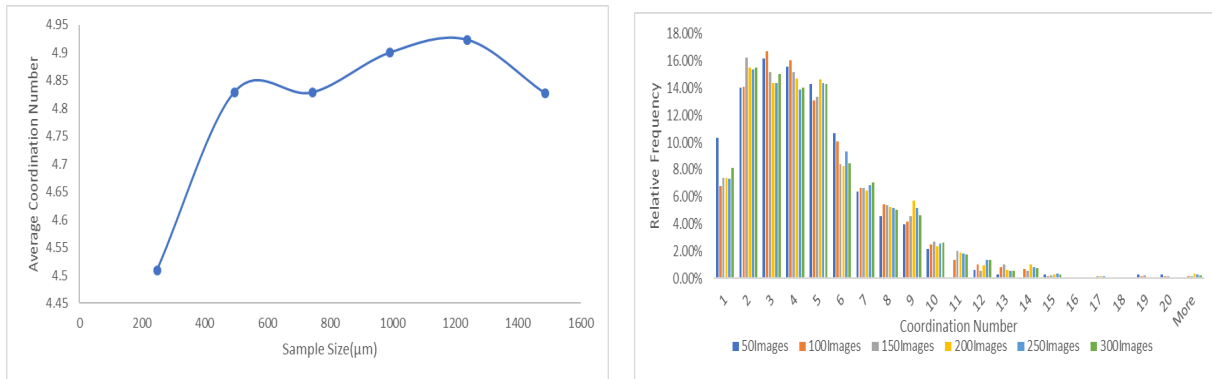

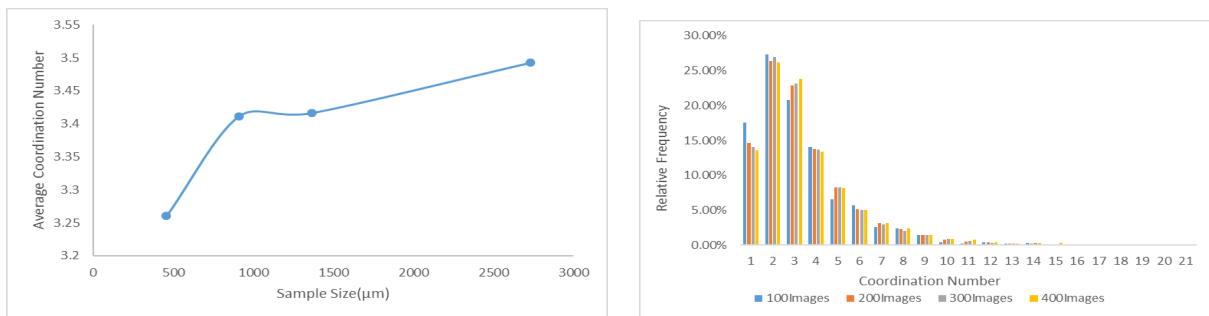**Figure 117 (a) Average Coordination with Sample Size(μm) (b) Histogram of Coordination Number for Sandstone Sample S8**
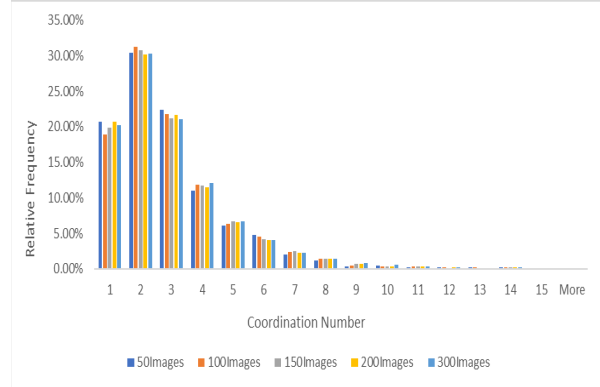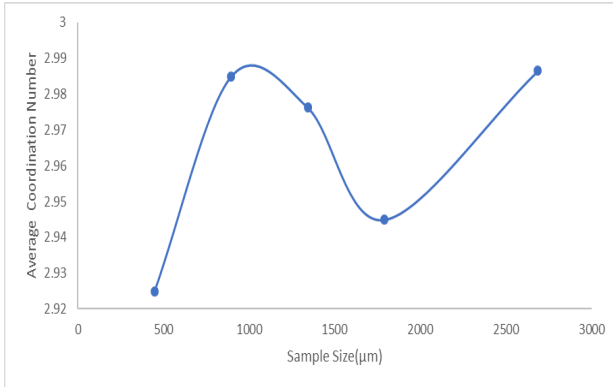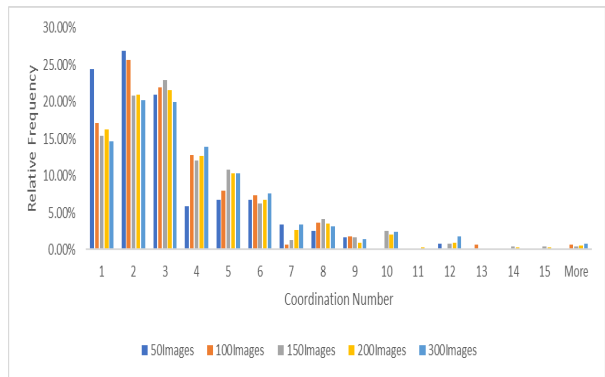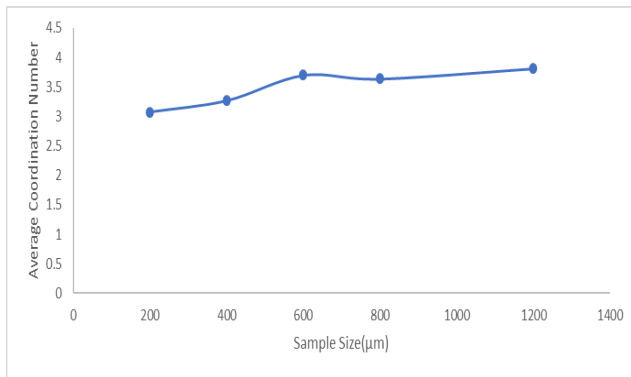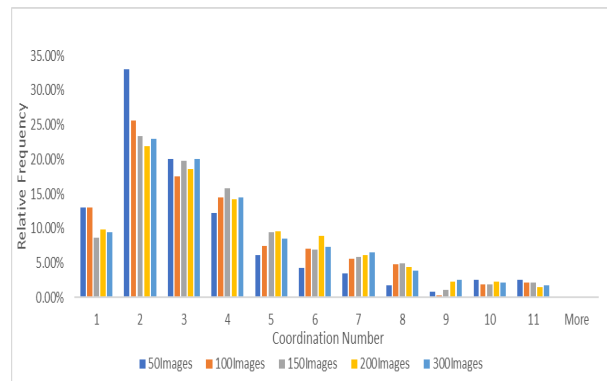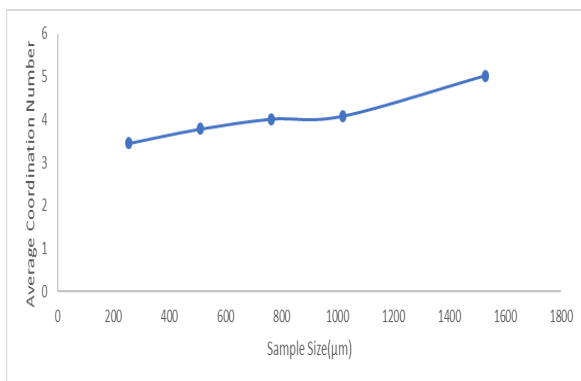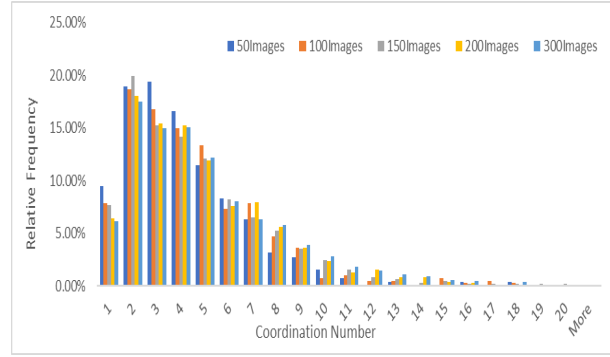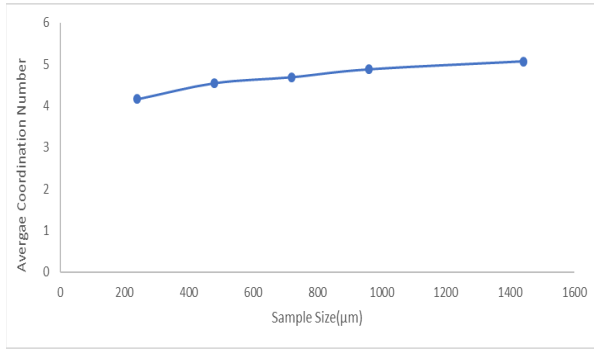

Figure 118 (a) Average Coordination with Sample Size(μm) (b) Histogram of Coordination Number for Sandstone Sample S9

Figure 119 (a) Average Coordination with Sample Size(μm) (b) Histogram of Coordination Number for a Doddington sandstone Sample

5.1.3 Average Coordination Number for Carbonate Samples

 Figure 121 − Figure 125 display the coordination number distribution of the five carbonate samples. Like the average coordination number of shale and sandstone, the average coordination number of carbonates increases with the sample size. The average coordination number of C1 increases from 3.8 to 4.5 as the sample size expands from 0.5mm to 2.5mm. The average coordination number of C2 rises from 3.6 to 4.3 as the sample size increases from 0.2mm to 2.2mm. For the Ketton carbonate sample, the average coordination number goes up from 3.3 to 3.7 but remains constant when the sample size reaches 2mm. Lastly, for the two Estaillades carbonate samples, Estaillades 1 shows a slight tendency to increase and then decrease. Its average coordination number ranges from 3.3 to 3.7, the same as the Ketton carbonate sample. The average coordination number of carbonate samples is approximately 4, and there are few isolated and dead-end pores in the samples. The peak value of coordination distribution for carbonate C1 is higher than 20, and for most of the carbonate samples, the coordination number for more than 50% of pores lies in the interval of 2 to 5.

Figure 120 (a) Average Coordination with Sample Size(μm) (b) Histogram of Coordination Number for Carbonate Sample C1

Figure 121 (a) Average Coordination with Sample Size(μm) (b) Histogram of Coordination Number for Carbonate Sample C2

Figure 122 (a) Average Coordination with Sample Size(μm) (b) Histogram of Coordination Number for a Ketton Carbonate Sample
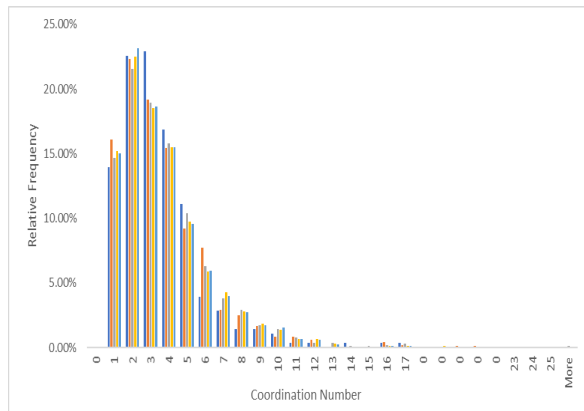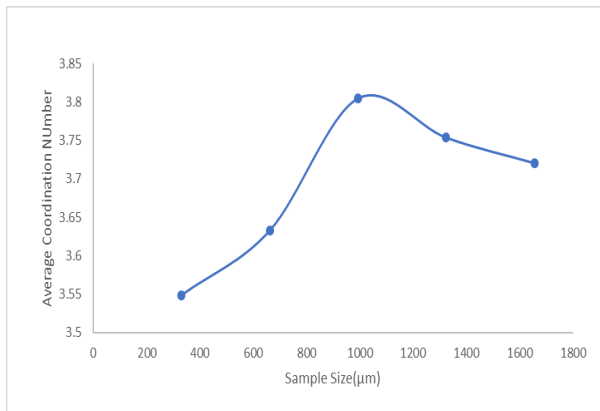
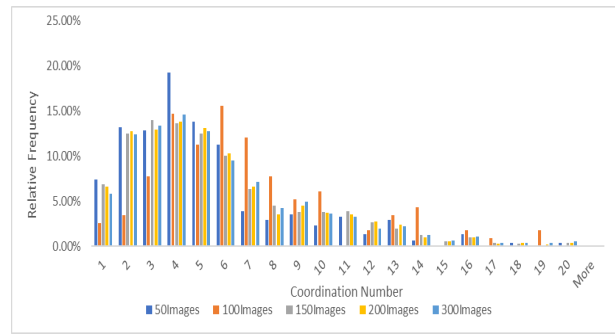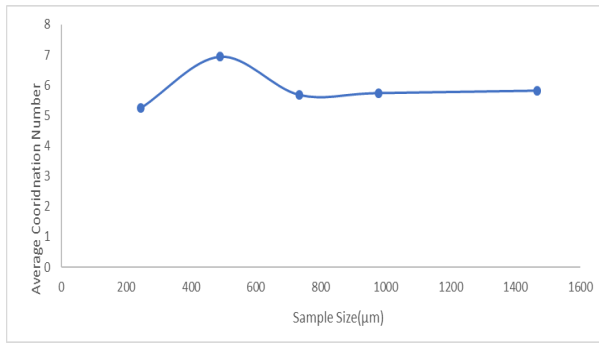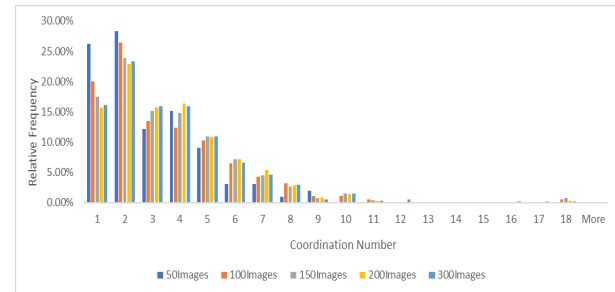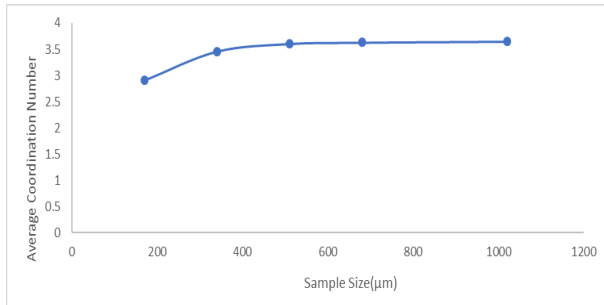**Figure 123 (a) Average Coordination with Sample Size(μm) (b) Histogram of Coordination Number for Estaillades 1 Carbonate Sample**
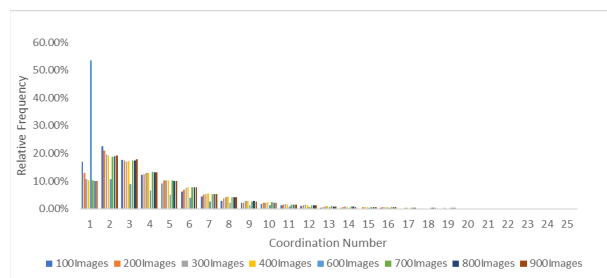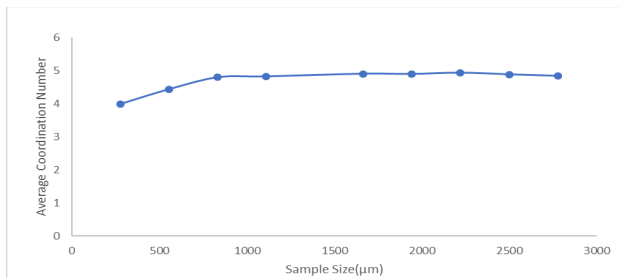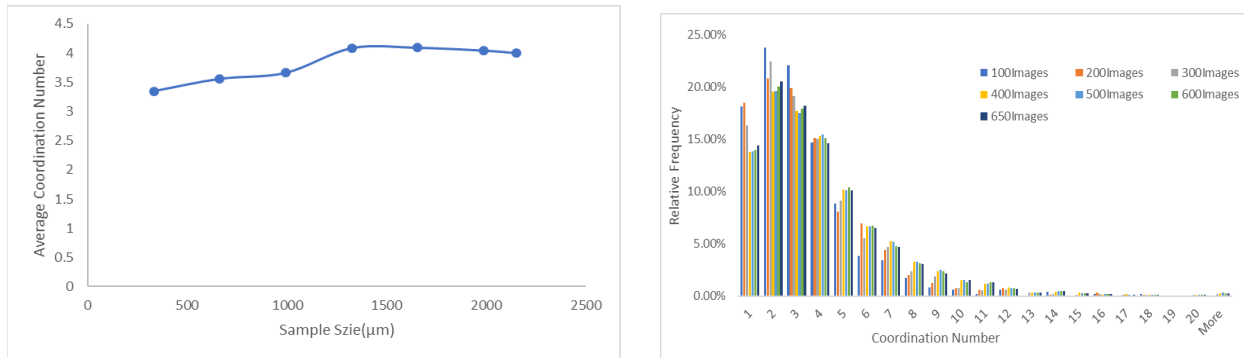
Figure 124 (a) Average Coordination with Sample Size(µm) (b) Histogram of Coordination Number for Estaillades 2 Carbonate Sample

5.1.4 Average Coordination Number for Limestone Samples

  The below Figure 126 and Figure 127 describe the coordination number results of two limestone samples. Figure 126 shows the average coordination number of the Estaillades limestone sample as a function of sample size, with the average coordination number fluctuating between 4.1 and 4.2 with sample size increasing from 500µm to 2500µm. And from the coordination number histogram of Estaillades limestone, the coordination number ranges from 0 to 20, and there are 10% of pores with a coordination number of 0 or 1. Figure 127 displays the curve of the average coordination number of Ketton limestone as the sample size increases. The average coordination number of Ketton limestone pores varies from 4 to 5, its largest coordination number can be more than 30. But there are about 15% of pores with a coordination number of 0 or 1. Although the distribution range for coordination number is broader for Ketton than for Estaillades, there are more isolated and dead-end pores in the Ketton limestone sample. An interesting finding of the carbonate, shale, and limestone samples is that the larger the coordination number the sample can reach, the more isolated pores exist in the sample.
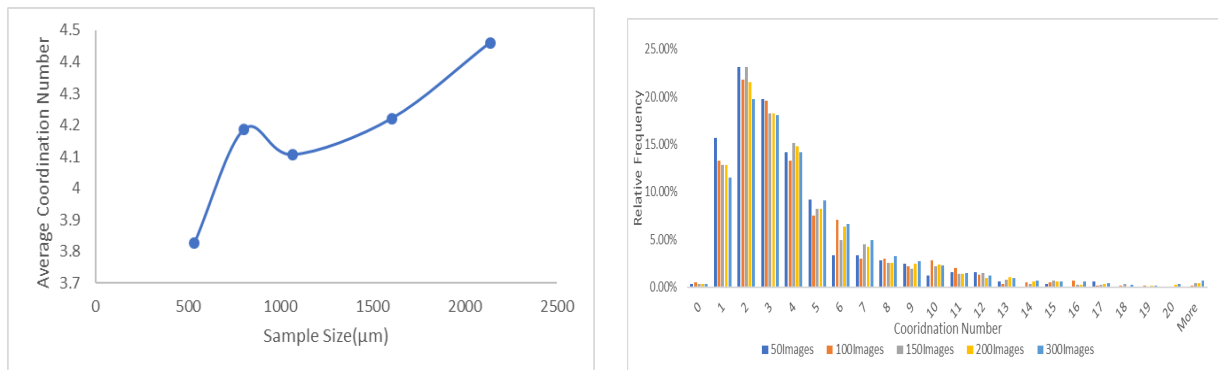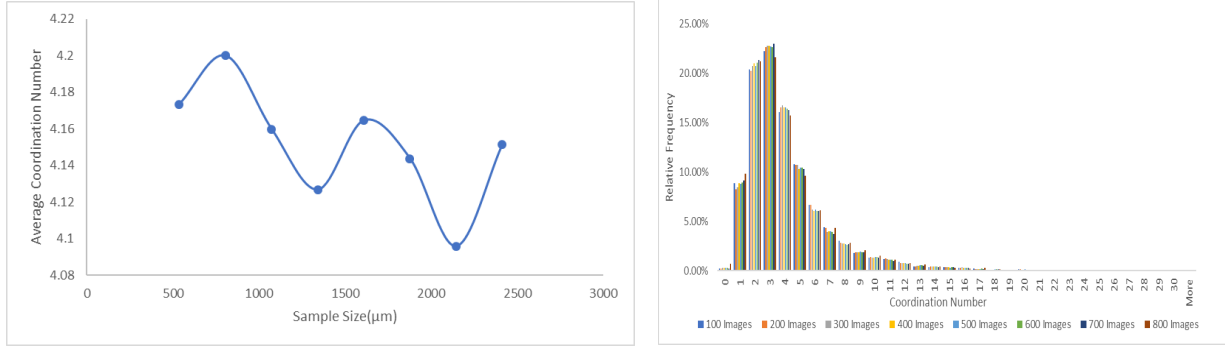
Figure 125 (a) Average Coordination with Sample Size(μm) (b) Histogram of Coordination Number for Estaillades Limestone Sample

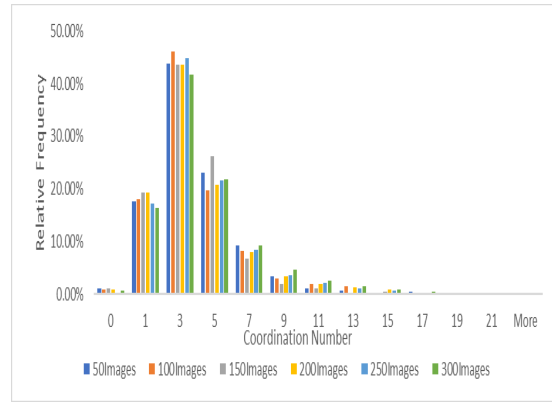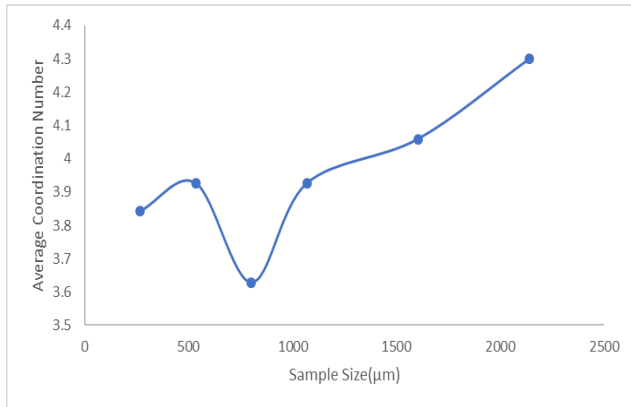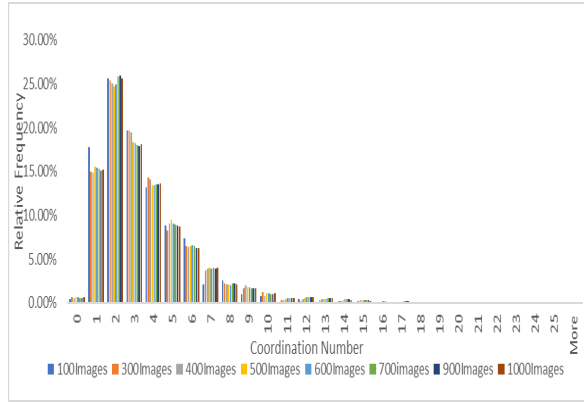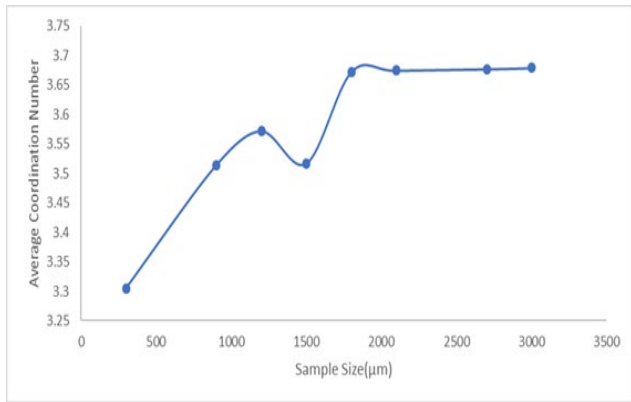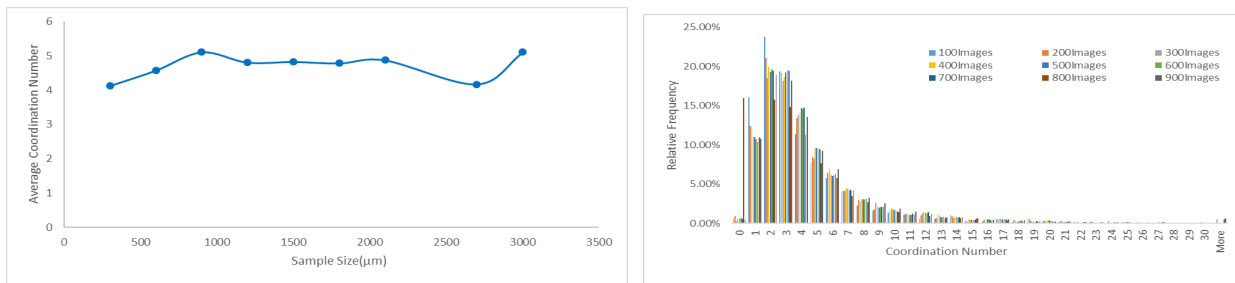**Figure 126 (a) Average Coordination with Sample Size(μm) (b) Histogram of Coordination Number for Ketton Limestone Sample**

5.2 Absolute Permeability

In this section, permeability simulation was done for 22 samples in three directions (x, y, z) and compared for each sample in order to study the existence of REV and permeability anisotropy. Because the pore network model could follow the percolation theory, the absolute permeability is directly calculated by Avizo® XLab module. The single-phase flow simulation is performed on all extracted connected pore networks to compute absolute permeability by solving Stokes equations and applying Darcy's law (Munawar et al., 2018). The single-phase fluid must be an incompressible Newtonian fluid with a steady-state laminar flow, and a viscosity of 0.001 Pa s is considered for simulation. Input pressure boundary conditions are set at 130 KPa and output at 100 KPa (Munawar et al., 2018). In the pore network model, the simulated single-phase fluid between two connected pores could be described as in Figure 128.
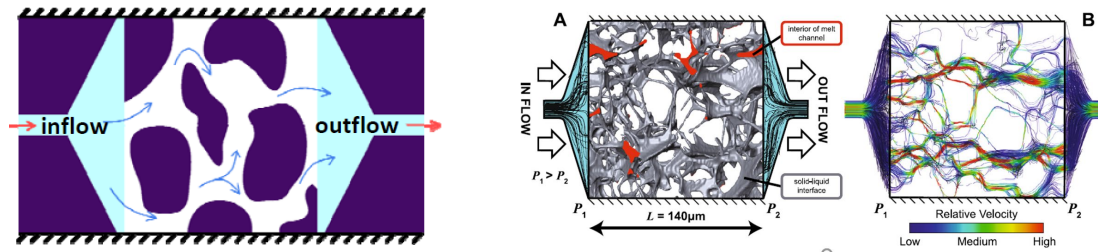
Figure 127 2D Illustration of the Permeability Simulation Setup (Zhang et al., 2011, Miller et al., 2013)

The measured absolute permeability results are compared in Table 3, taking into consideration the difference in network extraction approaches (mentioned in Chapter 3).

		S1	S2	S3	S4	S5	S6	S7	S8	S9	C1	C2	Berea
Kx	LBM	1.976	4.27	0.723	0.415	6.474	13.995	7.621	15.322	2.357	1.4	1.38	1.659
	AB	2.138	4.198	0.744	0.439	6.847	13.175	7.915	14.999	2.283	1.289	1.36	1.652
	WA	0.75	2.85	0.3	0.17	5.32	7.7	5.61	15.09	1.11	0.8	0.03	0.88
	MA	1.969	4.318	0.143	0.273	4.638	11.289	7.268	13.063	2.735	0.785	0.038	1.36
	HA	**1.807**	**4.672**	**0.39**	**0.216**	**5.208**	**13.61**	**7.426**	**18.276**	**2.421**	**0.376**	**0.22**	**1.386**
Ky	LBM	2.513	4.814	1.185	0.597	6.462	15.065	10.235	16.298	2.694	2.355	0.138	1.801
	AB	2.597	4.883	1.2	0.596	6.396	13.976	9.254	15.666	2.79	2.282	0.136	1.816
	WA	1.7	3.33	0.28	0.221	3.66	13.87	6.83	14.81	1.65	0.81	0.09	0.91
	MA	1.752	3.983	0.42	0.289	4.874	10.683	7.594	13.507	2.093	1.469	1.61	1.304
	HA	**1.501**	**4.309**	**0.637**	**0.23**	**6.814**	**16.107**	**8.72**	**16.12**	**2.1993**	**1.35**	**0.739**	**0.09**
Kz	LBM	2.74	5.252	0.784	0.573	6.223	18.246	9.349	15.61	3.319	1.185	0.161	1.872
	AB	2.816	5.174	0.733	0.587	6.202	14.66	9.271	14.897	3.506	1.138	0.139	1.901
	WA	0.9	2.96	0.47	0.23	2.92	8.63	6.69	15.35	1.44	1.62	0.18	0.91
	MA	1.312	3.394	0.109	0.215	4.44	10.951	6.037	12.936	1.844	1.053	0.018	1.193
	HA	**1.105**	**4.27**	**0.363**	**0.157**	**7.06**	**13.52**	**9.95**	**15.2**	**1.394**	**1.22**	**1.001**	**0.06**

Table 3 Absolute Permeability Computed from Different Pore Networks

This table comprehensively provides the results regarding absolute permeability along three axes by using five different approaches to measure 12 different samples. The results from the lattice Boltzmann method (LBM) and Axis-Ball (AB) algorithm are proposed by Yi et al. (2016), and the

source of absolute permeability results measured using a watershed algorithm (WA) is Rabbani et al. (2018). Additionally, Dong et al. (2009) provided absolute permeability results by using the maximum ball algorithm (MA). This dissertation mainly uses a hybrid algorithm (HA) of the Avizo® XLab module to measure absolute permeability. In contrast to these five methods, the results provided by the watershed algorithm are usually the smallest, and the results from the axis-ball algorithm are always highest. The results from the hybrid algorithm of Avizo® software lie in the middle of the results from the other four methods. Comparing the accuracy of these extracted network algorithms, the hybrid algorithm should be recognized as an excellent method to predict absolute permeability.

5.2.1 Absolute Permeability for Shale Samples

Figures 129 and Figure 130 show the absolute permeability of Eagle Ford and Marcellus shale samples with increasing sample size. What is striking in the statistics is that the curves firstly blow up, then dramatically fall off. The absolute permeability of Eagle Ford increases from 1.47E-08 to 3.34E-05 darcy at 2 μm, then it gradually declines to 2.01E-09 darcy. The factor of difference between the maximum permeability and the minimum permeability of Eagle Ford shale as the sample size increases is 1,000. The absolute permeability of the Marcellus shale sample is shown in Figure 130, with the curve of absolute permeability going up from 9.8E-09 to 2.89E-08 at 3μm, then going down to 1.2E-09. The maximum absolute permeability of this Marcellus shale sample is 10-fold higher than the minimum result. Furthermore, looking at Figure 131, the permeability range of 7 shale formations is divided. The absolute permeability of Eagle Ford is almost 100 times higher than Marcellus shale samples, which is consistent with the division of Figure 131. Also, these results indicate that permeability is reliably dependent on sample size; the absolute permeability firstly increases then decreases and forms a peak point at half of the total sample size.

However, the trend of the two curves is unanticipated, because since connectivity between pores gets limited as the sample size gets bigger, the pore connectivity and permeability could reasonably be expected to keep decreasing as the size of sample increases (Davudov & Moghanloo, 2016). One reason for this result might be the fact that the sample size is so small that it cannot represent the average properties of the entire sample. Furthermore, Tahmasebi et al. (2016) found that permeability exhibits significant fluctuations when the sample size is very small, and that the absolute permeability reaches a stationary state at a cubic volume of $300 - 400$ pixels. This also verifies that the permeability distribution could be helpful in determining the REV of samples. For the Eagle Ford and Marcellus shale samples, their REV should be around 4μm.
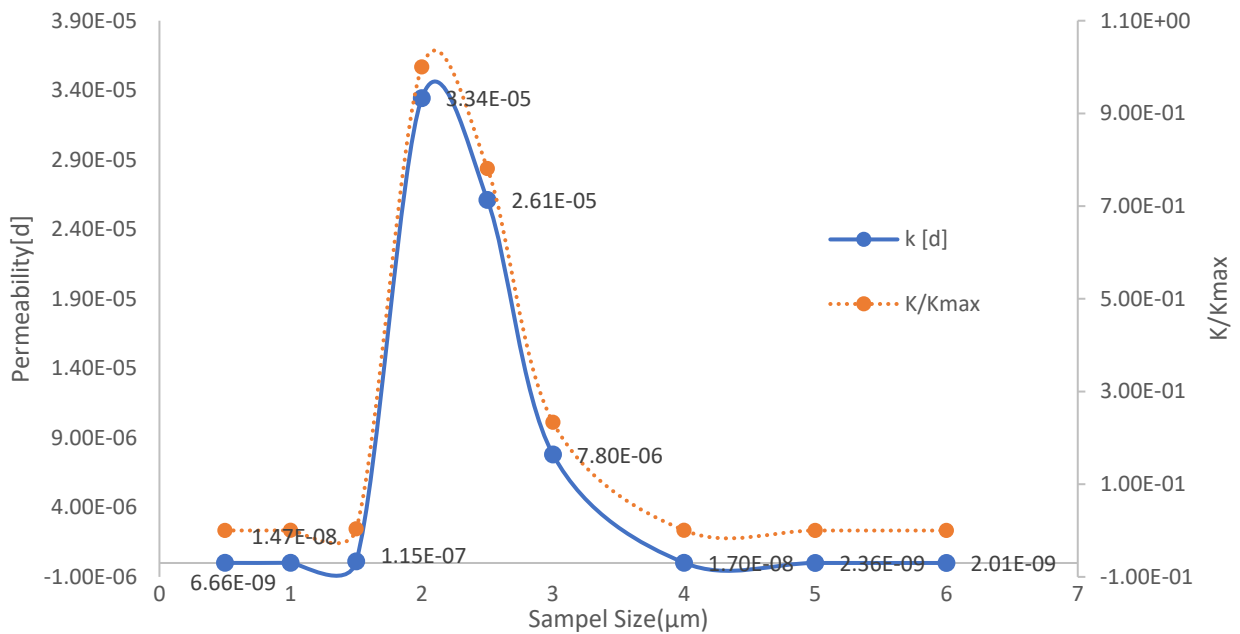
Figure 128 Permeability vs Sample Size for an Eagle Ford Shale Sample
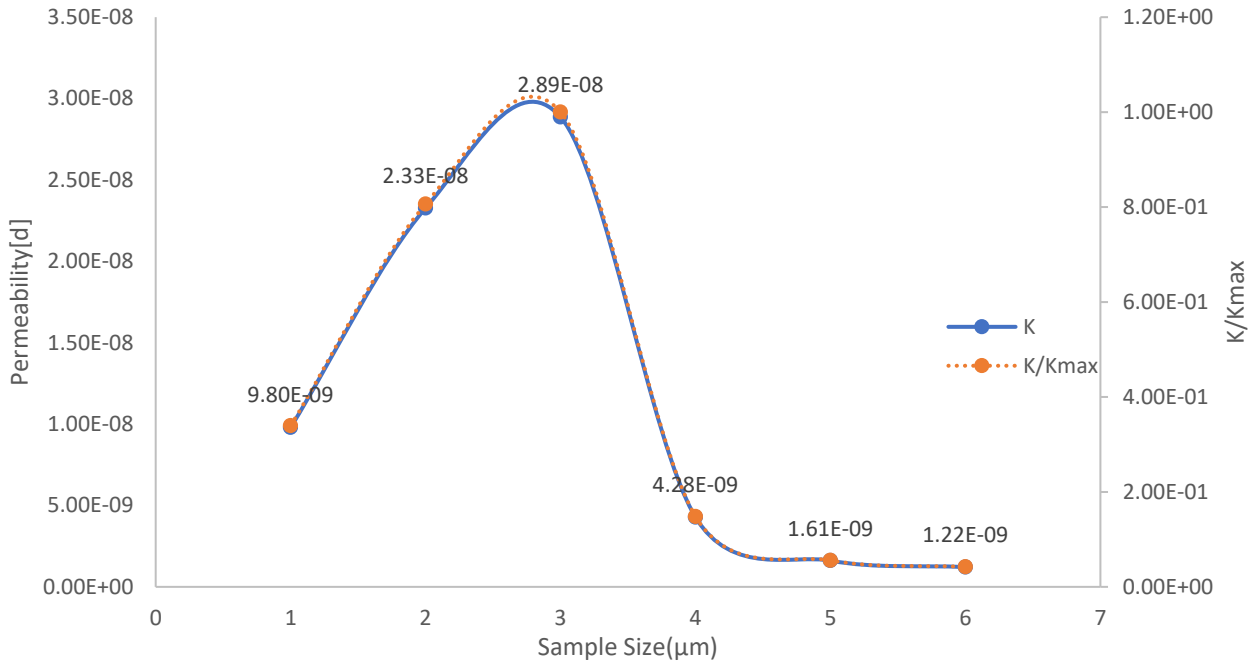
Figure 129 Permeability vs Sample Size for a Marcellus Shale Sample
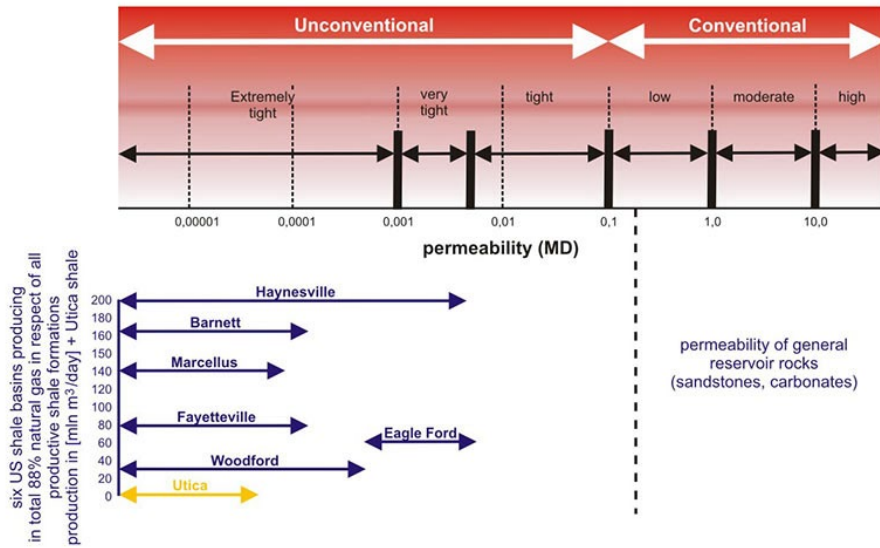
Figure 130 Permeability diagram of conventional and unconventional reservoirs (Faraj, 2012; Jarvie, 2012; Hughes, 2013)

5.2.2 Absolute Permeability for Sandstone Samples

Figure 132 − Figure 144 show the absolute permeability of 13 sandstone samples in three

directions (x-y-z). As can be seen, the permeability of three paths is anisotropic, and some curves

of permeability in the z-direction have a prominent tip, which is rising firstly and then falling off

88

like the above shale samples. This trend of the curve is likely caused by the number of images used for modeling being too small, falling to represent the whole sample. It thus corroborates the conclusion explained in the last section that absolute permeability would reach a stationary state at a cubic volume of 300 – 400 pixels. Furthermore, these figures reveal that anisotropy is influenced by a change in sample size. With the sample size increasing, the anisotropy of absolute permeability goes down to zero, while absolute permeability of sandstone in x and y directions still keeps the same upward tendency. More interestingly, according to the comparison of the thirteen sandstone samples, we find that for the sandstone sample with lower permeability (<1 darcy), the absolute permeability remains nearly unchanged. If the permeability of the sandstone sample is higher than 1 darcy, the distribution curve for absolute permeability would show an apparent drop. Furthermore, until the sample size is larger than 1mm or 1.5mm, the curve of permeability in three directions levels off. Hence, we deduce that the REV should be more than 1mm.

Figure 131 Permeability vs Sample Size for Sandstone Sample S1

Figure 132 Permeability vs Sample Size for Sandstone Sample S2
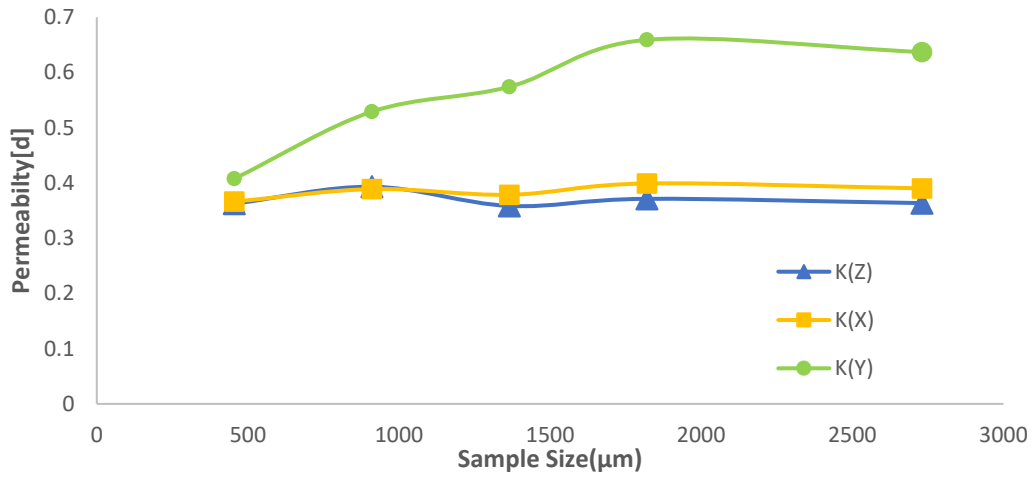
Figure 133 Permeability vs Sample Size for Sandstone Sample S3
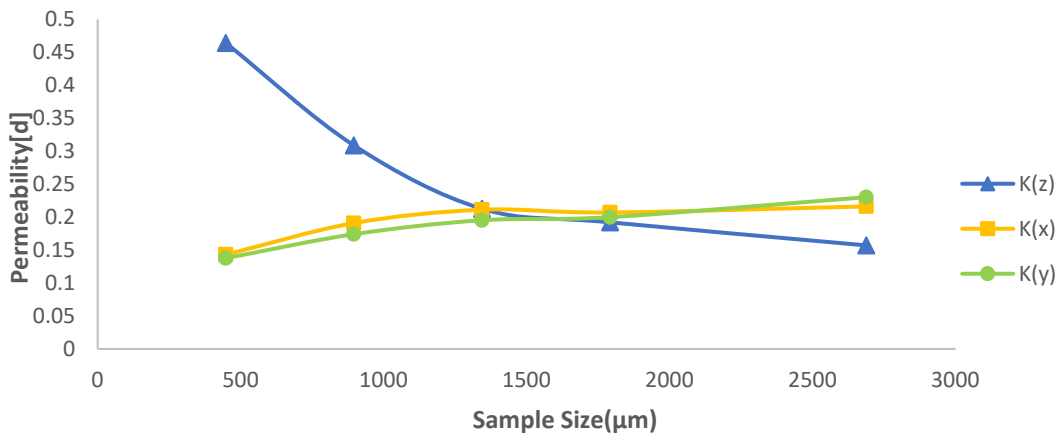
Figure 134 Permeability vs Sample Size for Sandstone Sample S4
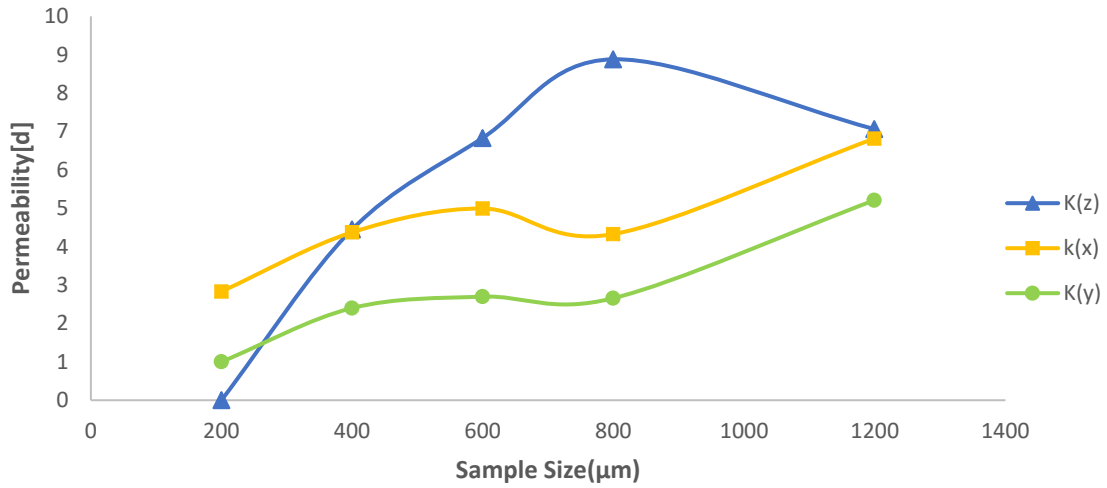
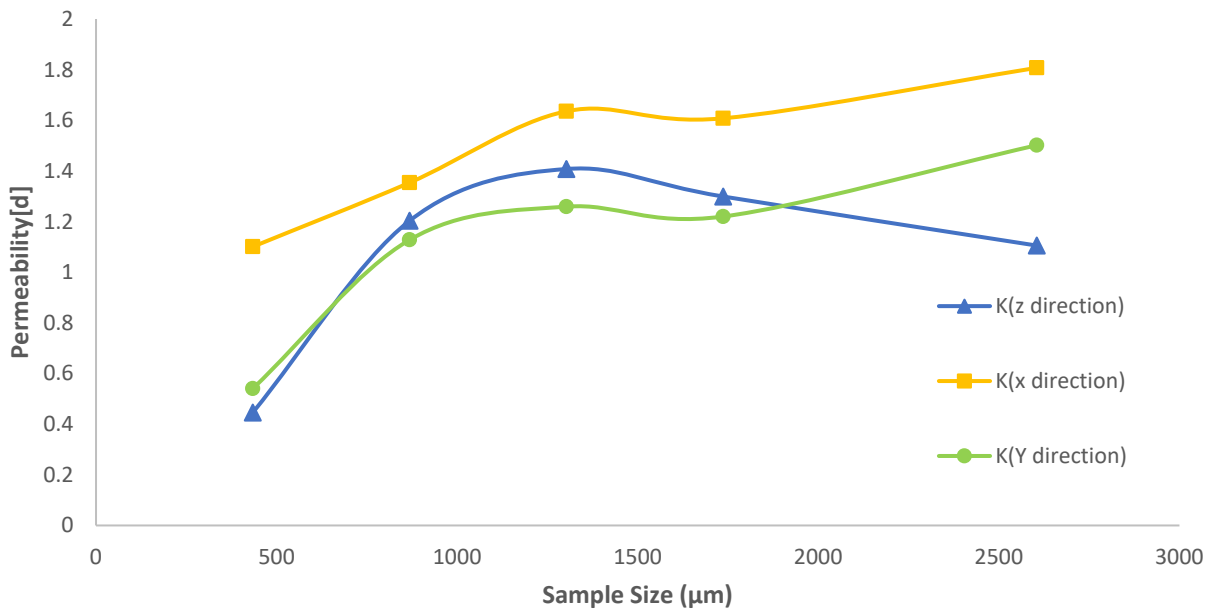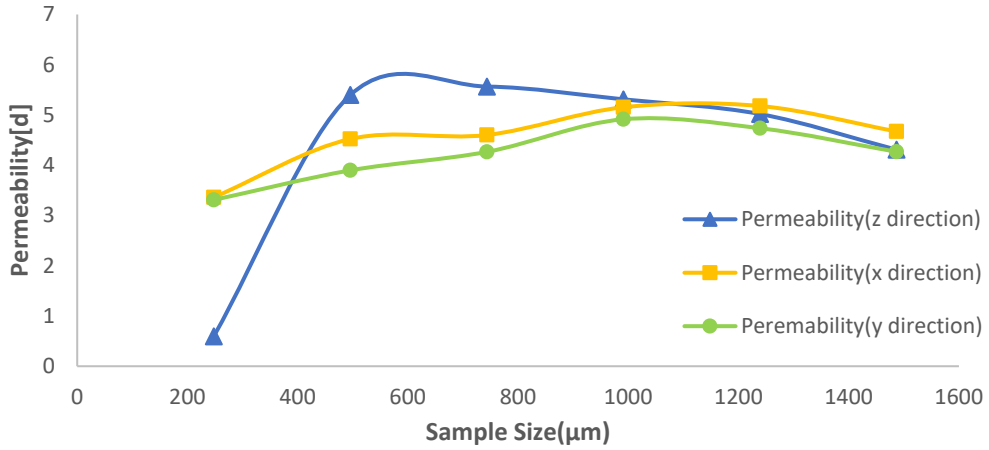**Figure 135 Permeability vs Sample Size for Sandstone Sample S5**
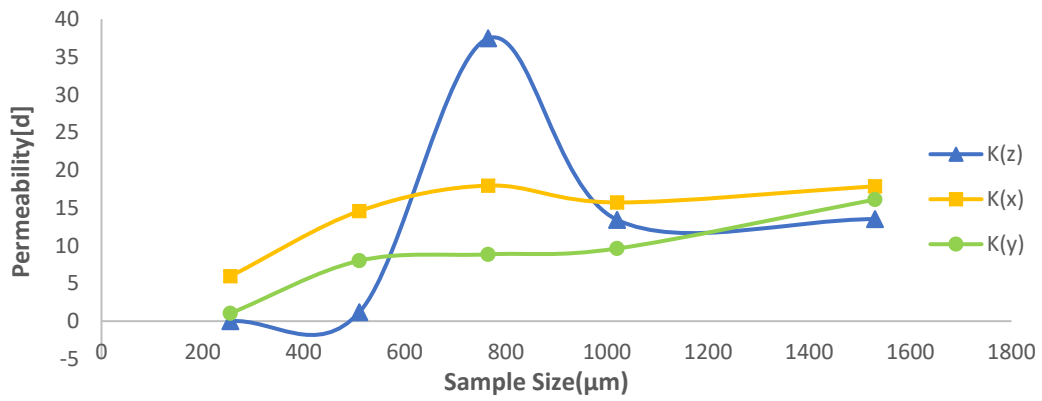
Figure 136 Permeability vs Sample Size for Sandstone Sample S6
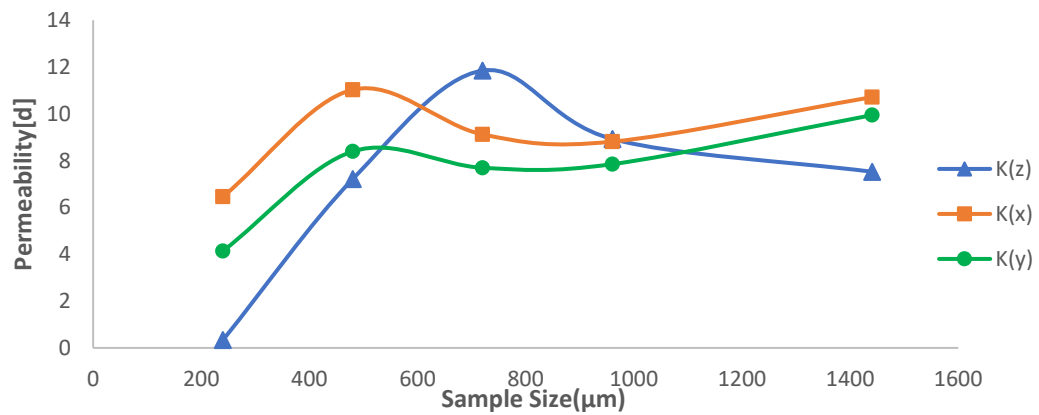
Figure 137 Permeability vs Sample Size for Sandstone Sample S7

Figure 138 Permeability vs Sample Size for Sandstone Sample S8
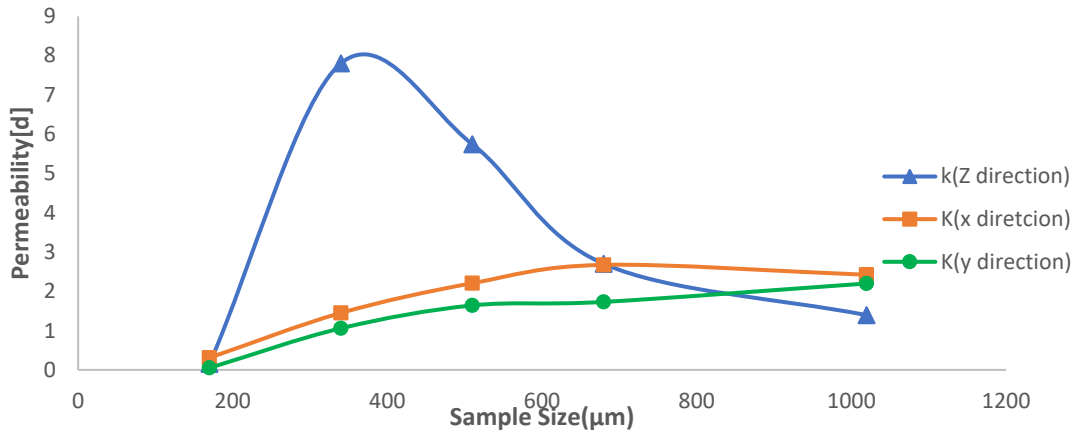
Figure 139 Permeability vs Sample Size for Sandstone Sample S9
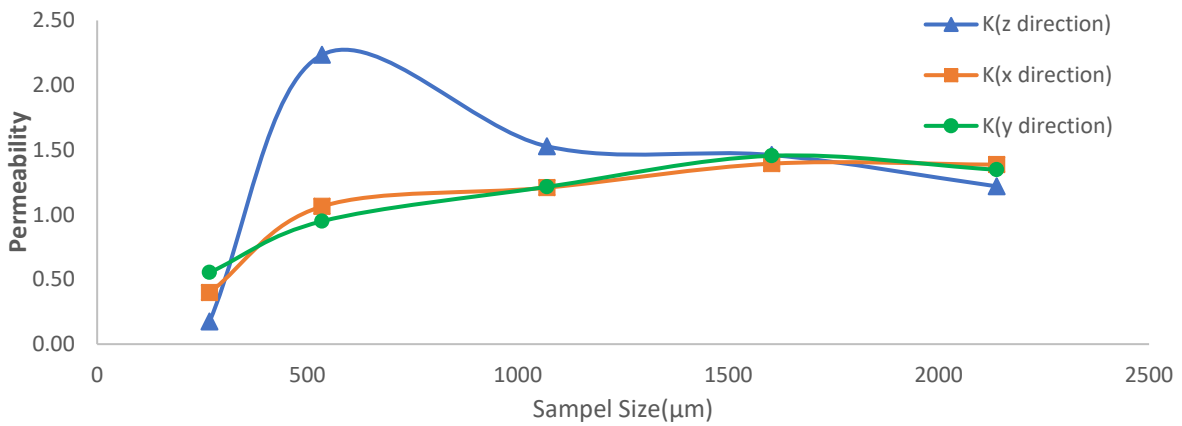
Figure 140 Permeability vs Sample Size for a Berea Sandstone Sample
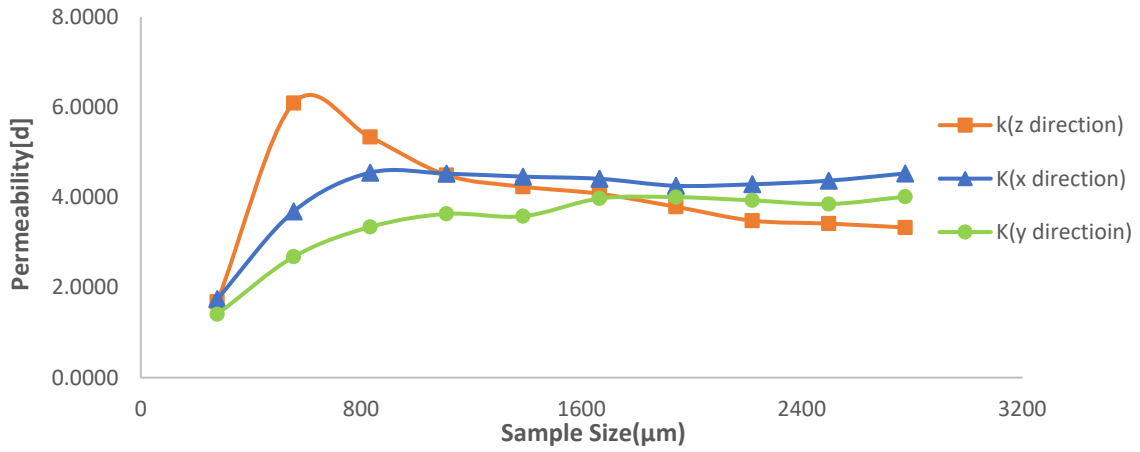
Figure 141 Permeability vs Sample Size for a Doddington Sandstone Sample
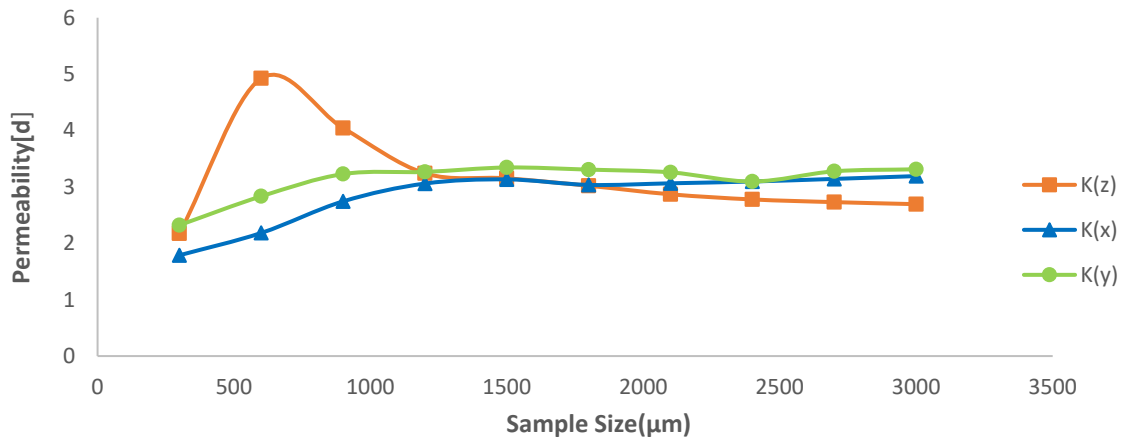
Figure 142 Permeability vs Sample Size for Sandstone Sample Bentheimer1
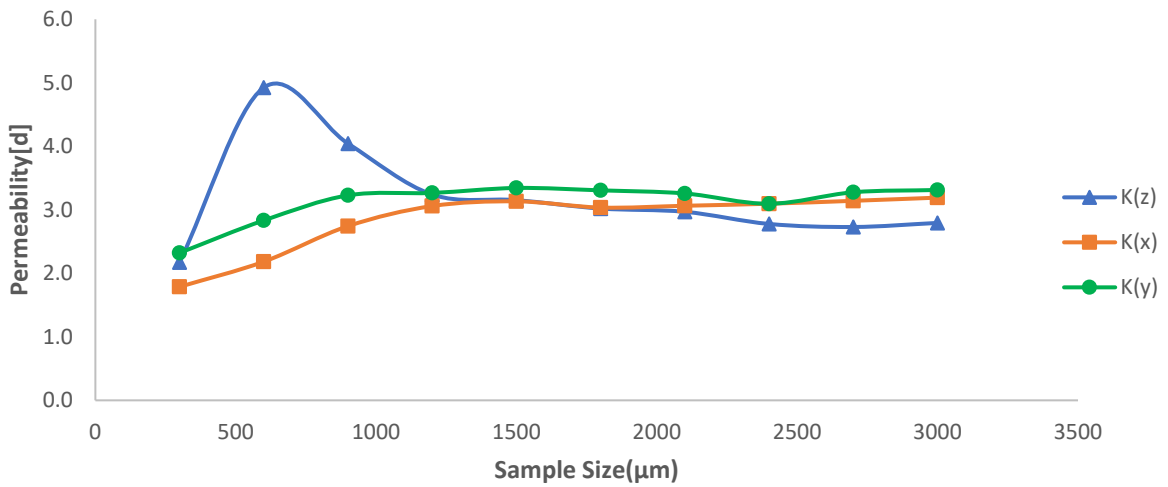
Figure 143 Permeability vs Sample Size for Sandstone Sample Bentheimer2

5.2.3 Absolute Permeability for Carbonate Samples

Figures 145 − 149 show the absolute permeability distribution of carbonate samples in three directions (x-y-z). Unlike the sandstone samples, the anisotropy of absolute permeability performs on all three pathways for the carbonate samples. The trend of three curves for each carbonate sample is divergent; moreover, the bend in the z-direction produces the peak value due to the permeability suddenly increasing and decreasing with increasing sample size. The range of absolute permeability for the carbonate samples is between 0.1 and 5 darcy. In general, as the sample size approaches 0.6mm, the absolute permeability starts to decline, and until 1mm, the absolute permeability gradually flattens out. Based on analysis regarding absolute permeability distribution for carbonate samples, the REV of carbonate samples should be around 1.3mm.

5.2.3 Absolute Permeability for Carbonate Samples
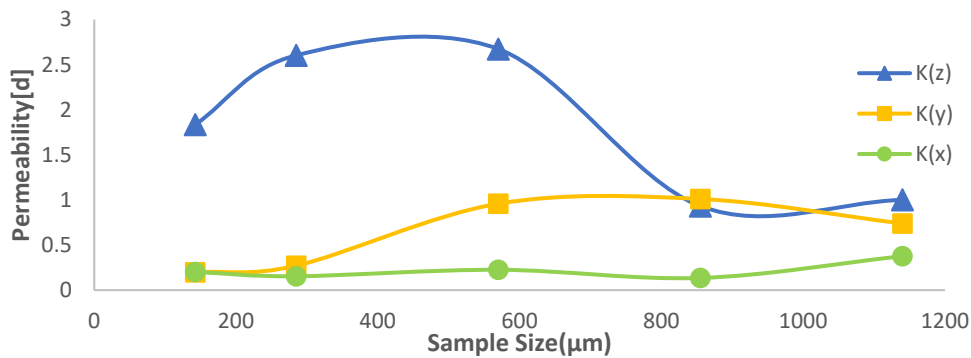
Figure 144 Permeability vs Sample Size for Carbonate Sample C1

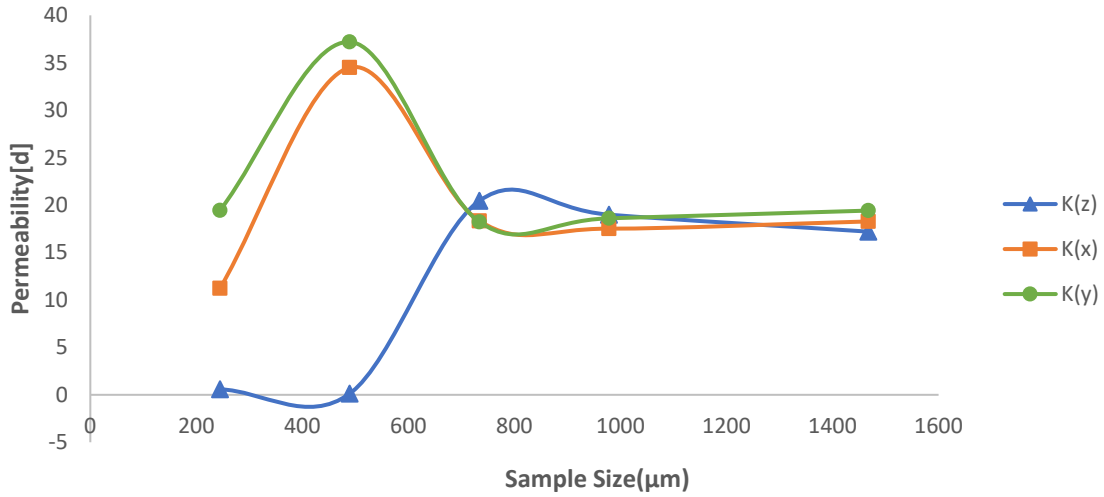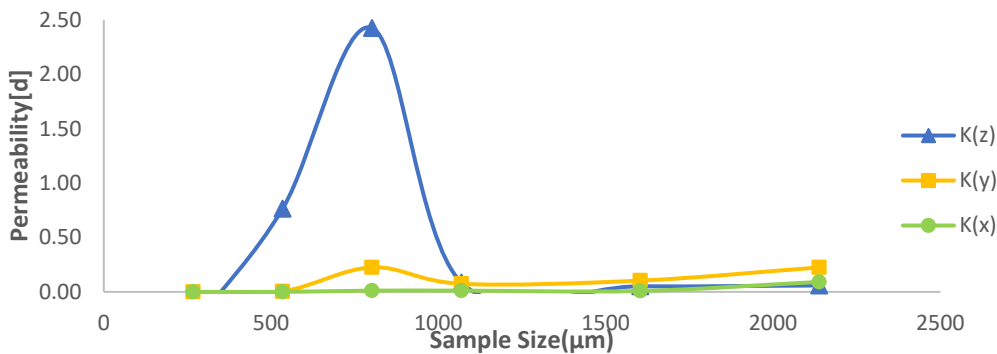**Figure 145 Permeability vs Sample Size for Carbonate Sample C2**
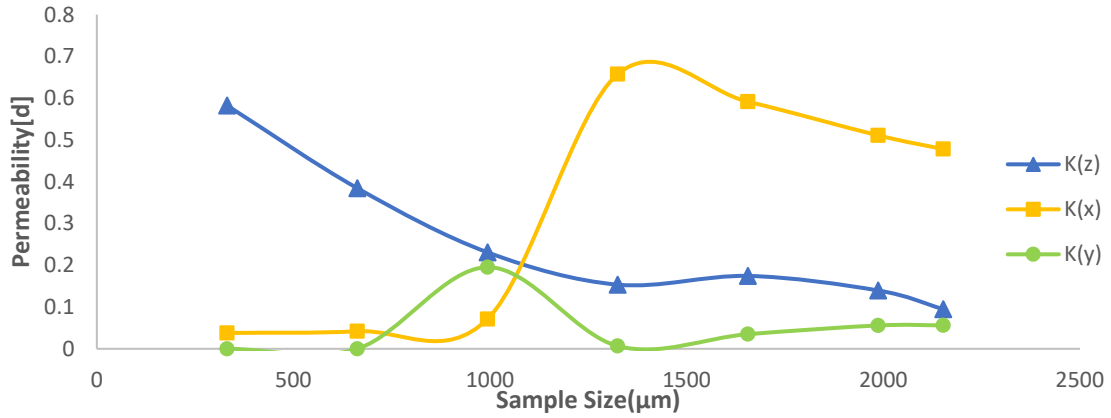
Figure 146 Permeability vs Sample Size for Carbonate Sample Estaillades 2
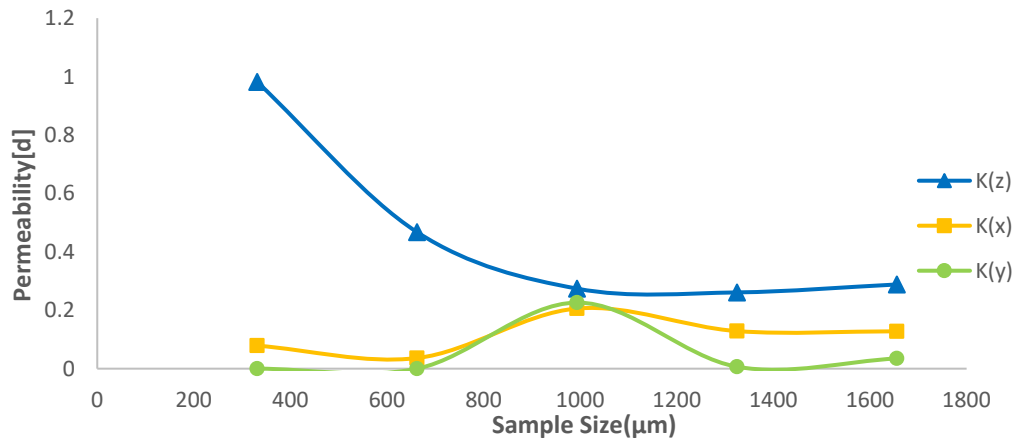
Figure 147 Permeability vs Sample Size for Carbonate Sample Estaillades 1
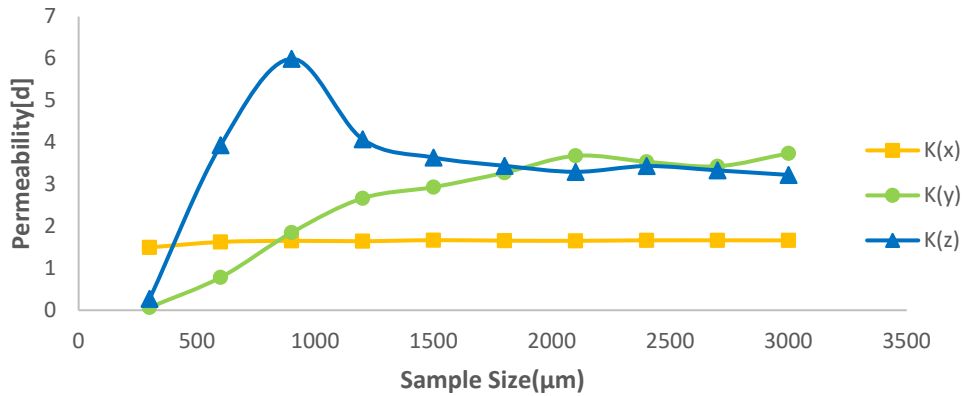
Figure 148 Permeability vs Sample Size for a Ketton Carbonate Sample

5.2.4 Absolute Permeability for Limestone Samples

Figure 150 and Figure 151 display the absolute permeability as a function of sample size along three directions for Ketton limestone and Estaillades limestone. Because there are so few samples of limestone, there are not many similarities to be seen. The permeability of Estaillades limestone in the z-direction starts decreasing at 0.2mm, dramatically dropping from 0.6 darcy to 0.01 darcy.

For Ketton limestone, the permeability firstly rises at 1mm sample size, then gradually declines from 13 darcy to 7 darcy. The only things in common between two limestone samples are that permeability of both samples has a similar trend in the x-and y-directions, and that the permeability of three directions are almost equal at the full sample size.

Figure 149 Permeability vs Sample Size for an Estaillades Limestone Sample

Figure 150 Permeability vs Sample Size for a Ketton Limestone Sample
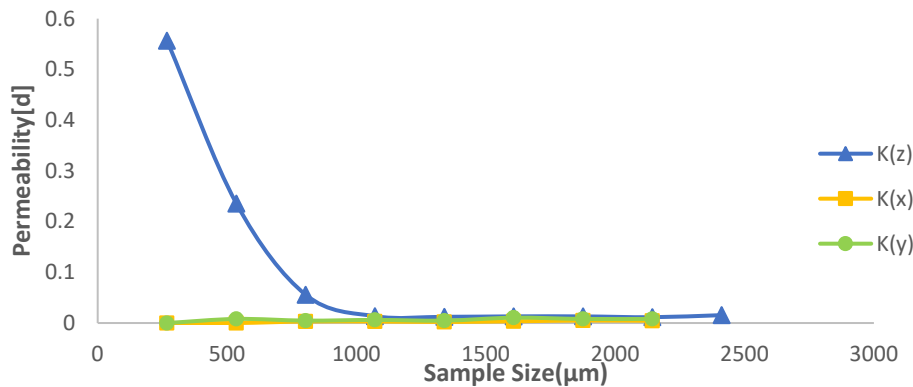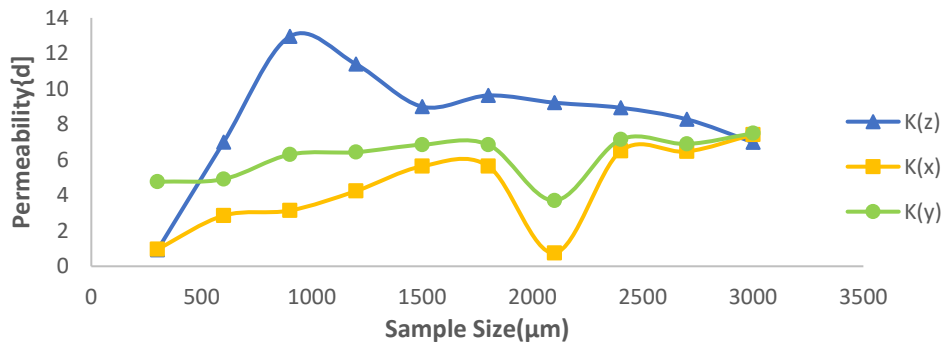
Sample Name	Mean Pore Radius (μm)	Mean Throat Radius	Average Coordination Number	Number of Total Pores	Number of Connected Pores	Number of Throats	Absolute permeability	Geometric Tortuosity	Porosity Connected(Total)
Eagle Ford	0.07	0.035	3.24	52736	3657	92906	2.01E-09	2.33	0.015(0.125)
Marcellus	0.03	0.011	4.86		4360		4.22E-11	1.818	0.0127(0.0017)
S1	46.88	24.68	3.43	1950	1429	2987	1.11	1.88	0.14
S2	31.37	16.37	4.83	2322	1884	4685	4.31	1.67	0.245
S3	32.69	15.33	3.49	9485	6574	12642	0.36	2.02	0.165
S4	31.34	15.06	2.99	10382	6537	11425	0.157	2.02	0.164
S5	25.6	20.7	3.81	865	511	1078	7.06	1.65	0.2108(0.211)
S6	33.4	23.8	5.02	1006	744	1775	16.1	1.72	0.238(0.239)
S7	36.1	19.65	5.07	1296	1076	2785	9.94	1.73	0.2501(0.2502)
S8	29.6	20.1	5.83	2407	1609	4847	15.19	1.65	0.338(0.339)
S9	28.8	16.6	3.65	706	541	1044	1.39	1.68	0.22(0.221)
Berea	34.5	15.4	4.18	5353	3966	8283	1.21	1.77	0.194(0.196)
Beth1	17.7	13.9	4.47	34790	20421	47425	2.69	1.805	0.2163(0.2167)
Beth2	17.7	14.3	4.47	34790	20422	47625	2.7	1.81	0.2163(0.2167)
Doddington	12	11	4.84	46726	22215	57356	3.33	1.85	0.215(0.216)
C1	11.19	9.9	4.46	8395	2130	9317	1.24	1.84	0.21(0.23)
C2	17 .4	13.6	4.3	13969	4249	11650	0.06	1.94	0.14(0.168)
Ketton 1	9.69	16.7	3.68	25781	5231	11446	1.794	1.8	0.131(0.132)
ES1	31.87	17.88	3.72	1836	1826	3431	0.28	1.75	0.108(0.108)
ES2	29.8	17.1	4	5828	4740	10338	0.095	1.82	0.118(0.129)
ES	17	9.6	4.15	49658	32542	68024	0.016	1.93	0.053(0.073)
Ketton 2	7.97	12.08	5.1	31097	10789	23908	6.9	1.79	0.148(0.149)

Table 4 Computed Pore Structure Parameters of 22 Rock Samples

Table 4 summarizes the computed pore structure parameters from the pore networks gathered from 22 rock samples. Based on the summarized parameters, we attempt to evaluate the relationship between these pore structure parameters and ascertain the main influencing factors of permeability. By observing the above table, it is evident which is the dominant factor influencing permeability.

For the heterogeneous shale samples, the pore radius, throat radius, and connected porosity should be the dominant factors causing low permeability. Because the Marcellus shale

permeability is ten orders of magnitude smaller than the permeability of Eagle Ford, the other parameters (geometric tortuosity and coordination number) of Marcellus are higher than that of Eagle Ford except for pore radius, throat radius, and connected porosity.

For the sandstone, carbonate and limestone samples, the parameters are plotted in Figure 152 to investigate which pore structure parameter is the predominant factor influencing permeability.
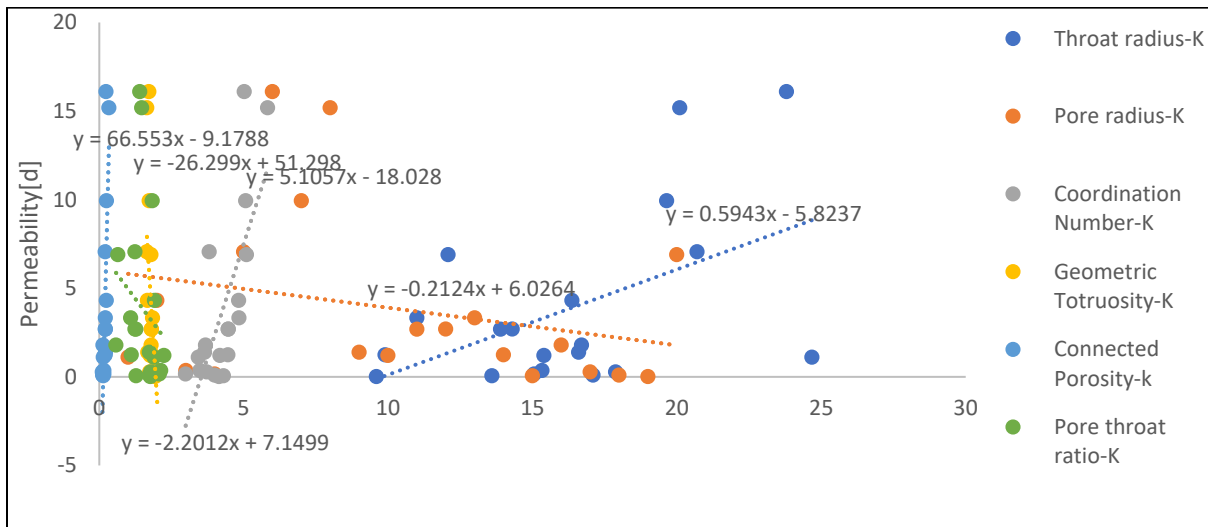
Figure 151 The Relationship Between Permeability and Pore Structure Parameters

By observing Figure 152, the correlation of permeability and computed pore structure parameters can be seen, and it is obvious that the slope of the relationship between permeability and connected porosity is highest, reaching 66. The second highest is geometric tortuosity, then coordination number. Thus, for the limestone, carbonate and sandstone, the main pore structure parameters that affect permeability should be (in order) connected porosity, geometric tortuosity and coordination number.

Chapter 6 Summary

In this thesis, an integrated study of pore structure characterization, pore connectivity, and permeability estimation using digital images is applied for four different lithological rocks, i.e., shale, sandstone, carbonate, and limestone. Furthermore, this study applied a methodology that combines the hybrid algorithm pore network and partitioning of the pore space, enabling a physical description of the geometry and topology of pore structure.

This study provides a new approach to evaluate and assess the differences in pore structure for 22 distinct rock samples. The main conclusions of the thesis are as follows:

- Our analysis indicated that connected porosity is 1.5% and 1.7% for two shale samples, much smaller than those of the sandstone samples ($14\% - 33.8\%$), carbonate samples ($13.2\% - 21.1\%$), and limestone samples ($3\% - 5\%$). The attributed pore radius distribution of shale samples ranges from $0.01\mu m$ to approximately $0.1\mu m$, while the effective pore radius of sandstone, carbonate, and limestone ranges from $1\mu m$ to $0.1mm$. The absolute permeability computed from the shale samples is around 2 nano-darcy, much smaller than those of the sandstone ($0.15 - 15$ darcy), carbonate ($0.1 - 5$ darcy) and limestone ($0.02 - 8$ darcy).

- For the two shale samples studied in this work, their connected porosity is ten times lower than their total porosity. The pore and throat size distribution of the analyzed shale sample range from $0.01\mu m$ to $0.1\mu m$. The geometric tortuosity is around 1.8 and 3.5, respectively. The coordination number of them is calculated between 3 and 5. As the sample size increases, only geometric tortuosity remains constant, and the other calculated parameters are influenced by the sample size.

- For the sandstone, carbonate, and limestone samples, the connected porosity is very close to total porosity, which ranges from 15% to 30%. The pore and throat size distribution of them is bounded between 10 and 100μm. The geometric tortuosity is around 2, and the coordination number is approximately between 4 and 6. The geometric tortuosity and absolute permeability of them are anisotropic and affected by sample size.

- Three REVs were calculated which is based on the variation of porosity, geometric tortuosity, and permeability as the sample size increases gradually. The size of REV measured by porosity is bigger than that obtained by permeability analysis and geometric tortuosity, which indicates that the study of a single parameter feature is difficult to ensure the reliability of REV measurement results, while the combination of the three parameters can provide a guidance for accurate prediction of REV.

- For the shale sample, the primary pore structure parameters influencing permeability are pore throat size and the connected porosity. In contrast, in sandstone, carbonate, and limestone samples, the main factors are connected porosity, geometric tortuosity, and the coordination number.

References

Al-Gharbi, M. S., & Blunt, M. J. (2004). 2D dynamic pore-scale network model of imbibition. In Developments in Water Science (Vol. 55, pp. 71-82). Elsevier.

Amien, M. N., Pantouw, G. T., Juliust, H., & Latief, F. D. E. (2019, August). Geometric tortuosity analysis of porous medium using simple neurite tracer. In IOP Conference Series: Earth and Environmental Science (Vol. 311, No. 1, p. 012041). IOP Publishing.

Avizo®. (2009). Avizo User's Guide.

Backeberg, N. R., Iacoviello, F., Rittner, M., Mitchell, T. M., Jones, A. P., Day, R., ... & Striolo, A. (2017). Quantifying the anisotropy and tortuosity of permeable pathways in clay-rich mudstones using models based on X-ray tomography. Scientific reports, 7(1), 14838.

Blunt, M. J., Bijeljic, B., Dong, H., Gharbi, O., Iglauer, S., Mostaghimi, P., ... & Pentland, C. (2013). Pore-scale imaging and modelling. Advances in Water Resources, 51, 197-216.

Bustin, R. M., Bustin, A. M., Cui, A., Ross, D., & Pathi, V. M. (2008, January). Impact of shale properties on pore structure and storage characteristics. In SPE shale gas production conference. Society of Petroleum Engineers.

Carman, P. C. (1937). L'écoulement d'un fluide à travers un lit de particules. Trans Inst. Chem. Engrs (Lond.), 15, 150.

Chawla, N., & Chawla, K. K. (2006). Microstructure-based modeling of the deformation behavior of particle reinforced metal matrix composites. Journal of Materials Science, 41(3), 913-925.

Davudov, D., Moghanloo, R. G., & Flom, J. (2018). Scaling analysis and its implication for asphaltene deposition in a Wellbore. SPE Journal, 23(02), 274-285.

Dunsmuir, J. H., Ferguson, S. R., D'Amico, K. L., & Stokes, J. P. (1991, January). X-ray microtomography: a new tool for the characterization of porous media. In SPE annual technical conference and exhibition. Society of Petroleum Engineers.

Dong, H., & Blunt, M. J. (2009). Pore-network extraction from micro-computerized-tomography images. Physical review E, 80(3), 036307.

Goral, J., Deo, M., & Andrew, M. (2018). Pore network modeling of Marcellus Shale using digital rock analysis with machine learning image segmentation. ZEISS Application Note.

Gostick, J. T. (2017). Versatile and efficient pore network extraction method using marker-based watershed segmentation. Physical Review E, 96(2), 023307.

Hemes, S., Desbois, G., Urai, J. L., Schröppel, B., & Schwarz, J. O. (2015). Multi-scale characterization of porosity in Boom Clay (HADES-level, Mol, Belgium) using a combination of X-ray μ-CT, 2D BIB-SEM and FIB-SEM tomography. Microporous and mesoporous materials, 208, 1-20.

Landini, G., Randell, D. A., Fouad, S., & Galton, A. (2017). Automatic thresholding from the gradients of region boundaries. Journal of microscopy, 265(2), 185-195.

Lee, P. H., & Kozak, J. J. (1987). Calculation of the tortuosity factor in single-phase transport through a structured medium. The Journal of chemical physics, 86(8), 4617-4627.

Lindquist, E. E. (1996). .1 External anatomy and systematics 1.1. 1. External anatomy and notation of structures. In World crop pests (Vol. 6, pp. 3-31). Elsevier.

Lymberopoulos, D. P., & Payatakes, A. C. (1992). Derivation of topological, geometrical, and correlational properties of porous media from pore-chart analysis of serial section data. Journal of colloid and interface science, 150(1), 61-80.

Lyra, M., & Ploussi, A. (2011). Filtering in SPECT image reconstruction. Journal of Biomedical Imaging, 2011, 10.

Nguyen, T. T., Bui, H. H., Ngo, T. D., & Nguyen, G. D. (2017). Experimental and numerical investigation of influence of air-voids on the compressive behaviour of foamed concrete. Materials & Design, 130, 103-119.

Peng, S., Yang, J., Xiao, X., Loucks, B., Ruppel, S. C., & Zhang, T. (2015). An integrated method for upscaling pore-network characterization and permeability estimation: example from the Mississippian Barnett Shale. Transport in Porous Media, 109(2), 359-376.

Okabe, H., & Blunt, M. J. (2004). Prediction of permeability for porous media reconstructed using multiple-point statistics. Physical Review E, 70(6), 066135.

Raeini, A. Q., Bijeljic, B., & Blunt, M. J. (2017). Generalized network modeling: Network extraction as a coarse-scale discretization of the void space of porous media. Physical Review E, 96(1), 013312.

Rabbani, A., Mostaghimi, P., & Armstrong, R. T. (2019). Pore network extraction using geometrical domain decomposition. Advances in water resources, 123, 70-83.

Remy, M. (2002). Wikipedia: The free encyclopedia. Online Information Review.

Schmitt, M., Halisch, M., Müller, C., & Fernandes, C. P. (2016). Classification and quantification of pore shapes in sandstone reservoir rocks with 3-D X-ray micro-computed tomography. Solid Earth, 7(1), 285-300.

Silin, D., & Patzek, T. (2006). Pore space morphology analysis using maximal inscribed spheres. Physica A: Statistical mechanics and its applications, 371(2), 336-360.

Thompson, K. G., Biscoe, K. L., & Sato, T. R. (2005). Neuronal basis of covert spatial attention in the frontal eye field. Journal of Neuroscience, 25(41), 9479-9487.

Yi, Z., Lin, M., Jiang, W., Zhang, Z., Li, H., & Gao, J. (2017). Pore network extraction from pore space images of various porous media systems. Water Resources Research, 53(4), 3424-3445. Youssef, S., Han, M., Bauer, D., Rosenberg, E., Bekri, S., Fleury, M., & Vizika, O. (2008).

High resolution μCT combined to numerical models to assess electrical properties of bimodal carbonates. Abu Dhabi, UAE, 29.

Zhang, S., Klimentidis, R. E., & Barthelemy, P. (2011, September). Porosity and permeability analysis on nanoscale FIB-SEM 3D imaging of shale rock. In International Symposium of the Society of Core Analysts (pp. 18-21).

Zhang, Y., Ghanbarnezhad Moghanloo, R., & Davudov, D. (2019, April). Pore Structure Characterization of a Shale Sample Using SEM Images. In SPE Western Regional Meeting. Society of Petroleum Engineers.

Zworykin, V. K. (1942). The scanning electron microscope. Scientific American, 167(3), 111-113.

Appendix

2-D Cross Section of Image Samples used in the study:

(1) SEM Images
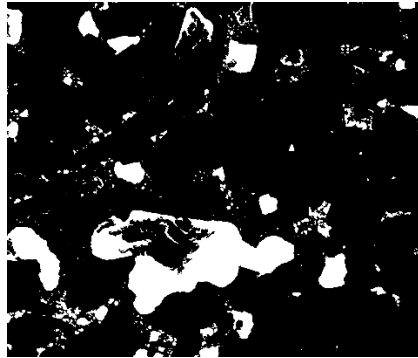
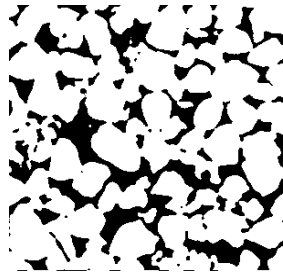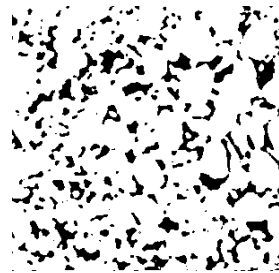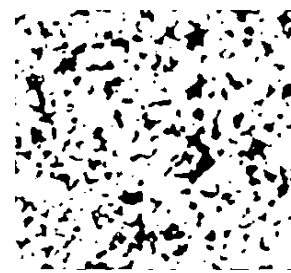Eagle Ford shale   Marcellus Shale

(2) Micro-CT Images

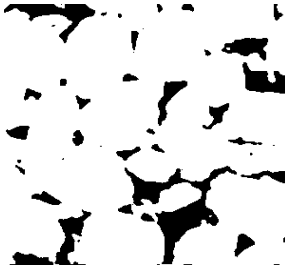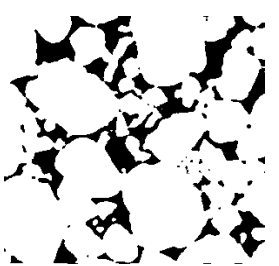SandstoneS1   Sandstone S2   Sandstone S3   SandstoneS4
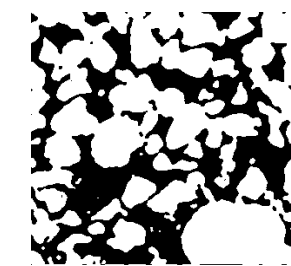

Sandstone S5   Sandstone S6   Sandstone S7   Sandstone S8
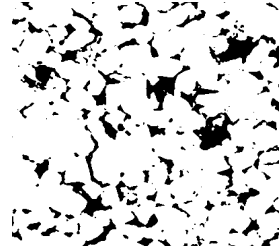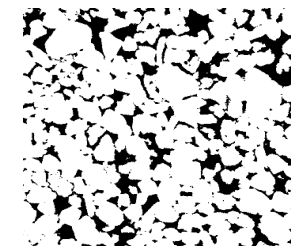

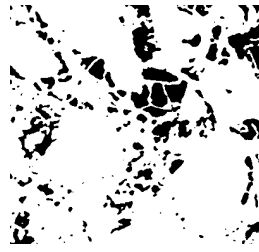Sandstone S9   Doddington Sandstone   Berea Sandstone   Betheimer Sandstone1

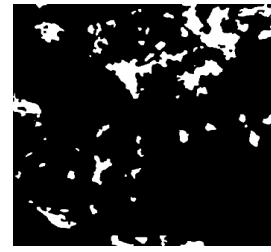BetheimerSandstone2   Carbonate C1   Carbonate C2   Estaillades Carbonate
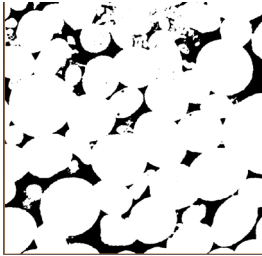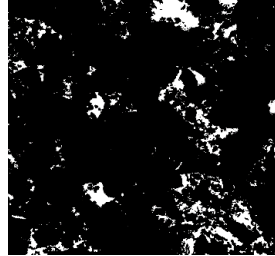
Ketton Carbonate   Estaillades Carbonate2   Estaillades Limestone   Ketton Carbonate